**Università degli studi di Salerno**

**FACOLTA' DI SCIENZE MATEMATICHE, FISICHE E NATURALI**

Corso di dottorato in scienze e tecnologie dell'informazione, dei sistemi complessi e dell'ambiente

XII ciclo


**PHD THESIS**

# The last forty years of surface deformation at Campi Flegrei caldera: two simple stationary sources are enough

Candidate: **Ilaria Sabbetta**

Tutor
**Prof. Luca Crescentini**

PhD Coordinator
**Prof. Roberto Scarpa**

Academic Year 2012/2013

# Contents

# Introduction

The Campi Flegrei (CF) caldera is one of the world's most active caldera; in this area the volcanic risk is extremely high, because of its location in a densely populated area about 15 km west of Naples inside the Campanian Plain. This caldera is renowned for its long historical activity that includes earthquakes, eruption and intense unrest episodes. The source of the observed surface deformation at Campi Flegrei has been and is a matter of debate, particularly in the last two years (2011-2013) because of a considerable uplift ($\sim 15\,cm$) that have drawn attention from both the scientists and civil protection.
In such a context, my thesis has been focused to find a simple model source that explains the CF deformation field during the last forty years (1970-2013), analyzing different types of data. The positive bradyseism crisis of 1982-1984 and the negative bradyseism of 1995-2000, in particular, are investigated. Different periods are covered by different types of data, from 1970 to 1994 by leveling data, in 1980 and in 1983 by geodetic precise traversing data, from 1993 to 2010 by Synthetic-Aperture Radar (SAR) data and finally from 2000 to October 2013 by continuous Global Positioning System (cGPS).
The first part of the thesis (chapters 1, 2 and 3) consists of a description of the deformation history of CF and the state of the art. Different models for earthquake volcano deformation, used to explain the CF phenomenology and two kinds of Monte Carlo inversion methods to determine the model source, are introduced.
In the second part (chapters 4, 5 and 6), the results of the analysis and of the inversion are described. Firstly the period 1970-2010 is analyzed, using leveling, geodetic precise traversing and SAR data, and subsequently cGPS data for the 2000-2013 period are used to confirm the found model .
We will see that, for the entire investigated period (1970-2013), a single stationary source, at about 4000 m in depth, satisfies overall CF deformation during the whole investigated

period and the residuals (with respect to the above source) deformation is confined to the Solfatara fumarolic field and satisfied by a stationary shallower small source located beneath Solfatara, at about 2000 m in depth; after 2005, also east side of CF seems to uplift abnormally.

In this sense, ground displacement data are analyzed in order to discern similarities or differences between CF inflation and deflation periods and to highlight possible anomalies in particular areas of the CF caldera. The first step was analyzed ground deformation pattern between the major 1982-84 inflation and subsequent deflation, focusing on periods with large signals and constant ratio. To compare the vertical displacements of this periods, each dataset was rescaled to match the 1980-83 one in the area of maximum uplift; the agreement is nearly perfect, apart from benchmarks in the Solfatara area and immediately South of it, where a local deformation source, with a different time history, seems superposed on the large-scale one. Same results are obtained by the comparison of eastward displacements of SAR data (period 1995-2000) and geodetic precise traversing data (period 1980-1983). This suggest the stationarity of the deformation field for these periods, apart for the Solfatara area.

The data of the 1980-1983 uplift are inverted for different models; this period is particularly favorable because of the presence of vertical and horizontal displacements data and because the Solfatara area is not cover by a leveling route in this period, so the inversions are not affected by a possible anomaly in the area.

Since the importance of taking into account the stratification is evidenced by many authors *(Amoruso, Crescentini and Fidani, 2004, Amoruso and Crescentini, 2007,* etc), a layered media is used for the inversion, and a quasi-horizontal elongated crack (oriented NW to SE, at a depth of about 3600 m) satisfies large-scale deformation. All source parameters but potency (volume change) are constant over time. Subtracting the effect of this source from the SAR data for 1995-2000 period, residuals are located in the Solfatara area. The anomaly is much more localized than large-scale deformation and suggests the presence of a local quasi-axis-symmetric shallower source.

From a mathematic point of view the best-fit source is a small (point) pressurized spheroid having vertical symmetry axis at a depth of 2000 m; location, aspect ratio, and volume change were left free in the inversion. The thesis is that this two-source model (a quasi-horizontal elongated crack + pressurized spheroid), can explain all the inflation and deflation phenomena at CF. Indeed, the deformation pattern is stationary during the period of

availability of SAR data, and to prove this, a correlation plot between the vertical displacement, at different points of CF which are representative of the behavior of the region, and the actual vertical displacement in the reference area, is produced. Points out of Solfatara are always very close to the best-fit 1993-1997 regression lines (indicating linear time-invariant correlation), while points related to Solfatara depart largely and non-randomly from the best-fit 1993-1997 regression line. This correlation plot suggests the stationarity of the deformation pattern, except for the Solfatara area, during the availability period of SAR data. This seems to confirm the thesis of two-source model during the whole investigated period (1970 to 2010).

The time histories of the two volume changes are estimated by a multiple linear regression, using the time histories of leveling uplift, and SAR vertical and eastward displacements data. The two sources volume changes histories are somewhat similar but not equal, supporting the existence of a genuine local deformation source at Solfatara against the emergence of a mere distortion of large-scale deformation.

Subsequently the analyzed period is extended, until October 2013, using cGPS data, inverting leveling and precising traversing data as previously described, but joining displacements cGPS data, for the period 2011-2013 (uplift period), scaled on 1980-83 displacement. The two-source model is confirmed, indeed residuals, with respect to the two-source model, are always almost null. Although reality is probably much more complex, this simple model explains 1970–2013 CF deformation within ground-displacement data errors and is consistent with Solfatara geochemical conceptual models, fumarolic geochemical data, and seismic attenuation imaging of CF. The observation that the CF deformation pattern can be decomposed into two stationary parts is hardly compatible with several recent works which proposed multiple sources with different features acting in different periods, fluid injections implying ample changes of large-scale deformation pattern over time, complex spatio-temporal patterns of distributions of volumetric sources.

# Chapter 1

# Ground deformation at Campi Flegrei area (Italy)

## 1.1 Deformation history

The Campi Flegrei (CF) caldera, located in the suburban area of Naples, in southern Italy, has been one of the world's most active caldera, characterized by intense unrest episodes involving huge ground deformation and seismicity. The large number of inhabitants make it one of the most hazardous area in the world.
Ground movements at CF caldera had been recognized since Roman times; the secular changes in the height above the sea level of "Serapeo", a Roman market at the Pozzuoli bay, have been documented from time to time *(Parascandola,1947)*. The time evolution of slow ground movements (called "bradisisma" from the Greek term for "slow seism") has been reconstructed from traces of marine deposits on this ancient monument. The CF are an agglomerate of many volcanic structures located in a circular area with a radius of about $12\,km$; this structure is a result of two major collapses related to the Campanian Ignimbrite (CI; 37.000 years BP) and the younger Neapolitan Yellow Tuff (NYT; 12.000 years BP) caldera. The CI, the largest pyroclastic deposit of the Campanian area, covered an area of about $30.000\,km^2$ with about $150\,km^3$ of erupted magma ranging in composition from trachyte to phonolitic-trachyte. The NYT eruption, the second largest of the Campanian area, had a very complex history; its eruptive dynamics changed during the course of the eruption according to variations of the efficiency of water/magma interaction and to

caldera collapse *(Orsi et al., 1996)*. The NYT covered an area of about $1000\,km^2$, including the Pozzuoli and Naples bays, while the volume of erupted magma was about $40\,km^3$. After each caldera collapse, volcanism was restricted within the collapsed area. During the past 10.000 years, most eruptive activitis have occurred during two periods: from 10.000 to 8000 years ago and from 4500 to 3700 years ago *(Dvorak and Berrino,1991)*. Two eruptions within the past 4000 years formed trachytic domes, Accademia and Monte Albano, near the center of Campi Flegrei.

The results of all this events are shown in figure 1.1 with a structural map of the CF caldera with the margins of CI and NYT caldera and the faults. Some fast and intense episodes of ground uplift occurred, culminating in eruption in the case of 1538 episode; this eruption, from 29 September to 6 October 1538, produced a new volcano, Monte Nuovo, that took place after 3.5 Ka of quiescence in the NW sector of the caldera. The first sign of unrest of the caldera became evident starting from AD 1503, when the uplift of the caldera center gradually led to the drying up of new land near the town of Pozzuoli *(Parascandola 1946, D'Oriano et al., 2005)*.

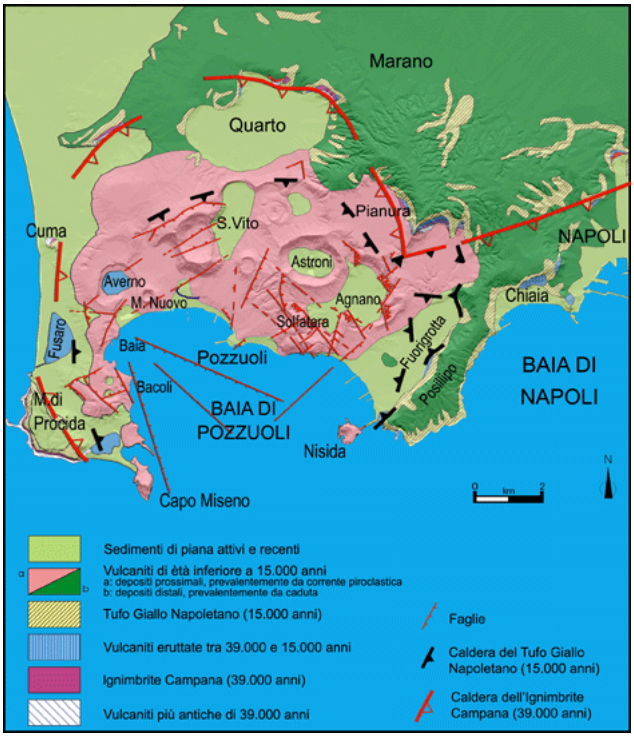


Figure 1.1: Structural map of the Campi Flegrei caldera (from http://www.ov.ingv.it/ov/)


Figure 1.2: Chronography of the volcanic history of the Campi Flegrei caldera (from http://www.ov.ingv.it/ov/)

The caldera has been generally subsiding (at about 1.5 cm per year) from 1538 till 1969; in 1970 started the most recent unrest episode with a fast uplift of 1.5 m. After 1972 the surface subsided relatively slowly by about 20 cm until 1974, in this period the vertical displacement field is essentially radial with a radius of about 7$km$.
The most important recent uplift started in January of 1982 and had its maximum, 1.80$m$, in November 1984, then subsided again at an average rate of 5 cm/yr without an eruption. A long-standing controversy characterizes the interpretation of the 1982-1984 unrest, both in the source geometry and unrest cause (intrusion of magma and/or magmatic fluids or instability of the hydrothermal system). Several point-or-finite source models (usually axisymmetric) have been invoked, from the tensile fault (*Dvorak and Berrino,1991*), to spheres, prolate spheroids and horizontal circular cracks *(e. g. Gottsmann et al., 2006a; Battaglia et al., 2006; Amoruso et al., 2008; Woo and Kilburn, 2010*), to a generic mo-

ment tensor *(Trasatti et al., 2011)*. *Beauducel et al. (2004)* investigated the role of caldera boundary discontinuities on the 1982-1985 deformation. Such models might explain the uplift deformation, but they still do not explain the subsequent subsidence phase since 1984.

*Battaglia et al. (2006)* model the location, geometry and density of the source, inverting levelling, trilateration and gravity measurements collected between 1980 and 1995. They found two different sources for the first uplift period and the subsequent subsidence phase. The best fitting source for the 1980–84 inflation is an horizontal penny-shaped crack with a density from 142 to $1115 kg/m^3$. The source best fitting the deflation period (1990–95) is a vertical spheroid with density between 902 and $1015 kg/m^3$. These results exclude the intrusion of magma, and indicate the migration of fluid to and from the caldera hydrothermal system as the cause of ground deformation and consequent unrest. *Amoruso et al. (2007)* have demonstrated that this large mismatch between inferred intrusion density for spherical and penny-shaped sources is at least partially a consequence of the homogeneous half space assumption, showing that neglecting crustal layering can lead to strong density underestimation.

*Lundgreen et al. (2001)* inverted the InSAR data from 1992 to 1998 and found a slightly shallow source between 2.5 and 3 km depth; this result is very similar to the horizontal sill proposed by *Dvorak and Berrino (1991)* to best fit the leveling and trilateration data at CF, during the unrest periods from 1969 to 1989; this could be suggest that the deformation pattern has remained the same during the uplift and the subsidence periods.

## 1.2 Recent bradyseisms

After the larger uplift of 1982-1984, mini-uplifts with a few cm amplitude occurred around 1989, 1994, 2000, and 2006 *(Amoruso et al., 2007)*. Since 2005 the subsidence, that affected the CF area after the 1982-1984 uplift, seems to be over and is mostly uplifting at an accelerating rate (www.ov.ingv.it/ov/campi-flegrei.html). Many fumaroles are still active in the area where an important geothermal field is present, like the Solfatara area. Currently, the Solfatara area is a set of fumarolic activity and is affected by an intense process of diffuse degassing of volcanic -hydrothermal $CO_2$ *(Chiodini et al., 2010). Manconi et al. (2010) analyzed* SBAS-DInSAR data (see later in the text) of the period 1992-2008

and observed that the deformation is entirely related to the unrest of a small source located in the center of the caldera at about $3\,km$ depth. *D'Auria et al. (2011) analyzed* the ground uplift and sismicity from 1989 to 2010 and proposed that the episodes were triggered by the injection of hot fluids, with a significant magmatic component, into the geothermal reservoir located beneath the CF area. They found a source at a depth of about $2.5\,km$.
In *D'Auria et al. (2012)* they determined the temporal and spatial distribution of volumetric strain sources up to 5 km depth and the results have shown complex spatial and temporal patterns and a positive strain sources (expansion) migrating upward (in 2000 and 2006). They have interpreted them as hot fluid batches injected at the bottom of the geothermal reservoir, migrating upward and reaching the surface. The injection of fluid batches does not occur at the center of the caldera, but along its borders and the identified injection episodes occur in different points.
In 2000 and 2006, the injected fluids migrated, subsequently, toward the center of the caldera. In *Troise et al., (2008)* is studied the 2004-2006 uplift $(\sim 4\,cm)$ using leveling vertical data and continuous GPS horizontal data, the ratio among maximum horizontal and maximum vertical displacement is equivalent to that observed during the uplift of 2000 and the shape of vertical pattern is vary similar to the 1982-1984 large uplift. The same period is analyzed in *Amoruso and Crescentini (2007)* to highlight the importance of using a layered medium, rather than an homogeneous one, in the inversion of geodetic data; they conclude that, using a realistic layered half-space, with properties constrained by local seismic data, it is possible to fit all the deformation data with an horizontal crack source. In this last two years, a considerable uplift has drawn attention from both scientists and civil protection; from the middle of 2011 there is an uplift with two different acceleration ratios between June 2010 and December 2011 and from January 2012 until June 2013. From 2011, cumulative uplift is about 14 cm.

## 1.3 Monitoring network

Precise monitoring of the ground deformation in Phlegrean area began in 1970 and was continuously improved during subsequent years, following the dynamic evolution of the area *(Berrino et al. 1984)*. In this thesis, different types of data are used, levelling, geodetic precise traversing, Synthetic Aperture Radar (SAR) and continuous Global Positioning

System (cGPS) data.

### 1.3.1 Leveling data

Leveling is the measurement of geodetic height, along a route of consecutive benchmarks, using an optical leveling instrument and a rod and provides measures of the elevation difference between benchmarks by sighting adjacent rods. Two methods are usually applied: geometric (or direct) leveling and trigonometric (or indirect) leveling . The first one, used in the CF area, is usually more precise; the difference of height between two points, is determined by differences of readings to the staffs placed on those points.
The vertical ground deformation at CF has been measured by precision leveling since 1969. The current leveling network, covers the entire Phlegrean area, from Naples to Miseno on a surface of $\sim 160 km^2$, is made by 330 benchmarks over a total length of about 135 km in 14 circuits *(Troise et al., 2008)*, as shown in figure 1.3 *(Del Gaudio et al., 2009)*. The reference benchmark, located in the area of maximum uplift, near the Serapeo is the

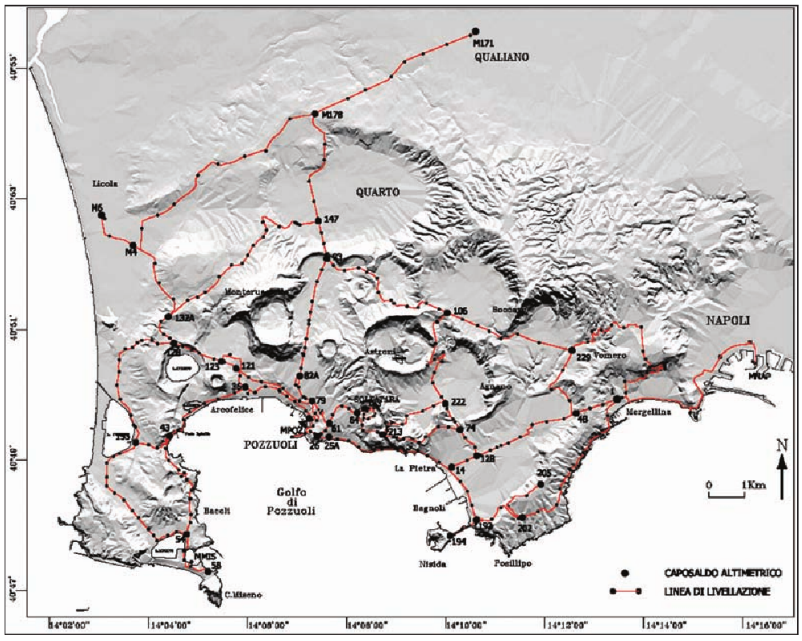


Figure 1.3: Current leveling network (from Del Gaudio et al., 2009)

25A (position in figure 1.4). Several leveling surveys were carried out before, during and after the major 1982-1984 unrest, including measurements in January 1980, January 1981,

and June 1983 ( *Dvorak and Berrino, 1991*). Leveling surveys subsequent to June 1983 include new leveling lines covering important parts of CF, including Solfatara.
The number of benchmarks changes from survey to survey, and generally increases over time. As it is shown in figure 1.4 in January 1980 and January 1981 there are four routs (A,B,C,D) and the Solfatara area is not covered, while during the period June 1983 - December 1992 there are other four routs (E,F,G,H) and the rout "G" cover the Solfatara area.

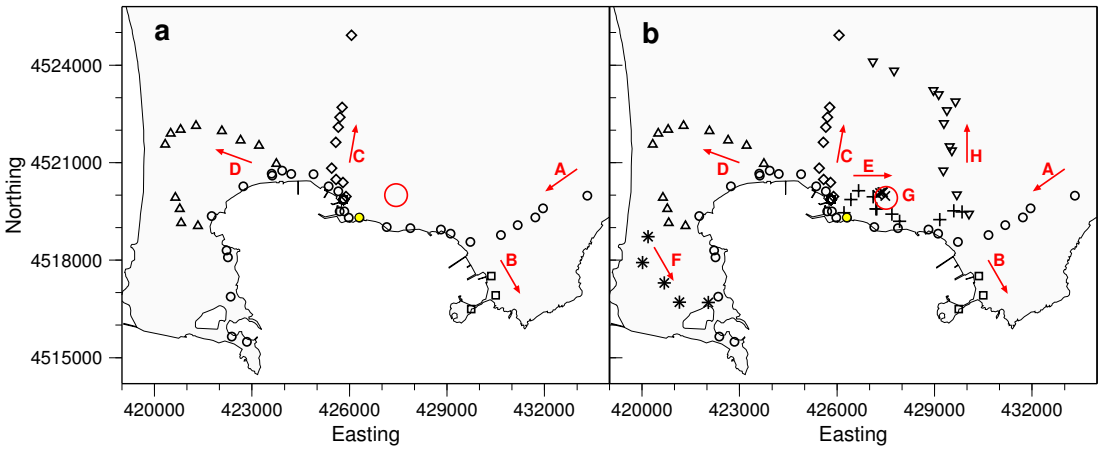


Figure 1.4: Leveling routs in different periods. a) measured in January 1980 and January 1981 b) measured during the period June 1983 - December 1992; yellow filled circle, benchmark 25A position; red empty circle, Solfatara area.

To get coeval leveling and EDM data (carried out in June 1980 and June 1983), June 1980 leveling data have been estimated by averaging the January 1980 and January 1981 surveys. We have not used benchmarks whose coordinates differ by more than 200 m between our dataset and the INGV WebGIS (http://ipf.ov.ingv.it/cf gis.html). Original data (section height differences) are not available and only adjusted benchmark heights with respect 114 to a reference benchmark *(Ghilani and Wolf , 2012)* can be used. We have not 115 used benchmarks whose height time histories include anomalous steps, e. g. because of 116 benchmark damage and reconstruction. We have removed benchmarks whose uplift histories include evident anomalous values and steps – e. g. because of benchmark damage and reconstruction – from the dataset. The final set consists of 53 adjusted benchmark uplifts. leveling measurements can be affected by both systematic correlated errors, that may be introduced by miscalibrated rods or refraction effects, and random measurement

errors *(Amoruso and Crescentini, 2007)*. In this thesis, only adjusted benchmark heights are used and the uplift covariance matrix is not diagonal and cannot be computed exactly because of lack of information on original measurements and the adjustment procedure.

### 1.3.2 Geodetic precise traversing data

Leveling data give vertical displacements of the area, to have the horizontal one geodetic precise traversing surveys are used, by distance and angular measurements. EDM (Electronic Distance Measurement) provides the horizontal distance between two points by an indirect determination of the travel time of a beam of light from the instrument to the reflector and back, applying corrections for atmospheric conditions. Angular measurements are obtained using the electronic theodolite, a precision instrument with a movable telescope mounted within two perpendicular axes (the horizontal or trunnion axis and the vertical axis). These measurements are collected on a polygonal, the set of measured points, connected to each other. There are two types of possible polygonals, opened and closed, and one of the most important aspect is that every point of the polygonal allow to watch the successive point. Geodetic precise traversing surveys – distance (EDM) and angular measurements – were carried out, at CF, in June 1980 and June 1983 by researchers of Bologna University, Italy (*Barbarella et al., 1983*). They provide horizontal displacement data that have been widely used in the past to model the major 1982-1984 unrest. As pointed out by *Trasatti et al. (2011)*, previous works *(Dvorak and Berrino, 1991; Battaglia et al., 2006; Amoruso et al., 2008)* often wrongly referred data to September 1983.

No additional survey was carried out between 1980 and 1983. An additional minor survey was conducted in November 1984; it involved only distance measurements (EDM) of three of the previous benchmarks and is not considered here. Later data share the same difficulty and/or show low signal-to-noise ratios *(Battaglia et al., 2006)*. Unfortunately, 1980 distance and angular measurements are no longer available (M. Barbarella, personal communication). *Barbarella et al. (1983)* give 1983 adjusted benchmark coordinates and 1980-to-1983 benchmark displacements (figure 1.5 (a)) with respect to a local reference system (origin at benchmark S, y axis from S to A) (see inset in figure 1.5 (a)).

Because of deformation, both the position of benchmark S and the azimuthal direction of

the y-axis might change between 1980 and 1983. We have checked if 1980-to-1983 benchmark displacements show an approximately radial pattern with respect to some point, in a fixed reference system. We have sought a rigid transformation (combination of S-A rotation and axis origin translation) able to make horizontal displacements as radial as possible with respect to some radiating center (the black star in figure 1.5 (b)) , through a best-fit procedure. Since the transformation is nonlinear, we have used Adaptive Simulated Annealing (see later in text) to minimize misfit between directions of transformed displacements and unit radial vectors. The translation gives the position of the radiating center with respect to S; the rotation angle gives S-A azimuthal change. The best-fit ra-

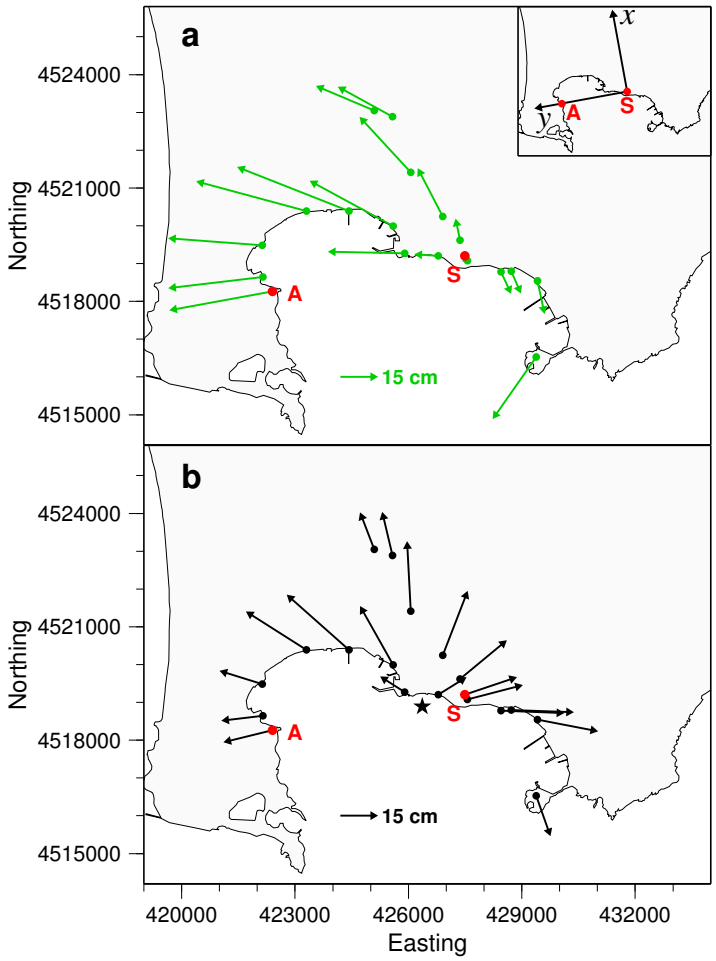


Figure 1.5: Positions and displacements of EDM benchmarks. a) 1980-1983 displacements relative to the local reference system in *Barbarella et al. (1983)* as shown in the inset. b) 1980-1983 displacements with respect to the radiating center (black star).

diating center is indicated by the black star in figure 1.5 (b); retrieved rotation angle is negligible ($< 10^{-3}$ deg). Figure 1.5 (b) gives benchmark displacements with respect to the radiating center (neglecting the very small rotation) and demonstrates that horizontal displacements are quasi-axisymmetric, possibly apart from benchmark C. Horizontal displacements are consequently consistent with a quasi-axisymmetric deformation source located below the radiating center.

### 1.3.3 RADAR data

RADAR stands for "RAdio Detection And Ranging". By virtue of sending out pulses of microwave electromagnetic radiation this type of instrument can be classified as an "active sensor", it measures the time between pulses and their reflected components to determine distance. Radar uses microwaves with wavelength between $1\,mm$ and $1\,m$ with frequencies from $3 \cdot 10^{11}\,Hz$ to $108\,Hz$; these long wavelengths have the notable advantage of being able to penetrate clouds and being insensitive to weather conditions. Unlike instruments that look straight down, radar data are collected looking off to the side. The antenna is an essential constituent of the radar; it radiates or receives electromagnetic energy. The antenna focuses the power in a given direction to increase the sensitivity, controlling the explorer beam to analyze a certain covering area. The radar data depends on the intensity and the return time, from the surface, of the reflected signal; in this way we obtain the distance between the target and the antenna (slant range). The illumination angle decreases from positions close to the sensor (near range) to positions more distant (far range), so those points with the same distance on the horizontal surface in the image are closer in near range than in far range. The resolution in slant range is along the line of sight (LOS), while the resolution in ground range is the slant range resolution of the projection on the reference surface. The image in ground range is simply the geometric correction of that in slant range. For an ideal smooth, surface correction is ground range = slant range/ $\sin(i)$, where $i$ is the local incidence angle.

#### 1.3.3.1 SAR data

Obviously there are physical limits to the length of the antenna used in a radar; first of all, the maximum length of the structure that can be mounted on an aircraft or on a satellite;

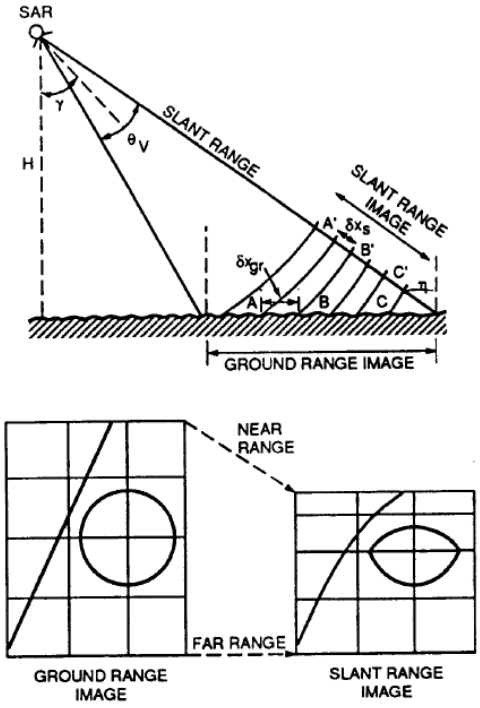


Figure 1.6: Effects of the slant range and ground range on the images (*Massironi, 2004*)

to solve this problem has been developed an approach, in which the antenna length is increased in a virtual way, thus having a larger antenna. Systems that use this approach are called Synthetic Aperture Radar (SAR); these sensors use microwaves with typical wavelengths between $1cm$ and several meters and have physical characteristics similar to those of the real aperture radar.

A longer virtual antenna is obtained by using the forward motion of the platform and using, for a same target, a large number of backscattered signals. The radar antenna, mounted on a satellite or on a plane, moves with a certain speed; each time, when it emits the pulse and receives the echo, it is located in a different position because of moving of platform. Collecting and storing all these echoes, related to different moments, seems that they are derived from different portions of the same antenna, exceed the actual dimension of that mounted on the satellite (see figure 1.7).

The data, used in this thesis, are surface displacements obtained through interferometric synthetic aperture radar (InSAR); this is a technique that analyzes the phase difference between two SAR images acquired from slightly different positions. This phase difference is related to the topography of the scene and can be used to generate models of ground

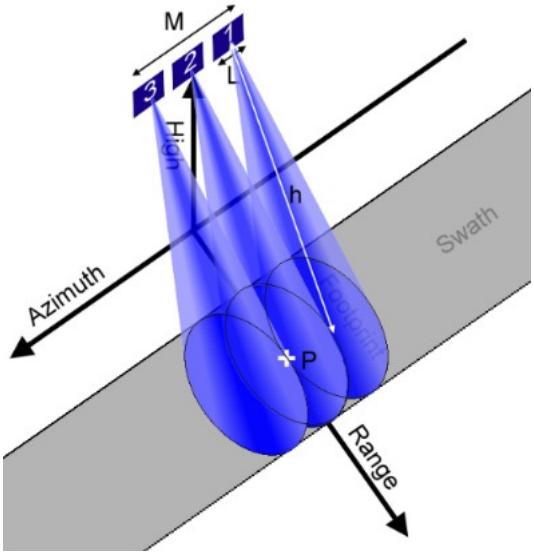


Figure 1.7: Schematic example of Synthetic Aperture Radar. The actual antenna length is L while the length of the synthetic antenna is M. (www.wikipedia.org/wiki/Radar_ad_apertura_sintetica)

elevation called Digital Elevation Models (DEMs).

The result of this technique is an interferogram; it is a map of the phase differences obtained by two SAR images that record the same place from different look angles. The two images, to be compared, must have the same geometry and firstly must be co-registered, using a correlation procedure to find the offset and difference in geometry between the two amplitude images. One of these two SAR images must be assigned as the master (reference) image and another one is the slave (match) image. Through the whole coregistration process, only the slave image will be shifted in coarse coregistration and resampled in fine coregistration. The technique used in this case is a more advanced type of SAR interferometry called Differential Interferometry (DlnSAR). This technique uses to determine the ground displacement occurred through the comparison between the two images captured at different times with with an accuracy of centimeter. In this thesis, the ERS (ERS-1 and ERS-2) and ENVISAT satellites data are used, both of these satellites move on an almost polar orbit around the Earth, so it's possible to have two images of the same place; when the satellite has an ascending orbit (from south to north) e when has a descending orbit (from north to south); in the first case the place is observed by the satellite from the west, while in the second case from the East, so we have two looking angles (see figure 1.8).

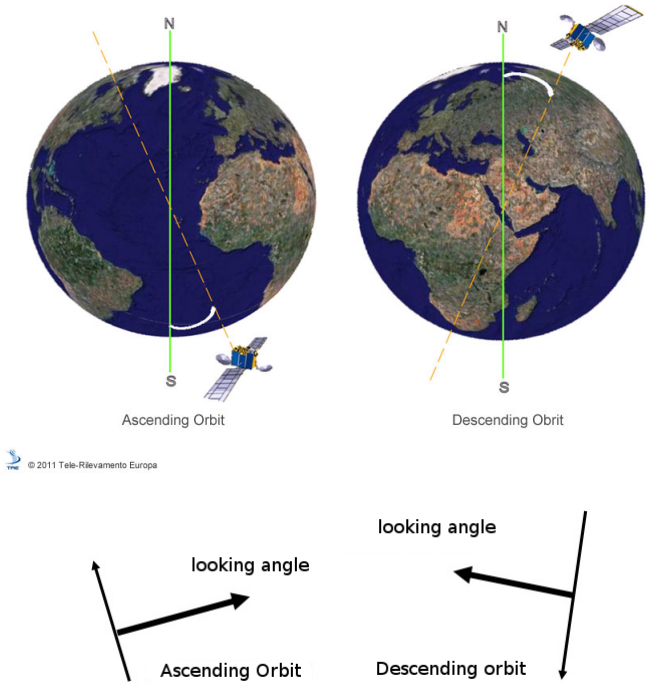


Figure 1.8: (www.treuropa.com) Ascending and descending orbit looking angles *(Manconi et al., 2010)*.

We use a temporal subset of pixel-wise displacements relative to every acquisition date in the period 1993-2010 produced by applying SBAS-DInSAR technique to a set of ERS (ERS-1 and ERS-2) and ENVISAT SAR images acquired on ascending (track 129, frame 809) and descending (track 36, frame 2781) orbits. SBAS-DInSAR technique selects image pairs to generate interferograms which are characterized by small temporal and spatial separation between the acquisition orbits *(Manconi et al., 2010)*. The accuracy of the technique has been quantified to be $\pm 0.5\,cm$ for measured line-of-sight (LOS) displacements, from comparisons with leveling and GPS data *(Casu et al., 2006)*. Differences between observed and predicted (on the basis of a deformation source model) displacements are expected to be larger, at least because data exhibit clear annual oscillations whose amplitude (up to about 1 cm) varies over space and time, and because of long-term ground instabilities *(Wyatt, 1989)*. Moreover, each displacement map may suffer a (small) uniform bias because displacements are computed with respect to a reference pixel, assumed to be stable. Errors on final results, can be produced from the atmospheric contribution to the interferometric phase. In this thesis, these kinds of errors are neglected because generally

present particularly in large elaboration areas.

### 1.3.4 cGPS data

The Global Positioning System (cGPS) is a satellite-based navigation system made up of a network of 24 satellites placed into orbit by the U.S. Department of Defense (DoD). It provides location and time information in all weather conditions, anywhere on or near the Earth where there is an unobstructed line of sight to four or more GPS satellites. Only four satellites are sufficient to calculate the four necessary informations (latitude, longitude, height and time) and to have the three-dimensional localization of a point on Earth surface. The GPS project was developed in 1973 but become fully operational in 1995. INGV-Osservatorio Vesuviano manages the NeVoCGPS (Neapolitan Volcanic Continuous GPS) monitoring network (figure 1.9), this consists of 29 stations (13 at Campi Flegrei area, 8 at the Vesuvio are, 4 on the isle of Ischia, 1 on the isle of Procida, 1 in the center of Naples and 2 on the eastern cost) with a configuration that guarantees constant and fast 3D information about the dynamics of the Neapolitan volcanic area *(Bottiglieri et al, 2010)*. The network began operating of the end of the 1990s but only since 2000 it has a stable configuration *(De Martino et al., 2014)*. Data, that are managed by remote control, are recorded at 30 second intervals in session of 24 hours and then using the Ultra-rapid International GNSS Service (IGS) processed on a daily basis. When the IGS final products become available, the data are reprocessed on a weekly basis. To minimize the contribution of tectonic movements, the GPS position time series are estimated relative to the stable station ENAV ($40.582°N, 14.335°E$), located on the limestones of Sorrento Peninsula, outside the volcanic area.
The horizontal cGPS velocities is removed from all cGPS stations. *Bottiglieri et al. (2010)* show that any ground deformations modify the distribution of the time-series amplitude so significantly that it can be used as the marker of an effective source-driven deformation.
An uncorrelated formal error equal to 0.3 cm to northward and eastward displacements and equal to 0.5 cm to vertical displacements is assigned. Currently there are 14 stations at CF, in table 1.10 there are their positions at Campi Flegrei. In this thesis, data until October 2013 and that have different starting date, as shown in figure 1.10, are analyzed. Big advantages of GPS data, compared to other, is that the full displacement vector is resolved.

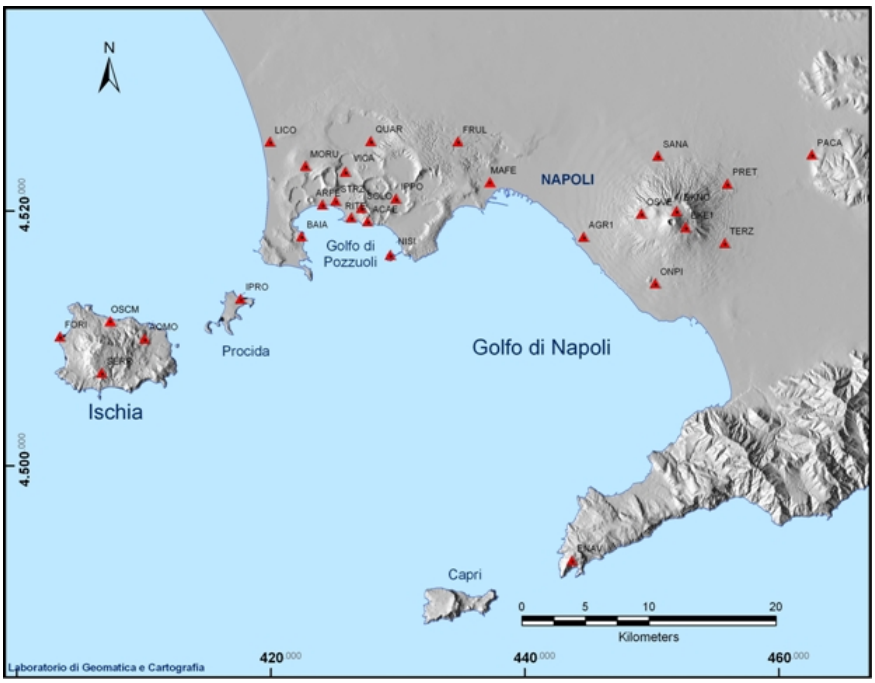


Figure 1.9: Neapolitan Volcanic Continuous GPS monitoring network (from http: //www.ov.ingv.it/ov/attivita-recente-di-ischia/212.html)

| CAMPI FLEGREI | |
|---|---|
| i.d. | on since |
| QUAR | 1999 |
| IPPO | 1999 |
| BAIA | 1999 |
| ACAE | 2000 |
| RITE | 2000 |
| ARFE | 2000 |
| MORU | 2000 |
| STRZ | 2008 |
| SOLO | 2009 |
| VICA | 2009 |
| NISI | 2009 |
| LICO | 2003 |
| FRUL | 2008 |
| MAFE | 2010 |

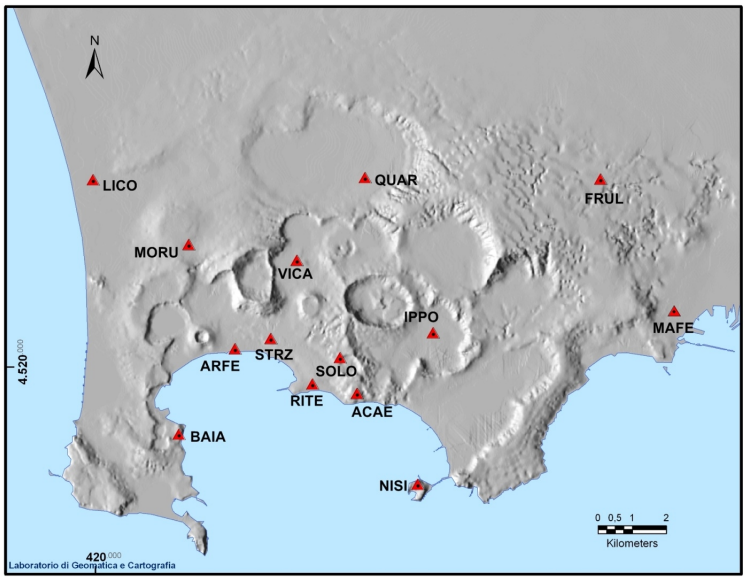


Figure 1.10: Starting date of acquisitions and positions of GPS station at Campi Flegrei caldera (from http: //www.ov.ingv.it/ov/it/campi-flegrei/attivita-recente.html)

# Chapter 2

# Models for earthquake volcano deformation

The aim of this thesis is to find a simple model source that explains the CF deformation field. In this chapter there are the mathematical formulations of the model sources tested.

## 2.1 Displacements due to a single force

In geophysics is known that, for a linear elastic material, the strain $\varepsilon$ is proportional to stress $\sigma$

$$\sigma_{ij} = C_{ijkl}\varepsilon_{kl} \tag{2.1.1}$$

This equation is known as generalized *Hooke's law*, where $C_{ijkl}$ is a symmetric fourth-rank tensor; this tensor consists of 81 coefficients but only 21 are independents because of the inherent symmetries of $\sigma$, $\varepsilon$, and $C$. For isotropic media (which have the same physical properties in any direction), $C$ can be reduced to only two independent numbers, the Lame constants $\lambda$ e $\mu$. $\mu$ is the shear modulus that relates shear stress to shear strain although the shear modulus must be positive while the Lame's first parameter, $\lambda$ can be negative. So *Hooke's law* becomes:

$$\sigma_{ij} = 2\mu\varepsilon_{ij} + \lambda\varepsilon_{kk}\delta_{ij} \tag{2.1.2}$$

where $\delta_{ij}$ is the Kronecker delta. For a point force, $F_k$, applied at the origin, the equilibrium equation is

$$\frac{\partial \sigma_{ij}}{\partial x_j} + F_k \delta_{ik} = 0 \tag{2.1.3}$$

where repeated indices are summed. The solution to this equation is the Green's function

$$G_{ik} = \frac{1}{4\pi\mu}\left[\frac{\delta_{ik}}{r} - \frac{1}{4(1-\nu)}\frac{\partial^2 r}{\partial x_i \partial x_k}\right] \tag{2.1.4}$$

where $G_{ik}$is the displacement in the $i$-direction from a unit point force in the $k$-direction. This is called Somigliana's tensor and through it, it is possible to find the displacement due to a single force $f_k$

$$u_i = \int_V f_k(\mathbf{x}') G_{ik}(x, x') dV \tag{2.1.5}$$

The displacement due to a single force is the simpler analyzed case, but starting from this simple source it is possible to obtain other sources through different combinations.

### 2.1.1 Elastic homogeneous half-space

The hypothesis of an infinite elastic medium is not acceptable for the Earth because of the Earth surface that is not negligible. *Okada (1992)* found a complete set of analytical expressions in a unified manner for the internal displacements and strains due to shear and tensile faults in an half-space for both point and finite rectangular sources. The Earth can be represented locally as an homogeneous elastic half-space and introduce the surface discontinuities between the medium and area, means introducing a new boundary condition, that the fractions are zero on the surface. It is possible to ignore Earth curvature and modeling the free surface as planar but the problem is complicated by the necessity to satisfy boundary conditions on two surfaces, the ellipsoid and the free surface. This problem can be solved by using the "method of images". The basic idea to solve this problem is to imagine the source embedded in the half-space at a fixed depth from free surface and using the same equations for an infinite space without the discontinuities but introducing

a new "image" source on the far side of the free surface. The half-space Green's functions introduce stresses that decay as 1/(distance)^3 away from the image point and so, for a deeply buried ellipsoid, are small but vary over its surface. Chosen the coordinate system in figure 2.1, if $u_i^j(x_1,x_2,x_3,\xi_1,\xi_2,\xi_3)$ is the $i$th component of the displacement

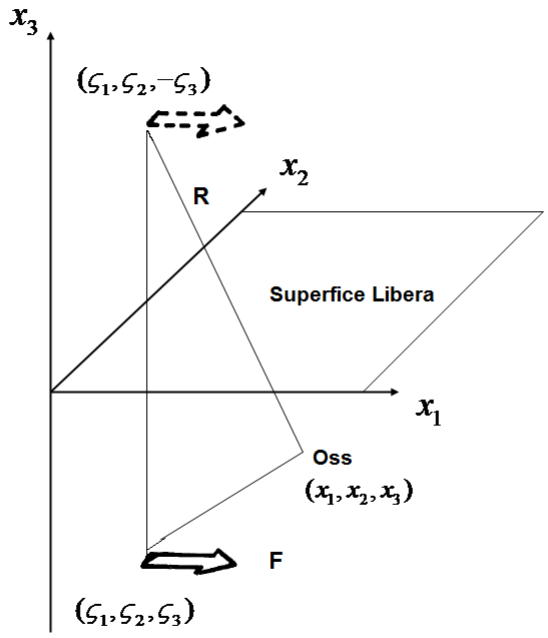


Figure 2.1: Schematics forces to simulate a homogeneous half-space (*from Okada, 1985*)

at $(x_1,x_2,x_3)$ due to the $j$th direction point force of magnitude $F$ at $(\xi_1,\xi_2,\xi_3)$, it can be rewritten from the formula by *Mindlin(1936)* as follows:

$$u_i^j(x_1,x_2,x_3) = u_{iA}^j(x_1,x_2,-x_3)\text{-}u_{iA}^j(x_1,x_2,x_3) + u_{iB}^j(x_1,x_2,x_3) + x_3 u_{iC}^j(x_1,x_2,x_3) \quad (2.1.6)$$

where:

$$\begin{cases} u_{iA}^{j} = & \frac{F}{8\pi\mu}\left\{(2-\alpha)\frac{\delta_{ij}}{R}+\alpha\frac{R_iR_j}{R^3}\right\} \\ u_{iB}^{j} = & \frac{F}{8\pi\mu}\left\{\frac{\delta_{ij}}{R}+\frac{R_iR_j}{R^3}+\frac{1-\alpha}{\alpha}\left[\frac{\delta_{ij}}{R+R^3}+\frac{R_i\delta_{j3}-R_i\delta_{i3}(1-\delta_{j3})}{R(R+R_3)}-\frac{R_iR_j}{R(R+R_3)^2}(1-\delta_{i3})(1-\delta_{j3})\right]\right\} \\ u_{iC}^{j} = & \frac{F}{8\pi\mu}(1-2\delta_{i3})\left\{(2-\alpha)\frac{R_i\delta_{j3}-R_j\delta_{i3}}{R^3}+\xi_3\left[\frac{\delta_{ij}}{R^3}-\frac{3R_iR_j}{R^5}\right]\right\} \end{cases} \tag{2.1.7}$$

with

$$R_1 = x_1-\xi_1, R_2 = x_2-\xi_2, R_3 = -x_3-\xi_3, R^2 = R_1^2+R_2^2+R_2^3 \tag{2.1.8}$$

where, $u_{iA}^{j}(x_1,x_2,-x_3)$ is the displacement field due to a single force in $(\xi_1,\xi_2,\xi_3)$ in an infinite medium, the term $u_{iA}^{j}(x_1,x_2,x_3)$ is the contribution from the image source placed at $(\xi_1,\xi_2,-\xi_3)$ in the infinite medium. These two terms vanish when combined each other, because equal and opposite and the last two terms are depth dependent. If $x_3 = 0$, on surface, the first and the second term cancel each other, and the fourth term vanishes. The remaining term, $u_{iB}^{j}(x_1,x_2,x_3)$, reduces to the formula for the surface displacement field due to a point single force in a half-space. Note that the use of the image source is correct only if the source's dimension is much less than its depth.

### 2.1.2 Elastic layered half-space

Until now, the earth has been modeled as a homogeneous half-space, but this approximation, although guarantees a more accurate solution than that obtained in an infinite half-space, does not take into account the stratification of the Earth. The importance of taking into account the stratification is evidenced by different authors *(Amoruso, Crescentini and Fidani, 2004, Amoruso and Crescentini, 2007,* etc). The Green's functions for a half-space have been found by *Mindlin (1936)*, in terms of relative coordinates, as $G(\mathbf{r}-\mathbf{r}')$, while in the layered case are $G(\mathbf{r},\mathbf{r}') = G(x-x',y-y',z,z')$, because the stratification is vertical only. The vertical profile of density, used in this thesis, is obtained from the 1D $V_p$ model in the work by *Judenherc and Zollo (2004)* and the Nafe-Drake curve *(Ludwig et al., 1970)* taking into account the drained response of the medium by setting the Poisson's ratio to 0.25 at all depths. Even if the Nafe-Drake curve may be inappropriate to an explosive volcanic environment like CF, nevertheless this density profile is very

| depth (km) | Vp (km/s) | Vs (km/s) | density (kg/$m^3$) |
|---|---|---|---|
| 0.00 | 1.60 | 0.92 | 1800 |
| 0.62 | 2.50 | 1.44 | 2100 |
| 1.40 | 3.20 | 1.85 | 2270 |
| 1.55 | 3.90 | 2.25 | 2380 |
| 2.73 | 3.95 | 2.28 | 2400 |
| 3.92 | 5.20 | 3.00 | 2580 |
| $\geq 4.03$ | 5.92 | 3.42 | 2700 |

Table 2.1: Vertical profile of density

similar to the one inferred by the Italian Oil Agency from gravity anomalies (2000 kg/m3 , above 1-km depth; 2200 kg/m3 , 1 to 2.4 km; 2400 kg/m3 , 2.4 to 3.2 km; 2600 kg/m3 below 3.2-km depth) *(AGIP , 1987*). Values for intermediate depths are obtained by linear interpolation between adjacent listed depths.
An important aspect is that the layering effects are larger on horizontal ground displacements than vertical ones and if synthetics data are generated in an homogeneous half-space and inverted in a layered half space, retrieved source parameters depend on the relative weight of horizontal and vertical displacement data in the misfit function (*Amoruso et al. 2007*). The Green's functions are determined using the PSGRN code (*Wang, 2005*) using the layering in table 2.1. This algorithm computes the Green's functions for four main sources (double forces strike-slip, double forces dip-slip, a compensated linear vertical dipole (CLVD) and an inflation) at different depths (see later in text).

## 2.2 Sources models

In this thesis, different types of sources models are tested:

1. one pressurized point spheroidal cavity having a vertical axis of symmetry *(*5 free parameters*, Amoruso et al., 2008),*

2. one pressurized finite horizontal circular crack (5 free parameters*, Crescentini and Amoruso, 2007),*

3. one pressurized finite spheroidal cavity having a vertical axis of symmetry, mathematically modeled under the quadrupole approximation (6 free parameters*, Amoruso*

*and Crescentini, 2011),*

4. one pressurized finite triaxial ellipsoidal cavity, mathematically modeled under the quadrupole approximation (10 free parameters*, Amoruso and Crescentini, 2011),*

5. one rectangular uniform-opening tensile fault (8 free parameters*, Okada, 1985; Wang et al., 2006),*

6. one moment tensor (9 free parameters*, Aki and Richards,1984)*.

In this session are given mathematical formulations about all these sources.

### 2.2.1 Moment tensor

For a seismic source on an earthquake dislocation model, slip is modeled in terms of oppositely directed point forces, which together form a couple. However, a couple has a net torque, so its sudden appearance at the time of an earthquake would develop an accelerating angular momentum; to avoid this, a second couple must be added with an equal and opposite torque and forces at right angles to the first. The result is a double-couple model.
Defining $\delta z$ the distance between two surfaces of the displaced crack, the normal to the crack area, **S**, parallel to the z-axis and **b** the horizontal displacement in x-direction, the stress is $b/\delta z$ and the force is $\mu(b/\delta z)S$. If $G_{ix}(r)$ is the Green's function associates to a single force, the displacement due to a couple of forces is

$$\begin{aligned} u_i(couple) &= force\left(G_{ix}(r+\frac{\delta z}{2}) - G_{ix}(r-\frac{\delta z}{2})\right) \\ &= \frac{\mu bS}{\delta z}\left(G_{ix}(r+\frac{\delta z}{2}) - G_{ix}(r-\frac{\delta z}{2})\right) \\ &= \mu bS\left(\frac{\partial G_{ix}}{\partial z}\right) \end{aligned} \tag{2.2.1}$$

the displacement due to a double couple of forces is obtained by adding a compensating couple at right angles, of the same strength but opposite torque

$$u_i(double\,couple) = \mu bS\left(\frac{\partial G_{ix}}{\partial z} + \frac{\partial G_{iz}}{\partial x}\right) \tag{2.2.2}$$

in this case the force couple is made up of two equal and opposite forces displaced normal to their line of action. Another important combination of force is formed by three doublets that make a center of dilatation

$$u_i(center\,of\,dilatation) = \lambda bS\left(\frac{\partial G_{ix}}{\partial x} + \frac{\partial G_{iy}}{\partial y} + \frac{\partial G_{izx}}{\partial z}\right) \tag{2.2.3}$$

this last combination is used, for example, in the next session to model a spherical source. Schematic examples of different sources are shown in figure 2.2. There are six couple of

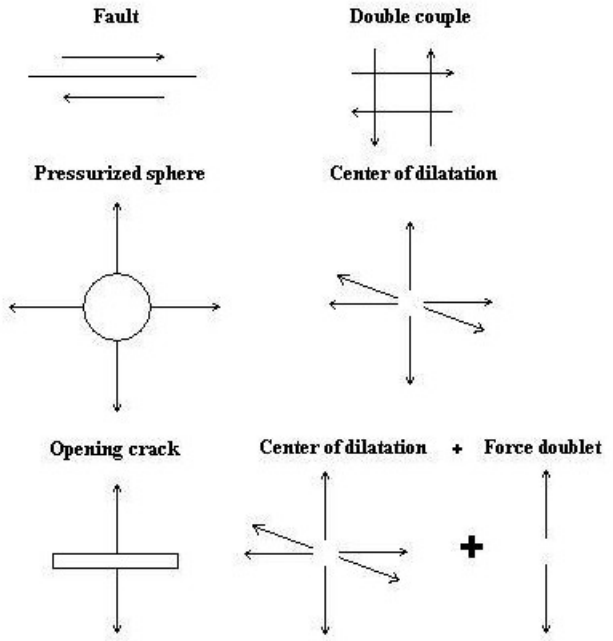


Figure 2.2: Schematic examples of different sources with their point forces representation (Figure from *Stacey and Davis, 2009)*

forces along main axes with a net torque, but in a elastic media a couple of forces with a zero net torque produces a displacement. So there are nine different types of couple of forces as in figure 2.3. So a source schematized with more couple of force is described by

a second order tensor $M_{ij}$, the moment tensor, where index $i$ is the force's direction and $j$ is the direction of the arm's couple. In other words, the moment tensor is the mathematical representation of seismic source.

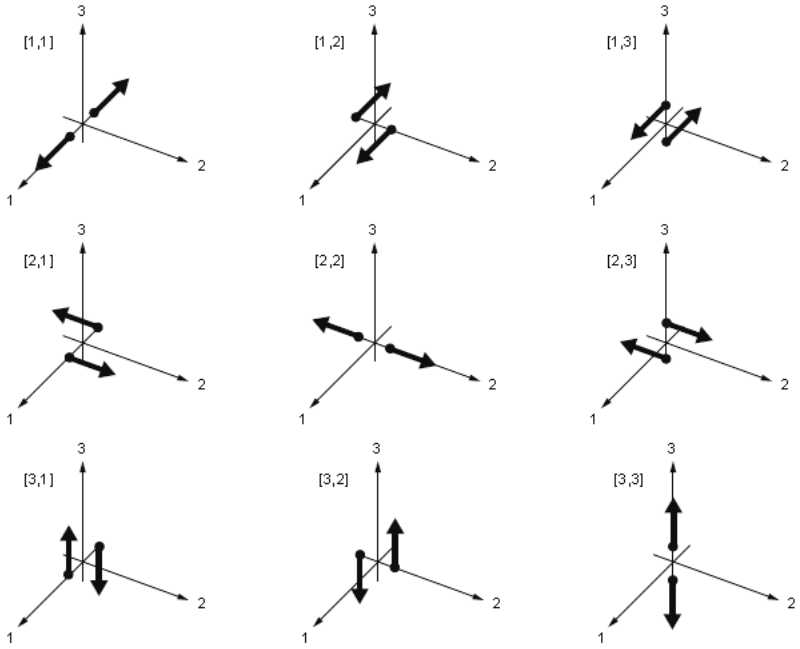


Figure 2.3: The nine generalized couples of the seismic moment tensor (Figure from *Aki and Richards, 2002*)

### 2.2.2 The Mogi model

In this thesis, different kind of "model" sources are tested to explain the data. The most simple is a spherical source so-called the "Mogi model" after *Mogi (1958)*. The sphere has radius $a$, with center at depth $d$ beneath the free surface. $r$ is the radial distance from the center of the sphere and $\rho$ is the distance from the center of symmetry along the free surface (see figure 2.4). For $r = a$, $\sigma = -p$ so the radial stress equals a uniform pressure p on the chamber walls, where the shear traction vanished.
Vertical and horizontal displacements, in an elastic homogeneous half-space, are:

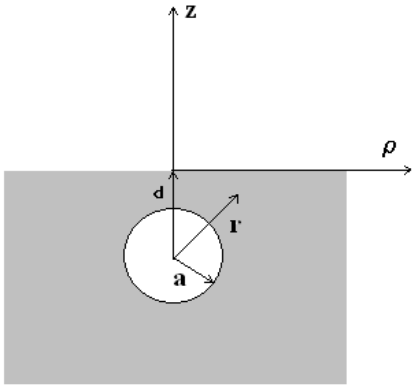


Figure 2.4: Problem geometry. The sphere has radius $a$, center depth $d$, radial distance from the center $r$ and $\rho$ is the distance from the center of symmetry along the free surface.

$$u_z = \frac{(1-\nu)pa^3}{\mu}\frac{d}{(\rho^2+d^2)^{3/2}} \tag{2.2.4}$$

$$u_\rho = \frac{(1-\nu)pa^3}{\mu}\frac{\rho}{(\rho^2+d^2)^{3/2}} \tag{2.2.5}$$

Vertical displacements are symmetric as shown in figure 2.5. Notice that the ratio of horizontal to vertical displacement is $u_\rho/u_z = \rho/d$, which means that the displacements, at the free surface, are directed radially away from the center of the spherical source, as they were in full-space. This is not true everywhere in the half-space; in general the displacements are not radial except near the chamber walls for small $a/d$ and at the free surface. The term $pa^3$ joins the pressure change to the cavity radius and for now it is not possible to estimate the size of the cavity and the pressure change independently. It is possible, however, to estimate the volume change $\triangle V$ . The radial displacement is:

$$u_r = \frac{pa^3}{4\mu r^2} \rightarrow u_r(r=a) = \frac{pa}{4\mu} \tag{2.2.6}$$

$$\triangle V = 4\pi a^2 u_r = \frac{\pi p a^3}{\mu} \tag{2.2.7}$$

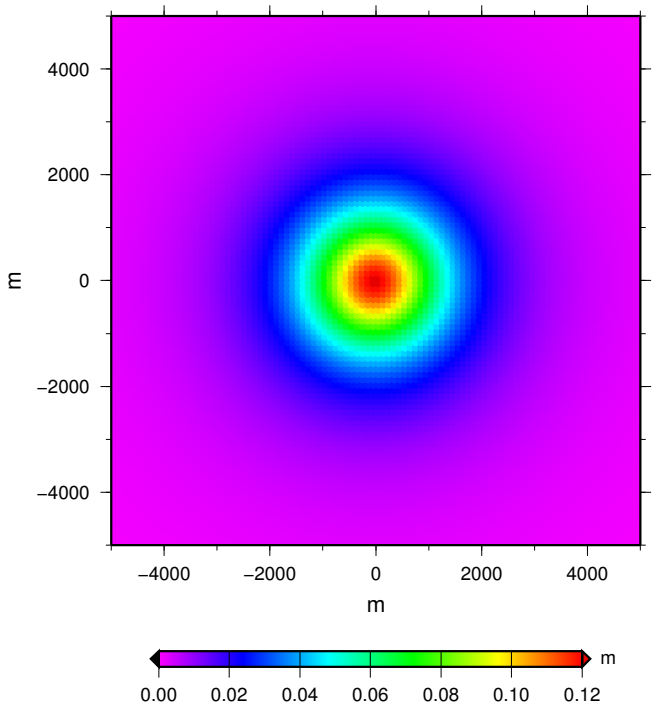


Figure 2.5: 2D vertical displacement due to a spherical source at depth 1500m with radius 200m, pressure $3 \cdot 10^3$Pa and embedded in a Poisson's media. The sphere's center is in (0,0).

because $4\pi a^2$ is the sphere surficial area.

$\triangle V$ is the cavity volume change, which is equivalent to a pressure change of the cavity. So the precedent equations become

$$u_z = \frac{(1-\nu)\triangle V}{\pi} \frac{d}{(\rho^2+d^2)^{3/2}} \tag{2.2.8}$$

$$u_\rho = \frac{(1-\nu)\triangle V}{\pi} \frac{\rho}{(\rho^2+d^2)^{3/2}} \tag{2.2.9}$$

Using the moment tensor

$$M = (\lambda + 2\mu)\delta V \begin{pmatrix} 1 & 0 & 0 \\ 0 & 1 & 0 \\ 0 & 0 & 1 \end{pmatrix} \tag{2.2.10}$$

Recalling that $V = \frac{4}{3}\pi a^3$ from eq. 2.2.7 the pressure inside the chamber is

$$P = \frac{4}{3}\mu\frac{\delta V}{V} \tag{2.2.11}$$

so the moment tensor becomes

$$M = \frac{3}{2}\frac{1-\nu}{1-2\nu}VP \begin{pmatrix} 1 & 0 & 0 \\ 0 & 1 & 0 \\ 0 & 0 & 1 \end{pmatrix} \tag{2.2.12}$$

### 2.2.3 Tensile fault

*Okada (1985)*, gives the solution for the surface deformation due to shear and tensile faults in an half space. Firstly, for an isotropic media, the *i*th component of the displacement at $(x_1, x_2, x_3)$, due to a *j*th direction point force F at dislocation $\triangle u_j(\xi_1, \xi_2, \xi_3)$ across a surface $\Sigma$ at the depth $d$, is found

$$u_i = \frac{1}{F}\int\int_{\Sigma} \triangle u_j \left[\lambda\,\delta_{ik}\frac{\partial u_i^n}{\partial \xi_n} + \mu\left(\frac{\partial u_i^j}{\partial \xi_k} + \frac{\partial u_i^k}{\partial \xi_j}\right)\right] v_k d\sum \tag{2.2.13}$$

where $v_k$is the direction cosine of the normal to the surface element $d\Sigma$. In figure 2.6 the elastic medium occupies the region $z \leqq 0$ and x-axis is parallel to the strike direction of the fault. The slip vector $U = [U_1, U_2, U_3]$ represents the movement of the hanging wall with respect to the foot wall signed such that positive $U_1$ is left-lateral strike slip, positive $U_2$ is thrusting dip slip, and $U_3$ is tensile slip. Having the contribution from surface element $\triangle\Sigma$ , by integration it is possible to obtain the deformation fields for a finite rectangular fault with length L and width W. In this thesis a *rectangular uniform-opening tensile fault* is tested, whom displacements are given from

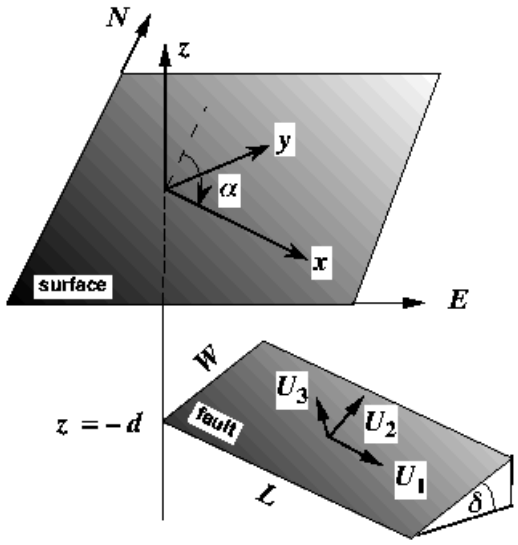


Figure 2.6: Schematic rapresentation of model fault source at depth d, with length L and width W, $\delta$ is the dip angle. Figure from http://earth.esa.int/ applications/data_util/ndis/equake/land4.htm

$$\begin{cases} u_x = \frac{U_3}{2\pi} & \left[\frac{q^2}{R(R+\eta)} - I_3 sin^2\delta\right] \\ u_y = \frac{U_3}{2\pi} & \left[\frac{-\widetilde{d}q}{R(R+\xi)} - sin\delta\left\{\frac{\xi q}{R(R+\eta)} - tan^{-1}\frac{\xi\eta}{qR}\right\} - I_1 sin^2\delta\right] \\ u_z = \frac{U_3}{2\pi} & \left[\frac{\widetilde{y}q}{R(R+\xi)} + cos\delta\left\{\frac{\xi q}{R(R+\eta)} - tan^{-1}\frac{\xi\eta}{qR}\right\} - I_5 sin^2\delta\right] \end{cases}$$

where

$$\begin{cases} I_1 = \frac{\mu}{\lambda+\mu} & \left[\frac{-1}{cos\delta}\frac{\xi}{R+\widetilde{d}}\right] - \frac{sin\delta}{cos\delta} I_5 \\ I_2 = \frac{\mu}{\lambda+\mu} & [-ln(R+\eta)] - I_3 \\ I_3 = \frac{\mu}{\lambda+\mu} & \left[\frac{1}{cos\delta}\frac{\widetilde{y}}{R+\widetilde{d}} - ln(R+\eta)\right] + \frac{sin\delta}{cos\delta} I_4 \\ I_4 = \frac{\mu}{\lambda+\mu}\frac{1}{cos\delta} & \left[ln(R+\widetilde{d}) - sin\delta ln(R+\eta)\right] \\ I_5 = \frac{\mu}{\lambda+\mu}\frac{2}{cos\delta} & tan^{-1}\frac{\eta(X+qcos\delta)+X(R+X)sin\delta}{\xi(R+X)cos\delta} \end{cases}$$

The rectangular uniform-opening tensile fault used in this thesis has 8 free parameters: horizontal projection (x, y), depth, volume change, fault length, fault width, azimuth and dip. For this source, volume change ($\Delta V$) is computed through the product of the fault area and opening (i. e. potency).

### 2.2.4 Finite ellipsoidal cavities

Most of volcano deformations are very different to those produced from a Mogi source, so other volcano sources, with different shapes, are introduced. The vertical displacements, at the earth's surface, are very similar for all models, if the source's depth is scaled appropriately; this is very important because suggests that it is difficult to determine the source shape with vertical displacement data alone; in this sense, the role of horizontal displacements becomes crucial.

An obvious extension of the spherical cavity, would be to a general three-dimensional ellipsoidal cavity subjected to uniform internal pressure because the general ellipsoid is versatile to cover a variety of particular cases. *Eshelby (1957)* was the first to propose an approximate solution for an ellipsoidal inclusion in an infinite elastic medium.

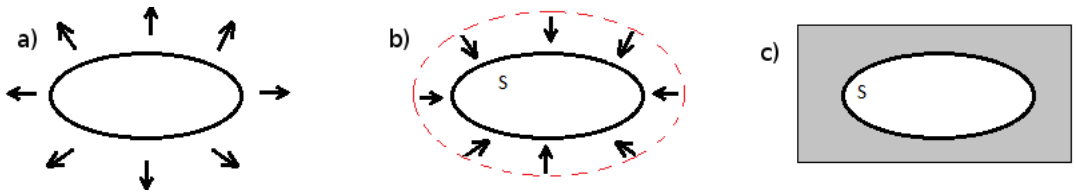


Figure 2.7: cut-and-weld procedure

Consider a cavity (or inclusion) in an infinite homogeneous isotropic elastic medium in which is valid the Hooke's law. It is possible to determine the perturbation on the elastic field due to a change of internal pressure of the source, to do this Eshelby proposed a cut-and-weld procedure. The region of the inclusion is "cut" from the matrix, so an un-constrained transformation takes place (see Figure 2.7(a)), $\varepsilon_{ij}^T$ is this stress free "transformation" strain. From the Hooke's law the stress is

$$p_{ij}^T = \lambda \varepsilon^T \delta_{ij} + 2\mu \varepsilon_{ij}^T \tag{2.2.14}$$

where $\varepsilon^T = \sum \varepsilon_{kk}$, note that at this stage, the stress in both the inclusion and the matrix is zero. Let be $S$ the surface separating matrix and inclusion and $n_i$ its outward normal. The second step is to apply tractions to the boundary of the inclusion such that it is elastically deformed back to its initial size and shape (see Figure 2.7(b)). The surface tractions are $-p_{ij}^T n_j$. At this point the inclusion is putted back in the matrix, this step is equivalent to

adding a layer of point forces to the surface $S$ that are equal and opposite to the traction $p_{ij}^T$(see Figure 2.7(c)). At this stage, the matrix remains stress free, the total strain in the inclusion (the sum of inelastic transformation strain and elastic strain) is zero. The induced strain in both the inclusion and matrix is $e_{ij}^C$ and

$$p_{ij}^C = \lambda \varepsilon^C \delta_{ij} + 2\mu \varepsilon_{ij}^C \tag{2.2.15}$$

So the stress due to the inclusion inside the matrix is

$$p_{ij}^I = p_{ij}^C - p_{ij}^T \tag{2.2.16}$$

where

$p_{ij}^I$ = is the stress due to the inclusion.

$p_{ij}^C$ = is the stress due to the inclusion and matrix.

$p_{ij}^T$ = is the stress due to the free transformation.

Since the displacement field in the $i$ direction at **r** due to a point-force $F_i$ at **r'** in a semi-infinite medium is

$$U_i(\mathbf{r}-\mathbf{r}') = \frac{1}{4\pi\mu}\frac{F_j}{|\mathbf{r}-\mathbf{r}'|} - \frac{F_i}{16\pi\mu(1-\sigma)}\frac{\partial^2 |\mathbf{r}-\mathbf{r}'|}{\partial x_i \partial x_j} \tag{2.2.17}$$

where $\sigma = \lambda/(\lambda+\mu)$ is the Poisson's ratio, the induced displacements in both the inclusion and matrix are given by

$$u_i^C(\mathbf{r}) = \int_s dS_k p_{jk}^T U_j(\mathbf{r}-\mathbf{r}') \tag{2.2.18}$$

Note that it is express in terms of relative coordinates because the hypothesis of infinite space. The strain is given by the spatial derivatives of $u_i^C$.

$$\varepsilon_{ij}^C = \frac{1}{2}\left(\frac{\partial u_i^C}{\partial x_j} - \frac{\partial u_j^C}{\partial x_i}\right) \tag{2.2.19}$$

while using equation 2.2.20 the stress in the matrix is

$$p_{ij}^{I} = p_{ij}^{C} - p_{ij}^{T} = \lambda(\varepsilon^{C} - \varepsilon^{T})\delta_{ij} + 2\mu(\varepsilon_{ij}^{C} - \varepsilon_{ij}^{T}) \tag{2.2.20}$$

Using Gausses's theorem $\int_S \mathbf{A} dS = \int_V \nabla \mathbf{A} dV$, in this case the derivative of a point force $U_j(\mathbf{r} - \mathbf{r}')$ becomes the difference of point forces in semi-infinite media

$$u_i^C(\mathbf{r}) = \int dV p_{jk}^T U_{j,k}^i(\mathbf{r} - \mathbf{r}') \tag{2.2.21}$$

where the $U_{j,k}(\mathbf{r} - \mathbf{r}')$ is the Green's function to describe a pair of opposing forces at position $\mathbf{r}$ pointing in the $j$ direction, separated in the $k$ direction. In far field we take everything except dV outside the integral and obtain

$$u_i(\mathbf{r}) = V p_{jk}^T U_{j,k}^i(\mathbf{r} - \mathbf{r}') \tag{2.2.22}$$

this requires 27 expressions, however using the symmetry of the stress tensor, off diagonal components are

$$W_{jk}^i = U_{j,k}^i + U_{k,j}^i \tag{2.2.23}$$

For a semi-infinite medium ($x_3' \leq 0$), equation 2.2.21 is a useful approximation provided that $U_{ij,k}(\mathbf{r} - \mathbf{r}')$ are computed for an half-space, in which case the Green's function does not depend on the difference $x_3' - x_3$, and the ellipsoid size is small with respect to its depth *(Davis, 1986)*. This solution satisfies boundary conditions exactly on the free surface but approximately on the ellipsoid, and it is accurate only if ellipsoid's dimension is twice time less of its depth. From Eshelby, it is known that for an ellipsoidal source region, in an infinite elastic medium, a constant $P_{jk}^T$ applied to the surface on the inclusion gives constant stresses and strains; in this sense the internal strain due to the convolution of the surface forces can be written as a linear combination of all the $\varepsilon_{kl}^T$

$$\varepsilon_{ij}^C = S_{ijkl}\varepsilon_{kl}^T \tag{2.2.24}$$

where $S_{ijkl}$ is the Eshelby's tensor and depends only from the axes lengths, its components are written by elliptic integrals of the second kinds. The stress due to the inclusion inside

the matrix is

$$p_{ij}^{I} = -\delta_{ij} P \tag{2.2.25}$$

this equation is used to choose the values of $e_{ij}^{T}$ from the pressure in the cavity

$$p_{ij}^{I} = p_{ij}^{C} - p_{ij}^{T} = -\delta_{ij} P \rightarrow \varepsilon_{ij}^{C} - \varepsilon_{ij}^{T} = S_{ijkl}\varepsilon_{kl}^{T} - \varepsilon_{ij}^{T} = \varepsilon\delta_{ij}/3 \tag{2.2.26}$$

which corresponds to the linear system:

$$\begin{bmatrix} S_{1111}-1 & S_{1122} & S_{1133} \\ S_{2211} & S_{2222}-1 & S_{2233} \\ S_{3311} & S_{3322} & S_{3333}-1 \end{bmatrix} \begin{bmatrix} \varepsilon_{11}^{T} \\ \varepsilon_{22}^{T} \\ \varepsilon_{33}^{T} \end{bmatrix} = \frac{1}{3} \begin{bmatrix} \varepsilon \\ \varepsilon \\ \varepsilon \end{bmatrix} \tag{2.2.27}$$

where $e$ is the expansion stress inside the matrix that corresponds to the pressure $P$, infact $P = K\varepsilon$, where K is the Bulk modulus of the matrix. $p_{ij}^{I}$ values are obtained from eq. 2.2.20 having the values $\varepsilon_{ij}^{T}$ .

$$-3P = P_{kk}^{I} = 2\mu(\varepsilon^{C} - \varepsilon^{T}) + 3\lambda(\varepsilon^{C} - \varepsilon^{T}) = 3K(\varepsilon^{C} - \varepsilon^{T}) \tag{2.2.28}$$

but remembering that $K = \lambda + 2\mu/3$

$$P_{kk}^{I} = 3K(\varepsilon^{C} - \varepsilon^{T}) \tag{2.2.29}$$

so

$$\varepsilon^{C} - \varepsilon^{T} = \varepsilon \tag{2.2.30}$$

and

$$2\mu(\varepsilon_{ij}^{C} - \varepsilon_{ij}^{T}) + \lambda\delta_{ij}\varepsilon = K\delta_{ij}\varepsilon \tag{2.2.31}$$

To solve the problem of a pressurized triaxial ellipsoidal cavity in an infinite medium, Eshelby used uniform distribution of doubles forces and centers of dilatation, within the ellipsoid, to produce normal uniform stresses on its surface. By a volume integration of the force distributions, external displacements are found. To reduce the difficulty of integration, *Yang et al., (1988)* simplified the volume integral to a line integral by finding

the distributions of double forces and centers of dilatation between the spheroid foci which satisfy the constant pressure boundary condition on its surface. The double forces are aligned along the spheroid axis. For example, for a vertical prolate ellipsoid, the vertical double forces are compressive such that the force couples in the horizontal direction are greatest. This makes sense in that the force couples in the vertical surface area, giving rise to a greater horizontal force. For an oblate ellipsoid, the double forces are tensile, so the vertical force couples are maximal (see figure 2.8).

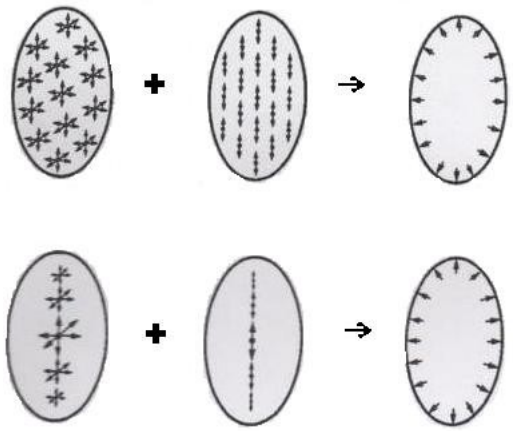

Figure 2.8: Models of equivalent sources distribution for a prolate spheroid for *Eshelby* (1957) (top) and *Yang et al. (1988)* (bottom)

At this point is important to focus on the volume change of the chamber. Results for a generic ellipsoid cavity are given by *Amoruso and Crescentini (2009)* ; since the total strain in the inclusion is equal to the constraint strain, the change in volume is given by

$$\delta V = \varepsilon^C_{kk} V \tag{2.2.32}$$

Using the equation 2.2.26 the

$$\begin{aligned} -3P &= 3K(\varepsilon^C - \varepsilon^T) \rightarrow -3P = 3K(\varepsilon^C - \frac{p^T}{3K}) \\ -3P &= 3K\varepsilon^C - p^T \rightarrow \varepsilon^C = \frac{-3P + p^T}{3K} \end{aligned} \tag{2.2.33}$$

so

$$\delta V = V\left(\frac{-3P+p^T}{3K}\right) = \frac{VP}{3K}\left(\frac{p^T}{P}-3\right) \tag{2.2.34}$$

*Davis (1986)* found that an extended ellipsoidal source is equal to a distribution of moment tensors equal to each other with auto vectors oriented as ellipsoid axes (a,b,c). The single moment tensor is

$$M_{single} = P\begin{pmatrix} P_a^T/P & 0 & 0 \\ 0 & P_b^T/P & 0 \\ 0 & 0 & P_c^T/P \end{pmatrix} \tag{2.2.35}$$

The $P_i^T/P$ ratios are functions of the ellipsoid axis ratio and consequently depend from its shape and $P$ is positive for overpressure. Note that $p^T = P_{11}^T + P_{22}^T + P_{33}^T$ is independent from ellipsoid axes orientation and it is proportional to the seismic moment trace. The volume integral gives the $M_{tot}$

$$M_{tot} = VP\begin{pmatrix} P_a^T/P & 0 & 0 \\ 0 & P_b^T/P & 0 \\ 0 & 0 & P_c^T/P \end{pmatrix} \tag{2.2.36}$$

Using eq. 2.2.34 $M_{tot}$ becomes

$$M_{tot} = \frac{3K\delta V}{\left(\frac{p^T}{P}-3\right)}\begin{pmatrix} P_a^T/P & 0 & 0 \\ 0 & P_b^T/P & 0 \\ 0 & 0 & P_c^T/P \end{pmatrix} \tag{2.2.37}$$

so it is possible to write the moment tensor equivalently by the product between PV (or $\delta V$) with a term that depends only from the shape. Note that for a sphere ($a=b=c$); $P_a^T = P_b^T = P_c^T = 3P((1-\nu)/2(1-2\nu))$ that is the same previously result.

*Fialko et al. (2001)* solved the problem of computing deformation due to a finite horizontal crack embedded in a homogeneous half-space, in figure 2.9 there is a schematically view of an horizontal penny-shaped crack with radius R and depth H in an elastic half-space. In this analysis the half-space surface is assumed to be stress-free and the crack plane divides the half-space into two domains (i=1, 2, in figure 2.9). To solve this problem *Fialko et*

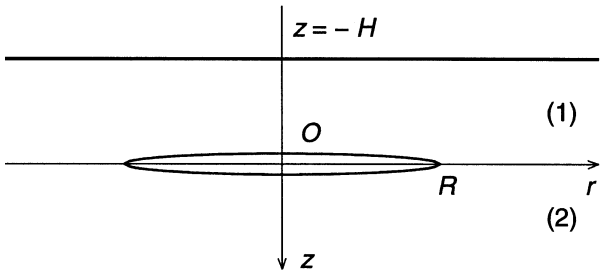


Figure 2.9: Horizontal circular crack in a semi-infinite elastic body (Figure from *Fialko et al., 2001*)

*al. (2001)* used a procedure to relate the stress and displacement to Neuber-Papkovich functions. In this case the boundary conditions are

for $z = -h$

$$\sigma_{zz}^{(1)} = \sigma_{rz}^{(1)} = 0 \quad \text{for } 0 \leq r < \infty$$

for $z = 0$

$$\sigma_{zz}^{(1)} = \sigma_{zz}^{(2)} = -\triangle p(r),$$

$$\sigma_{rz}^{(1)} = \sigma_{rz}^{(2)} = \tau(r) \quad \text{for } 0 \leq r < 1,$$

$$U_z^{(1)} = U_z^{(2)} \, , U_r^{(1)} = U_r^{(2)} \quad \text{for } 1 \leq r < \infty$$

where $\triangle p(r) = p_M - p_L$ where $p_M =$ is the magma pressure and $p_L =$lithostatic pressure. $\tau(r)$ is the shear stress at the crack walls, and is assumed that the stress distribution is the same in the top and bottom crack faces. The goal of *Fialko et al.* was to find the Neuber-Papkovich functions that satisfy the governing equations of the theory of elasticity and the boundary conditions. No solution is available for an horizontally layered elastic medium, but a point crack is a good approximation of a finite crack if source depth to radius exceeds 5 *(Crescentini and Amoruso, 2007)*. The approximation begins to break for H/R = 2.5 and is poor for H/R=1 (*Segall, 2010*). Following *Amoruso et al., (2007) and Amoruso et al.,*

*(2008)*, this source is schematized through an even distribution of moment tensors

$$M_i = m\left[1-\left(\frac{r_i}{R}\right)^4\right]\frac{2\mu}{1-2\nu}\begin{pmatrix}\nu & 0 & 0\\ 0 & \nu & 0\\ 0 & 0 & 1-\nu\end{pmatrix}$$

over the crack mid-plane (perpendicular to the z-axis). Here $r_i$ is distance of the i-th moment tensor from the crack axis, $R$ the crack radius, $\mu$ rigidity, and $\nu$ the Poisson's ratio. $M_i$ is the moment tensor of a small (point-like) crack whose potency (area times opening, i. e. volume change $\Delta V_i$ ) is

$$\triangle V_i = m\left[1-\left(\frac{r_i}{R}\right)^4\right] \tag{2.2.38}$$

Volume change $\Delta$V of the crack is

$$\triangle V = \sum_i \triangle V_i = m\sum_i\left[1-\left(\frac{r_i}{R}\right)^4\right] \tag{2.2.39}$$

#### 2.2.4.1 Approximate solutions for stress and displacements due to a pressurized ellipsoidal cavity in an elastic half-space

*Amoruso and Crescentini (2011)* proposed an approximate solution for stresses and displacements due to a pressurized ellipsoidal cavity in an elastic half-space. It is considered a generic triaxial ellipsoid with semi-axes $a_1 \geq a_2 \geq a_3$ and oriented by Euler angles $\alpha, \beta, \gamma$ and center in $(x_0, y_0, z_0)$. If $G(r-r'_s, z)$ is the Green's function of the ellipsoid with $PV = 1$ located in $(\mathbf{r}, z) = (x, y, z)$ in a point-station in $(\mathbf{r_s}, 0) = (x_s, y_s, 0)$ the effect of this source is

$$v = P\int\int\int_v G(\mathbf{r}-\mathbf{r_s}, z)dV \tag{2.2.40}$$

using second order Taylor expansion of $G(\mathbf{r}-\mathbf{r_s}, z)$ around the ellipsoid center $(x_0, y_0, z_0)$

$$G(\vec{r}-\vec{r}_s,z) \simeq G(\vec{r}_0-\vec{r}_s,z)+(x_i-x_{0i})\left(\frac{\partial G(\vec{r}-\vec{r}_s,z)}{\partial x_i}\right)_{(\vec{r},z)=(\vec{r}_0,z_0)} \quad (2.2.41)$$

$$+\frac{1}{2}(x_i-x_{oi})(x_j-x_{0j})\left(\frac{\partial G(\vec{r}-\vec{r}_s,z)}{\partial x_i \partial x_j}\right)_{(\vec{r},z)=(\vec{r}_0,z_0)} \quad (2.2.42)$$

so replacing in the eq.2.2.40

$$v = PVG(\vec{r}_0-\vec{r}_s,z)+\frac{1}{2}PQ_{ij}\left(\frac{\partial^2 G(\vec{r}-\vec{r}_s,z)}{\partial x_i \partial x_j}\right)_{(\vec{r},z)=(\vec{r}_0,z_0)} \quad (2.2.43)$$

where

$$Q_{ij} = \int\int\int (x_i-x_{0i})(x_j-x_{0j})dV \quad (2.2.44)$$

The second term of eq. 2.2.41 $\int\int\int_v (x_i-x_{0i})dV = 0$.
Using the equation 2.2.22 and expanding $U_{j,k}(x'_1-x_1,x'_2-x_2,x'_3,x_3)$ around the ellipsoid center $\mathbf{r}^0=(x_0,y_0,z_0)$

$$u_i(\mathbf{r}') \simeq P^T_{jk}U^i_{j,k}(x'_1-x^0_1,x'_2-x^0_2,x'_3,x^0_3)V+\frac{1}{2}P^T_{jk}Q_{lm}(\frac{\partial^2 U^i_{j,k}(x'_1-x_1,x'_2-x_2,x'_3,x_3)}{\partial x_l \partial x_m})_{\mathbf{r}=\mathbf{r_0}}. \quad (2.2.45)$$

The basic idea of this approach is the multipole expansion of the electric field; in electromagnetism this expansion allows to approximate, at large distances, the electric potential generated by a system of electric charges. This procedure is, however, impossible when the distribution extends to infinity, as in case of an infinite charged plane. The peculiarity of this development is that the terms that appear are formally identical to those of simple spatial configurations, and therefore can be decomposed into the sum of the potential due to a single charge (monopole), a dipole, a quadrupole, and so on. The term $Q_{lm}$ is similar to usual quadrupole moment, but cannot made traceless because generally the function $P^T_{jk}U^i_{j,k}(x'_1-x^0_1,x'_2-x^0_2,x'_3,x^0_3)$ does not satisfy the Laplace's equation with respect to $(x_1,x_2,x_3)$. If $Q_{lm}$ is isotropic, the Laplace's equation is satisfied, so the quadrupole term is null. Using the Euler angles and following the convention of Z-X-Z

co-moving axes rotations, for moving the (x, y, z) reference frame (e. g. x Northward, y Eastward, z downward) to the (X, Y, Z) referred frame (X parallel to the shortest ellipsoid axis or the minimum moment tensor eigenvector, Y to the intermediate ellipsoid axis or moment tensor eigenvector, Z to the longest ellipsoid axis or the maximum moment tensor eigenvector), $Q$ can be write as

$$Q = \frac{V}{5}\begin{pmatrix} a_3^2 & 0 & 0 \\ 0 & a_2^2 & 0 \\ 0 & 0 & a_1^2 \end{pmatrix} \tag{2.2.46}$$

where V is the ellipsoid volume.
In an heterogeneous half-space, the Green's function cannot be written exactly, but in a coordinate system (X,Y,Z) coincident with the ellipsoid axes the eq. 2.2.40 can be re-written as

$$v \simeq PVG(-\vec{r}_s) + \frac{1}{2}PQ_{ij}\left(\frac{\partial^2 G(\vec{r}-\vec{r}_s)}{\partial x_i \partial x_j}\right)_{\vec{r}=0} \tag{2.2.47}$$

$$\simeq PVG(-\vec{r}_s)+$$

$$+\frac{1}{2}PV\left[\frac{a_1^2}{5}\left(\frac{\partial^2 G(\vec{r}-\vec{r}_s)}{\partial x_i \partial x_j}\right)_{\vec{r}=0} + \frac{a_2^2}{5}\left(\frac{\partial^2 G(\vec{r}-\vec{r}_s)}{\partial x_i \partial x_j}\right)_{\vec{r}=0} + \frac{a_3^2}{5}\left(\frac{\partial^2 G(\vec{r}-\vec{r}_s)}{\partial x_i \partial x_j}\right)_{\vec{r}=0}\right]$$

The "monopole" term gives the same displacement field as the moment tensor co-located with the ellipsoid center.

$$M_0 = VP\begin{pmatrix} P_a^T/P & 0 & 0 \\ 0 & P_b^T/P & 0 \\ 0 & 0 & P_c^T/P \end{pmatrix} \tag{2.2.48}$$

Generally the $P_a^T/P, P_b^T/P, P_c^T/P$ can be obtained through first and second types elliptic integrals. To determine $\partial^2 G(\vec{r}-\vec{r}_s,z)/\partial x_i \partial x$ it is necessary to make a second order Taylor's expansion. Using the definition of derivative

$$\frac{\partial^2 f(x)}{\partial x^2} = \lim_{\varepsilon\to 0}\frac{\frac{f(x+\varepsilon)-f(x)}{\varepsilon} - \frac{f(x)-f(x-\varepsilon)}{\varepsilon}}{\varepsilon} = \tag{2.2.49}$$

$$\lim_{\varepsilon\to 0}\frac{f(x+\varepsilon)-f(x)-f(x)-f(x-\varepsilon)}{\varepsilon^2} = \tag{2.2.50}$$

$$\lim_{\varepsilon\to 0}\frac{f(x+\varepsilon)-2f(x)-f(x-\varepsilon)}{\varepsilon^2} \tag{2.2.51}$$

and the term $\frac{a_1^2}{5}\left(\frac{\partial^2 G(\vec{r}-\vec{r}_s)}{\partial x_i \partial x_j}\right)_{\vec{r}=0}$ becomes

$$\frac{a_1^2}{5}\left(\frac{\partial^2 G(\vec{r}-\vec{r}_s)}{\partial x_i \partial x_j}\right)_{\vec{r}=0} \simeq G\left(\left(0,0,\frac{a_1}{\sqrt{5}}\right)-\vec{r}_s\right)+G\left(\left(0,0,-\frac{a_1}{\sqrt{5}}\right)-\vec{r}_s\right)- \tag{2.2.52}$$

$$-2G((0,0,0)-\vec{r}_s)$$

and the equation 2.2.47 becomes

$$v \simeq PVG(-\vec{r}_s)+ \tag{2.2.53}$$

$$+\frac{1}{2}P\left[G\left(\left(0,0,\frac{a_1}{\sqrt{5}}\right)-\vec{r}_s\right)+G\left(\left(0,0,-\frac{a_1}{\sqrt{5}}\right)-\vec{r}_s\right)+G\left(\left(0,-\frac{a_2}{\sqrt{5}},0\right)-\vec{r}_s\right)+\right.$$

$$\left.+G\left(\left(0,-\frac{a_2}{\sqrt{5}},0\right)-\vec{r}_s\right)+G\left(\left(-\frac{a_3}{\sqrt{5}},0,0\right)-\vec{r}_s\right)+G\left(\left(-\frac{a_3}{\sqrt{5}},0,0\right)-\vec{r}_s\right)\right]-$$

$$2PVG(-\vec{r}_s) \tag{2.2.54}$$

The monopole term is equivalent to a moment tensor centered in the origin with intensity $PV$; the quadrupole is equivalent to six point sources distributed along the ellipsoid with weight $1/2$ and one point source located at the ellipsoid center, with weight -3. So the explicit solutions, that can be implemented also for an heterogeneous media, involves the use of seven point sources, one point source is located at the ellipsoid center, with weight -2; six half-potency (and opposite in sign) sources are symmetrically distributed

along the ellipsoid axes placed at $a/\sqrt{5}$ from the ellipsoid center, as shown in figure 2.10 In this thesis, a pressurized finite spheroidal cavity having a vertical axis of symmetry

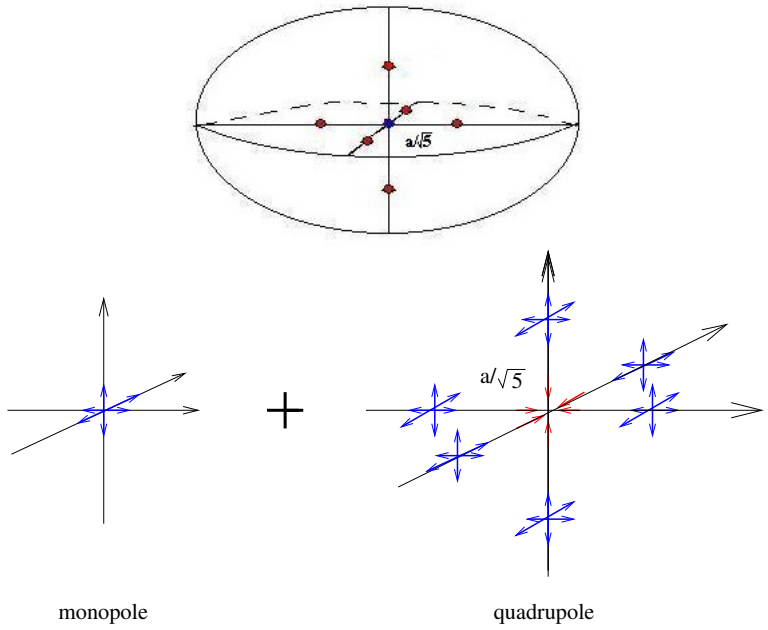


Figure 2.10: Schematic modeling of the seven sources approximation

and a pressurized finite triaxial ellipsoidal cavity are mathematically modeled using the quadrupole approximation (*Amoruso and Crescentini, 2011*).

# Chapter 3

# Monte Carlo inversion of deformation data

## 3.1 Monte Carlo inversion methods and misfit function

In geophysics, it is often necessary to estimate model parameters from collected data, in order to obtain the most likely values of the model parameters that describe completely the system; here the term "model" indicates a kind of source (pressurized sphere, moment tensor, etc.). Disagreement (misfit) between a given model and observations is measured using misfit functions usually obtained from the likelihood function, whose form depends on the assumed statistical distribution of residuals (differences between model prediction and data). Model parameters optimization is obtained by minimizing the misfit function. Optimization problems can be classified into two types; linear inversions, when one minimum, of the misfit function, is present and the solution may be obtained by solving a set of linear equations and non linear inversion when there are many minima. In this last case a nonlinear inversion is performed in order to find a global minimum among many local ones (see figure 3.1). Often, Monte Carlo methods (MC) are used to analyze nonlinear inverse problems where the relation between data and model parameters have not an analytical expression, and where linearization is unsuccessful. This method, introduced firstly from Nicholas Metropolis, owes its name to the Monte Carlo casino, the ideal place for random events; infact Monte Carlo methods are numerical processes that produce so-called pseudo-random numbers, a series of numbers that appear random if tested with any

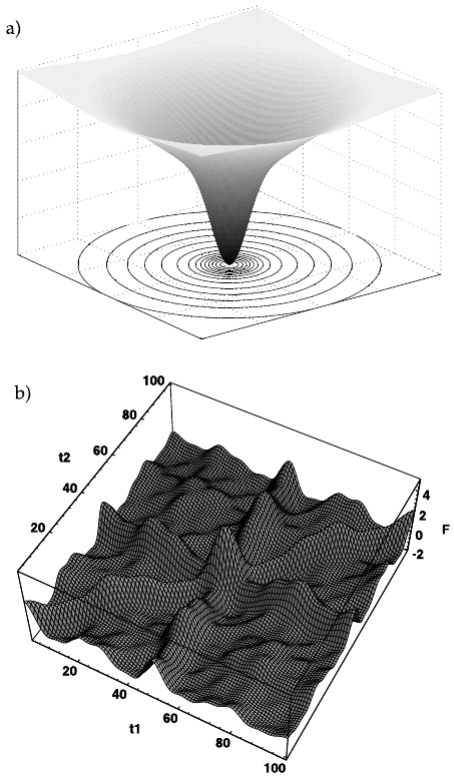


Figure 3.1: a) Example of a misfit function in case of a linear problem in which the misfit function is quadratic in the parameters and presents an absolute minimum b) Example of misfit function in case of a nonlinear problem in which there is the presence of several local minima ( Figure from *Sanbridge and Mosegaard, 2002*)

reasonable statistical test.

In case of linear problems, least squares fit (minimization of squared residuals) is a common choice because it is mathematically simple and the misfit function has one global minimum. However, least squares fit assumes a gaussian distribution of residuals and makes retrieved parameters sensitive to the presence of outliers. Ground displacements depend linearly on source potency but nonlinearly on the remaining parameters (e.g. source center location); even a least squares fit is consequently nonlinear if all the parameters are left adjustable in the inversion procedure. In this thesis the absolute deviation of residuals ($\mathscr{L}^1$ -norm misfit function) is minimized, appropriate for two-sided-exponentially distributed residuals and commonly used for robust fitting *(Amoruso et al., 2002, Amoruso et al., 2005)*:

$$\mathscr{L}^1 = \sum_{i=1}^{N_j} \left| \frac{x_i - f_i(a)}{\sigma_i} \right| \tag{3.1.1}$$

$x_i (i = 1, ..., N_j)$ indicates independent data, $f_i(a)$ is model prediction of $x_i$ given model parameters **a**, and $\sigma_i$ is uncertainty of $x_i$. From the maximum likelihood point of view, all the weights $w_j$ should be 1 independently of how many data are in each data set, provided that uncertainties have been estimated correctly.

There are many algorithms based on MC methods and a useful framework for comparing different searches is in terms of a trade-off between exploration and exploitation. Exploration improves the objective function searching (randomly) on the parameters space, without using information obtained from previous sampling. Exploitation is the opposite; the algorithm decides where sampling the parameter space only using the previous sampling and sometimes just the current best fit model *(Sanbridge and Mosegaard, 2002)*. Only simulated annealing and neighborhood algorithm are used in this thesis and are illustrated in the next sections. Figure 3.2 shows as this technique are a good compromise

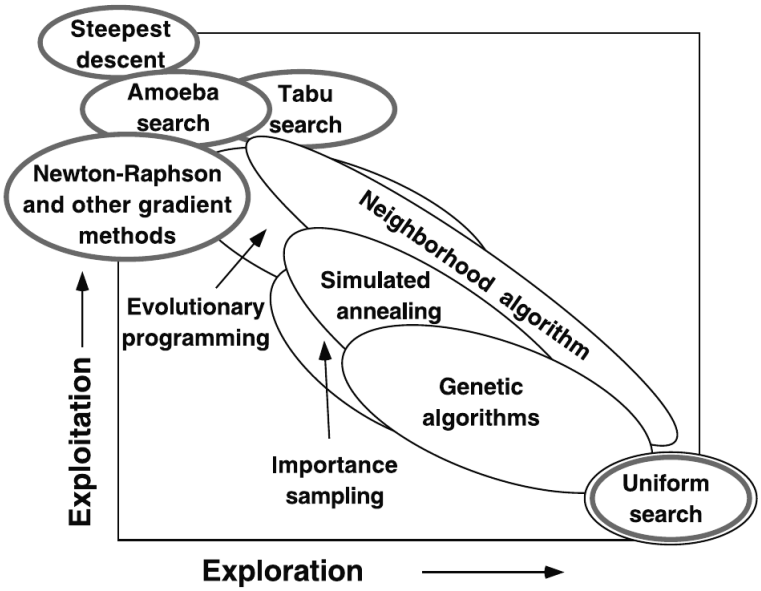


Figure 3.2: Optimization algorithms show in terms of trade-off between exploration and exploitation. Shaded borders indicate a deterministic (non–Monte Carlo) method. (Figure from *Sanbridge and Mosegaard, 2002*).

between exploration and exploitation.

### 3.1.1 Adapted Simulated Annealing (ASA)

In this thesis, misfit function optimization is obtained, firstly, using Adaptive Simulating Annealing *(Ingber, 1993)*. Adaptive Simulating Annealing (ASA) is a variant of simulated annealing (SA) algorithm. The work of *Rothman (1985, 1986)* introduced into geophysics the technique of simulated annealing, which is a nonuniform Monte Carlo method for global optimization. Simulated annealing owes its name and inspiration from annealing in metallurgy, infact the way in which crystals grow depends from the cooling rate of melt; this rate is important because a non-crystaline, metastable glass can form if cooling is too rapid. This crystal is the state of minimum energy for this system, so for slowly cooled systems, nature is able to find this minimum energy state. Nature uses a minimization algorithm based on the so-called Boltzmann probability distribution

$$P(E) \sim e^{-\frac{E}{kT}} \tag{3.1.2}$$

that expresses the idea that a system in thermal equilibrium at temperature T has its energy probabilistically distributed among all different energy states E. The quantity $k$ (Boltzmann's constant) is a nature constant that relates temperature to energy. In the algorithm the misfit function is identified with the energy of the crystalline material and the goal is to bring the system, from an arbitrary initial state, to a state with minimum possible energy. By appropriate definition of a temperature parameter for simulations, it is possible to simulate a "cooling" of the system to be optimized. For each model parameters $X_{ij}$, a random perturbation is made, and the change in energy, $\triangle E$, is computed. If $\triangle E \leq 0$, the perturbation is accepted. If $\triangle E$ is positive then the perturbation is accepted with a probability

$$P(\triangle E) \sim e^{-\frac{\triangle E}{T}} \tag{3.1.3}$$

and it is possible to choose a number $\alpha$ uniformly distributed between 0 and 1. This, essentially, is the Boltzmann distribution contributing to the statistical mechanical partition function of the system. If $\alpha \leq P(\triangle E)$ the perturbation is accepted. If the new model is

rejected, a new perturbation, controlled by a temperature parameter $T$, is attempted in the next move. The temperature parameter serves to control the region of the parameters space explored by the algorithm; at high temperatures, the SA algorithm samples all the space of the parameters because solutions, far from minimum, are accepted. Subsequently, by lowering the value of the control parameter, the algorithm is confined in increasingly restricted regions of the parameters space. In other words, as the temperature gradually approaches zero, the probability that the system is close to the global minimum for its objective function approaches 1 (see figure 3.3).

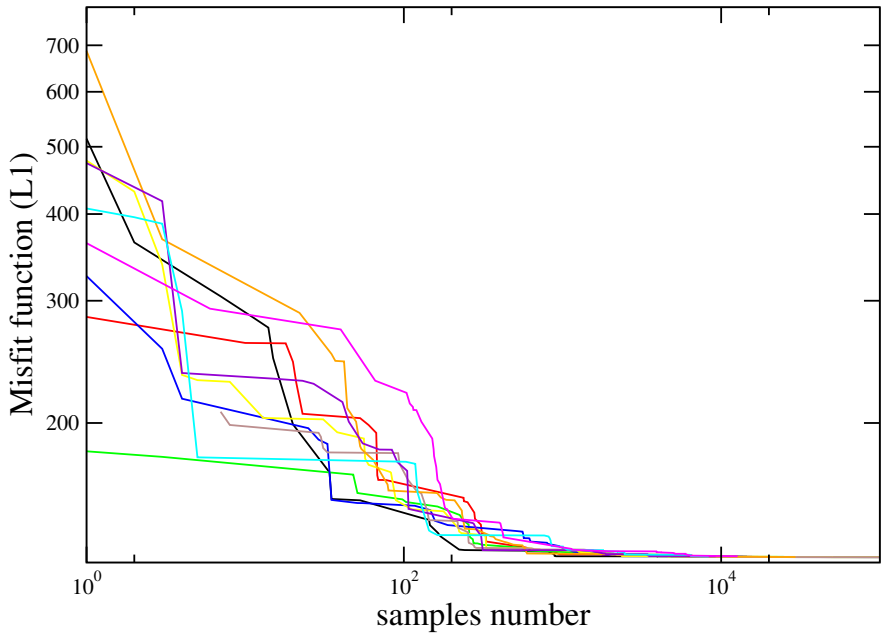


Figure 3.3: Examples of misfit function (L1) trends respect to samples numbers, even if the starting values of misfit are such different, after a samples number of$\sim 10^4$ , the misfit value become the same.

So, simulated annealing algorithm can be synthesized in four basic steps.

1. Definition of a probability density of state-space of parameters, where the parameterization is respect to the “temperature”

2. Definition of a probability for acceptance of new cost-function given the just previous value

3. Introduction of a schedule of "annealing" the "temperature" T in annealing-time steps

The acceptance probability is based on the chances of obtaining a new state with "energy" $E(k+1)$ relative to a previous state with "energy" $E(k)$ *(Ingber, 1995).*
In this thesis, a variant of SA called Adaptive Simulated Annealing (ASA) *(Ingber, 1993; Ingber, 1995),* is used. ASA aims to find the best global fit of a non-linear misfit function over a multidimensional parameters space, it ensure ample global searching in the first phases of search and ample quick convergence in the final phases, self-optimizing its program options recursively. The parameters space can be D-dimensional and different parameters have different finite ranges, fixed by physical considerations, and different annealing-time-dependent sensitivities, measured by the curvature of the cost-function at local minima. ASA try to consider possible differences in each parameter dimension, e.g., different sensitivities might require different annealing schedules. The temperature and the step size are adjusted, so that all of the search space is sampled to a coarse resolution in the early stages, while the state is directed to favorable areas in the late stages. This algorithm permits an annealing schedule for temperature T decreasing exponentially in annealing-time $k$.

$$T_i(k) = T_{0i} exp(-c_i k^{1/D}) \tag{3.1.4}$$

The introduction of re-annealing also permits adaptation to changing sensitivities in the multi-dimensional parameter-space.

### 3.1.2 The Neighborhood Algorithm (NA)

The Neighborhood Algorithm (NA) is an inversion technique very similar to simulated annealing, infact it uses a random sampling of parameters space and requires a cost function and a forward model to be specified. Compared to a basic Monte Carlo sampling, these approaches try to guide the random generation of samples by the results obtained so far on previous samples. The areas of the parameters space, where no interesting solution can be found are less sampled than promising areas.
For the neighborhood algorithm, as for simulated annealing, is firstly necessary defined a multidimensional parameters space and, by a direct search method, to find points (mod-

els) with acceptable values of misfit function. This algorithm uses same geometrical constructs, known as Voronoi cells, to model the misfit function across the parameters space; the first step is to generate, in the parameters space, a number of random models ($n_s$) with uniform probability, Voronoi cells are partitions of the parameters space and for every point (p) is associated a region V(p) that is the nearest neighbor region defined under a suitable distance norm (usually Euclidean). Note that the size (volume) of each cell is inversely proportional to the point's density.
New samples are then made in the union of a number ($n_r$) cells with a low misfit. Subsequently $n_s$ new models are generated by performing a uniform random walk (Gibbs sampler) in the Voronoi cell of each of the $n_r$ chosen models (i.e. $n_s/n_r$ samples in each cell). The process is repeated max times until an acceptable sampling of the solution is obtained (see figure 3.4). This algorithm has the advantage that size and shape are de-

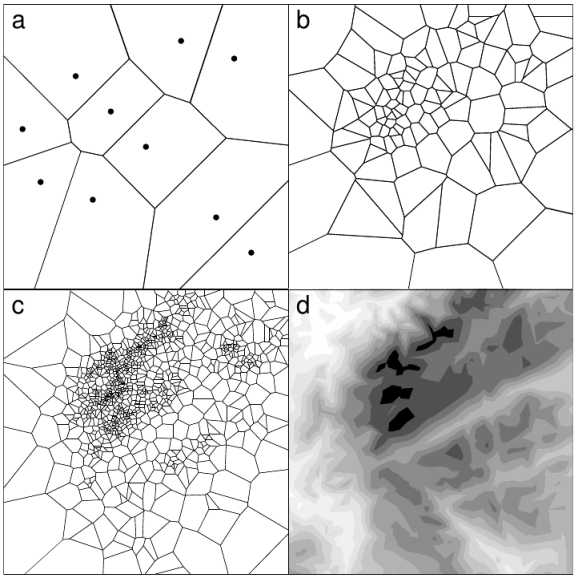


Figure 3.4: (a) 10 quasi uniform random points and their Voronoi cells. (b) The Voronoi cells about the first 100 samples generated by a Gibbs sampler using the neighbourhood approximation. (c) Similar to b) for 1000 samples. (d) Contours of the test objective function. (figure from *Sambridge, 1999a*)

termined automatically and uniquely by the first samples and are not chosen a priori and also the rank of models (how the misfit of a given model compares to the misfit of other models), rather than the value of the misfit itself, drives the search process. The choice of the two parameters $n_s$ and $n_r$ is very important, indeed increasing the number of resembled

Voronoi cells $n_r$ there are less possibility to find a local minimum and when $n_s$ increases, more weight is given to the previous samples because the Voronoi cells are updates less frequently (*Sambridge, 1999a).*
Like for any other Monte Carlo methods, success in finding the optimal model parameters is never guaranteed by ASA or NA, so we cross-check ASA and NA inversions to increase results confidence.

## 3.2 Marginal probability density function with NA-Bayes

The second stage consists of an algorithm for using the entire ensemble of models produced with NA, and deriving information from them in the form of Bayesian measures of resolution, trade-offs between parameter couples and Marginal Probability Density Functions (MPDF) *(Sambridge, 1999b)*, as in this thesis, in which assessment of parameter uncertainties is performed in the form of MPDF.
Bayesian inference is a method for combining prior information on a model with the information from new data; in this formulation of an inverse problem, all information is represented in probabilistic terms *(Sanbridge and Mosegaard, 2002*). Information that could be derived from the ensemble produced with NA are limited from two factors. The first is the degree of constraint provided by the observed data, and the second is how well are sampled the "important" region of parameter space. In this sense, the first quantity to introduce is the posterior probability density (PPD) that is the solution to the inversion problem by a Bayesian approach. This quantity is used to represent all information available for a model. If **m** is a point, in model space, the PPD is given by

$$P(m|d_0) = k\rho(m)L(m|d_0), \tag{3.2.1}$$

where $\rho(m)$ is the prior probability distribution, $L(m|d_0)$ is a likelihood function which represents the fit to observations ($d_0$), and $k$ is a normalizing constant. A property of PPD, that is used in this thesis, is the marginal PPD that is a a function of one or more variables and is formed from an integral of the PPD over the remaining dimensions of the

parameters space. For example, the marginal distribution of variable $m_j$, is given by

$$M(m_i) = \int \ldots \int P(m) \prod_{\substack{k \neq i \\ k=1}}^{d} \tag{3.2.2}$$

through these marginals is it possible to have information on a single, or pair of variables. Veronoi cells are used again for reconstruction of the PPD from a finite ensemble of samples. This is done by simply setting the known PPD of each model to be constant inside its Voronoi cell. $P_{NA}(m)$ is the name of the neighbourhood approximation to the PPD. So, starting from the neighbourhood approximation of the PPD, the Gibbs sampler is used to have the re sampled ensemble, that can generate a random walk in model space. The point B is the start point of random walks and it is the model from the input ansemble. From this point it takes a series of steps along each parameter axis in turn.Conditional probability $P_{NA}(m)$ is random deviate at each steps. Since $P_{NA}(m)$ is constant inside each Voronoi cell, than the conditional PDF is built from the PPD values inside each Voronoi cell intersected by the axis. Only when all dimensions have been cycled through once, and

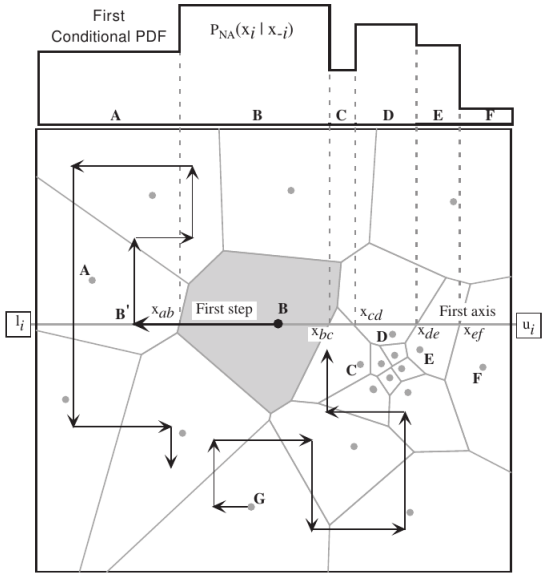


Figure 3.5: Two examples of Gibbs sample. The shape of the conditional, $P_{NA}(x_i|x_{-i})$ for the first step (x- direction) of the walk starting at cell B is shown above the figure. Another independent random walks starts from point G. (figure from *Sambridge, 1999b)*

a complete new model space vector has been generated the iteration is completed and another independent random walks starts from point G (see figure3.5) *(Sambridge, 1999b)*. After many steps the density distribution of the random walk will asymptotically tend to the approximate PPD, $P_{NA}(x)$. It is important that the number of walkers $n$ is sufficiently big, infact only after a number m, is it possible have a good solution, therefore the first m samples are eliminated and only (n - m) walks are used. At first m realizations of the Gibbs sampling, which are not used, usually refers as *burn-in*. Through NA-Bayes, 2-D marginals, are also calculated, and they are a valid way to show evident trade-offs that link two different parameters.

## 3.3 ANGELA: a package for the inversion of geodetic data

In this thesis, to invert the data by ASA and NA, the package ANGELA is used. ANGELA, acronym for Analysis of Geodetic data in Layered media (*Crescentini et al. 2007*), is a package for the inversion of geodetic data, for different types of sources embedded in a homogeneous or layered elastic elastic half-space. ANGELA is composed of more than 50 functions written in C and Fortran. The program is controlled by five files of ASCII input and can invert different types of data as leveling, dilatometric, EDM, GPS, gravity data, SAR and sea level changes, using different models (e. g. one or more double-couple sources, expansion sources, mass intrusions etc).

As input is necessary to provide:

- *asa_opt* file, in which there are the points number used by ASA to sample the parameters space and the range of variability of every single parameter.
- *inversione.cfg* file, in which there are information on the type of misfit function used (L1 or L2), on the source to use, and the names of input and output files. Also there is the possibility of using more than only one source.

In case of layered half-space, Green's functions which depend on layering details, are generated. The results are written in the output files, specifically in the file *parametri.out* there are the values of parameters related to ten different cooling for the ASA algorithm. A typical ANGELA session (also used in this thesis) consists of five steps:

1. generation of data files
2. generation of option files (misfit function, annealing parameters for ASA, etc.);
3. data inversion using ASA (to search for the mist global minimum);
4. parameters space sampling using NA;
5. 1D and 2D marginal PPD estimation using NAB.

As seen in chapter 2, model sources are represented as linear combination of four fundamental point sources, namely the strike-slip double-couple, the dip-slip double-couple, the compensated linear vertical dipole (CLVD) and the isotropic inflation. The vector *pmwei[]* in ANGELA provides the weights for this base. Parameters of the elastic layered medium are chosen a priori using seismic tomography and/or geological information, and proper Green's functions are generated as previously described and stored for future use. In case of mass-less sources, time-dependent Green's functions, of a given layered viscoelastic-gravitational half-space for the four fundamental dislocation sources at different depths, are computed using PSGRN *(Wang et al., 2006)*.

## 3.4 Akaike information criterion

Generally, data are explained assuming a model. In principle, any set of data can be almost perfectly fitted by using a sufficiently complicated model, so to discriminate among competing models, we must account for both the misfit and the number of model parameters. The preferred model is the simplest one that fits the data within the expected errors (parsimony principle). We can choose the "best model", among a set of different types of models, using the Akaike's Information Criterion. Perhaps none of the models in the set are good, but AIC attempts to select the best approximating model of those in the candidate set. Thus, every effort must be made to assure that the set of models is well founded. *Akaike (1973)* found a simple relationship between expected Kullback-Leibler information and Fisher's maximized log-likelihood function.
The Kullback-Leibler (K-L) method finds the "distance" between two models, $f$ and $g$, using the integral

$$I(f,g) = \int f(x) log(\frac{f(x)}{g(x|\theta)}) dx \tag{3.4.1}$$

This integral I gives the information lost when $g$ is used to approximate $f$. So, minimizing $I(f,g)$, the model that loses as little information as possible, is determined.
The precedent integral can be written equivalently as

$$I(f,g) = \int f(x)log(f(x))dx - \int f(x)log(g(x|\theta))dx \tag{3.4.2}$$

where $\theta$ is the models space where $g(x)$ varies.
It is possible to write this formula through the expected value.

$$E[x] = \int_{-\infty}^{\infty} xf(x)dx \tag{3.4.3}$$

$$I(f,g) = E_f[log(f(x)] - E_f[log(g(x|\theta)] = K - E_f[log(g(x|\theta)] \tag{3.4.4}$$

or

$$I(f,g) - K = -E_f[log(g(x|\theta)] \tag{3.4.5}$$

so the term $I(f,g) - K$ is the distance between models $f$ and $g$.
A few decades later, *Akaike (1973)* proposed using Kullback-Leibler information for model selection. He established a relationship between the maximum likelihood, which is an estimation method used in many statistical analyses, and the Kullback-Leibler information, with a constant that is approximately equal to $k$, the number of estimable parameters in the approximating model.
The general expression of AIC is:

$$AIC = 2k - 2\ln(L) \tag{3.4.6}$$

where $k$ is the parameters number and L is the bestfit value of misfit function.
The $AIC$ can be correct if the number of data $n$ is small using the expression given by *McQuarrie et al. (1998)*

$$AICc = 2\ln\frac{M_1}{n} + \frac{n+k}{n-k-2} \tag{3.4.7}$$

where $M_1$ is the $\mathscr{L}^1$-norm misfit. The use of AICc is strongly recommended, rather than $AIC$, if $n$ is small or $k$ is large. Since $AICc$ converges to $AIC$ as $n$ gets large, $AICc$ generally should be employed regardless.
The competing model with the smallest $AICc$ is most likely to be correct. The individual values of the $AICc$ are not interpretable because they contain arbitrary constants and are affected by the sample size. Only the $AICc$ difference ($\Delta AICc$) is significant when comparing two competing models. A simple rule of thumb states that if $\Delta AICc < 2$ the two models have similar support from data, if $4 < \Delta AICc < 7$ the two models have considerably different support, while if $\Delta AICc > 10$ the larger-$AICc$ model has essentially no support *(Burnham and Anderson, 2004)*.

# Chapter 4

# Paired deformation sources of the CF caldera

## 4.1 Analysis of large-signal pre-2000 periods

The aim of this thesis is to find a simple model that explains the CF deformation field during the last forty years (1970-2013). In this chapter the period 1970-2010 is covered using different types of data, with different peculiarities and which give different information about the analyzed area. As seen in previously chapters, same periods are covered by different types of data:

- 1970-1994 -> Leveling data
- In 1980 and in 1983 -> Geodetic precise traversing data
- 1993-2010 -> Sar data

Firstly we have analyzed ground displacement data in order to discern similarities or differences between CF inflation and deflation periods and highlight possible anomalies in particular areas of the CF caldera. Our first step was analyzed ground deformation pattern between the major 1982-84 inflation and subsequent deflation, focusing on periods with large signals and constant ratio. Tested periods ( 1970-75, March 1970 to May 1975; 1980-83, June 1980 to June 1983; 1983-84, June 1983 to October 1984; 1985-88, January

1985 to December 1988; 1989-92, June 1989 to December 1992; 1995-2000, March 1995 to end 1999) are shown in Figure4.1. With regard to SAR data, each pixel has a scattered

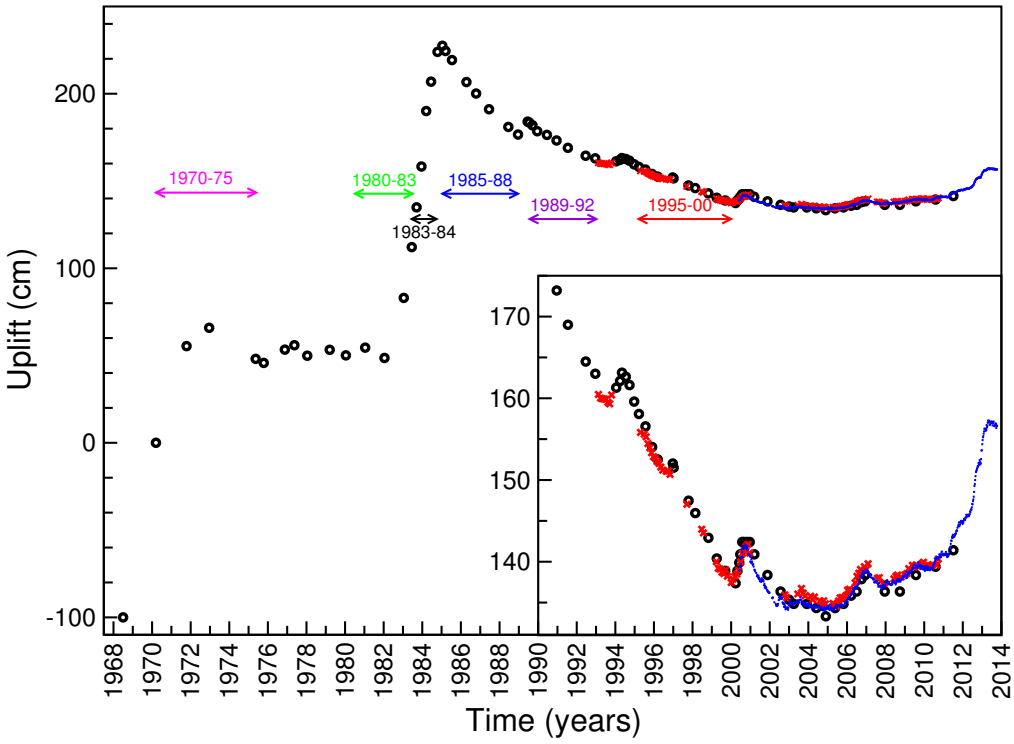


Figure 4.1: Ground level changes at the leveling benchmark 25A, located in the area of maximum uplift (see figure 1.4). Black circles, leveling data (digitized from www.ov.ingv.it); red crosses, estimated vertical displacements from SAR images. Colored double-ended arrows indicate the periods compared in figures 4.4. An enlarged y-scale is used in the inset.

trend, so to reduce noise, we estimated pixel-wise SAR LOS displacements for 1995-2000 by fitting (least absolute deviation) a straight line to the displacement history, on the ascending and descending orbit, of each pixel. Figure 4.2 shows examples of fitting lines for four different pixels (red circle in the inset map), located in the area of maximum displacement. These ascending and descending displacement histories are different because of the different viewing geometry of the radar satellite. In particular, we have properly combined the ascending and descending deformation time series in order to retrieve the east-west (EW) and vertical deformation components on a regular (150 m $\times$ 150 m) incomplete grid, because the LOS viewing is expressed by its direction cosines with respect to the geocentric XYZ reference system. In this case direction cosines are

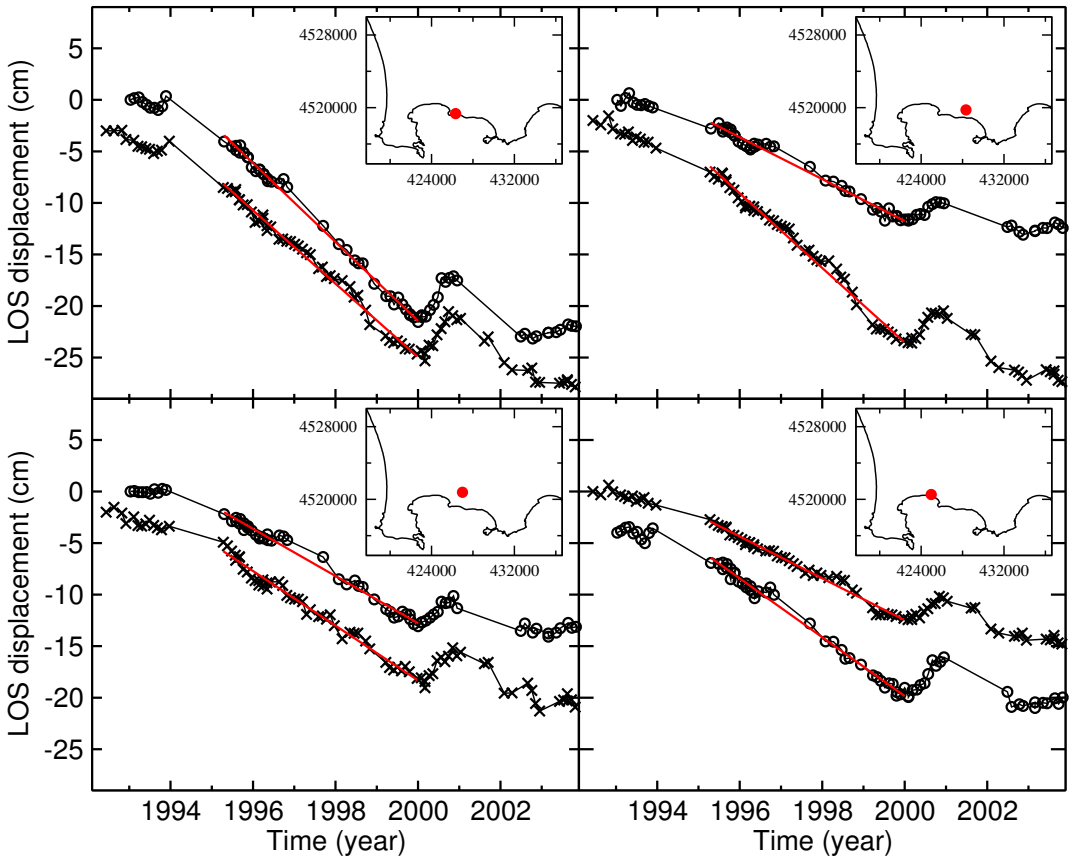


Figure 4.2: LOS displacement on ascending (circles) and descending orbit (crosses) and examples of fitting with a straight line for four different areas of the CF caldera (red full circles).

Ascending: $North = -0.082521154$, $East = -0.38107129$, $Up = 0.92085553$;

Descending: $North = -0.07510573$, $East = 0.35541612$, $Up = 0.93168585$;

It is assumed that the ascending and descending radar LOS directions, belong to the East-Z plane and the look-angle, are the same for both ascending and descending geometries. The data do not provide information about the North–South component; because of the viewing geometry of the radar satellite, we cannot detect displacements in the North–South direction being this latter roughly parallel to the orbit track.

The time histories of eastward and vertical displacements on a regular (150 m $\times$ 150 m) incomplete grid has been estimated as follows. The circular area (150 m in radius) centered on each node is divided into four sectors. The node is accepted only if the occupancy

condition of at least one pixel inside at least two of the four sectors is satisfied for both ascending and descending LOS displacements.
We selected ascending and descending SAR acquisitions whose lag is shorter than one week, and interpolated selected pixel-wise SAR data to estimate LOS displacements on each accepted node using BIVAR *(Akima et al.,1984)* and QSHEP2D *(Renka et al., 1988)* codes to cross-validate results. Gridded ascending and descending LOS displacements were combined to obtain eastward and vertical displacements. Because of LOS geometry, the accuracy of the technique can be estimated to be $\pm$ 0.5 cm for vertical displacements and $\pm$ 1.4 cm for eastward displacements. Ascending and descending displacements and estimated vertical and eastward displacements are shown in Figure 4.3. Vertical displacements exhibit a quasi-axisymmetric pattern, but seem slightly elongated NW-SE.
To compare SAR data with other types of data (leveling and geodetic precise traversing), we follow the same interpolation and combination procedure to estimate 1995-2000 eastward and vertical displacements as close as possible (given ascending and descending pixel locations) to leveling and EDM benchmarks.

## 4.2 Cross-comparisons and the need for two sources

In order to discern similarities or differences between CF inflation and deflation periods, we compared the vertical displacement first. We use BIVAR to have eastward and vertical displacements as close as possible (given ascending and descending pixel locations) to leveling benchmarks. Vertical displacements related to the above-listed six periods are compared in Figure 4.4. Each dataset is rescaled to match the 1980-83 one in the area of maximum uplift (benchmarks from nine to twelve in figure 4.4). The agreement is nearly perfect, apart from benchmarks in the Solfatara area (red double-ended arrow) and immediately South of it (black double-ended arrow), where a local deformation source, with a different time history, seems superposed on the large-scale one. As shown in figure 1.4 the Solfatara area is covered by leveling benchmarks only from 1983, so we have only four periods to compare. In Figure 4.5 we compare 1980-83 eastward EDM benchmark displacements with respect to the radiating center (black star), as explained in chapter 1, and 1995-2000 eastward SAR displacements (multiplied by -3.2 like coeval uplifts in Figure 4.4), showing that they are equal within the uncertainty of the datasets.

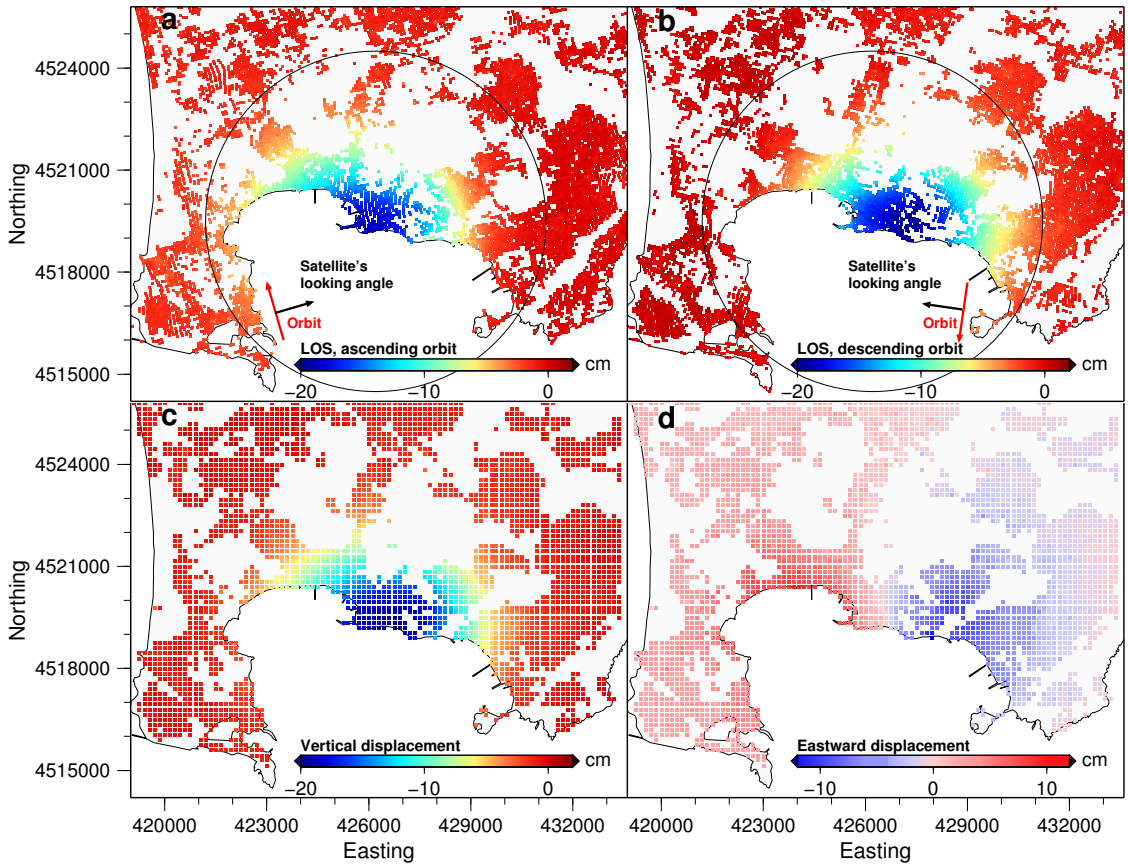


Figure 4.3: 1995-00 displacements from SAR data. (a) LOS displacements from ascending orbits. (b) LOS displacements from descending orbits. (c) Estimated vertical displacements on a regular (150 m $\times$ 150 m) incomplete grid. (d) Estimated eastward displacements on a regular (150 m $\times$ 150 m) incomplete grid. The black circle in (a) and (b) borders the pixels used to obtain the Solfatara local deformation source parameters.

We can conclude that the deformation pattern was probably the same during the tested periods, excluding the Solfatara area. Consequently, overall CF deformation asks for (at least) two sources, the former satisfying large-scale deformation, the latter satisfying additional deformation in the Solfatara area.

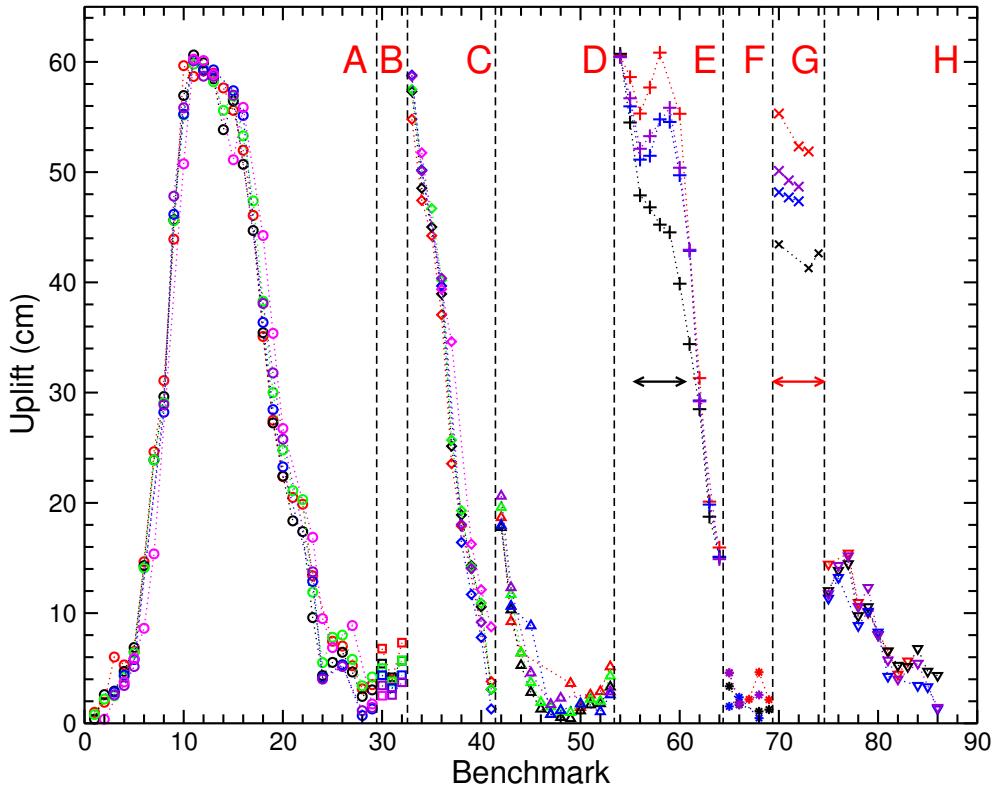


Figure 4.4: Vertical displacements at leveling benchmarks. Symbols and capital letters indicate the leveling routes as in Figure 1.4. Colors indicate the same periods as the double-ended arrows in Figure 4.1: magenta, 1970-75 (multiplied by 1.25); green, 1980-83; black, 1983-84 (multiplied by 0.54); blue, 1985-88 (multiplied by -1.28); violet, 1989-92 (multiplied by -2.86); red, 1995-00 (from SAR data, multiplied by -3.2). The red (black) double-ended arrow indicates benchmarks at (South of) Solfatara.

## 4.3 Inversion of ground displacements, june 1980 to june 1983

The previous figure 4.4 suggests the possibility that one simple source is enough to satisfy large-scale deformation, and another simple source satisfies additional deformation in the Solfatara area. Firstly we analyzed the 1980-83 period, because it is characterized by a strong uplift (about 60 cm), and both vertical (from levelings) and horizontal (from precise traversing) displacements are available, in order to find a source that satisfies the large scale deformation. Solfatara is not covered by 1980-83 data, reducing contaminations from the local deformation anomaly.

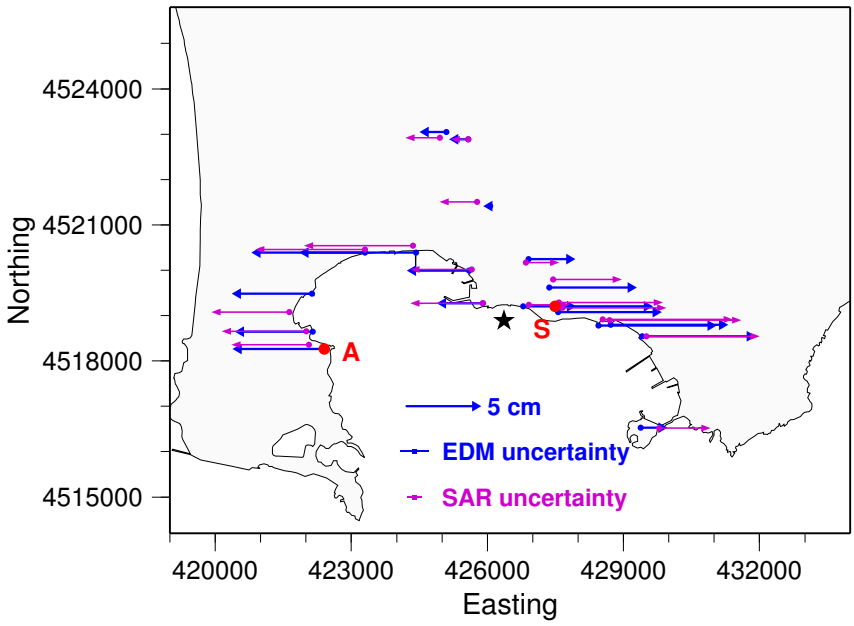


Figure 4.5: Comparison between blue arrows, eastward component of 1980-83 displacements, with respect to the radiating center and magenta arrows, 1995-00 eastward displacements reversed in sign and multiplied by 3.2; magenta bar, eastward SAR uncertainty (±1.4 cm, here rescaled as done for 1995-00 displacements). A and S are like in figure 1.5

### 4.3.1 Inverted data

To the inversion we used leveling and geodetic precise traversing data, as introduced in chapter 1. As regards horizontal ground displacements, we consider two different data sets, namely the 13 benchmark distance changes (BDC) reported in *Dvorak and Berrino (1991)* and widely used in the past *Battaglia et al. (2006*), and the 19 adjusted benchmark displacements (ABD) given in *Barbarella et al., (1983)* with respect to a local non-fixed reference system (origin at benchmark S, y axis from S to A, see inset in Figure 1.5 ). For both BDC and ABD, benchmark coordinates are obtained from those given in *Barbarella et al., (1983)* with respect to the above-mentioned local reference system. For BDC, we assume that distance changes are statistically independent of one another, even if the dataset was actually obtained from benchmark adjusted position changes (G. Berrino, personal communication). Following *Barbarella et al., (1983)*, we attribute the same error to all distance changes to take also account of systematic errors, as centering errors and the approximations of the atmospheric model adopted for data reduction. The adopted value (0.01 m) is not crucial because we use a variable factor to weight horizontal displace-

ments with respect to vertical ones in the misfit function. For ABD, we compute model predictions of horizontal displacements in Barbarella's local reference system. The data covariance matrix is not diagonal because of the adjustment procedure *(Ghilani and Wolf, 2012)*, and, unfortunately, cannot be computed because of lack of information about the surveys and the adjustment procedure. For the sake of simplicity we treat displacements in Barbarella's reference system as independent data, using uncertainties given in *Barbarella et al., (1983)*. Again, adopted uncertainties are not crucial because we use a variable factor to weight horizontal displacements with respect to vertical ones in the misfit function.
As already mentioned, original leveling data (section height differences) are not available and only adjusted benchmark heights can be used. Levelings surveys were carried out in January 1980, January 1981, and June 1983 *(Dvorak and Berrino, 1991)*. To get coeval leveling and precise traversing data, June 1980 adjusted benchmark heights have been estimated by averaging the January 1980 and January 1981 ones. The initial data set consists of 73 adjusted benchmark uplifts from June 1980 to June 1983. We have removed benchmarks whose coordinates differ by more than 200 m between our dataset (courtesy of G. Berrino) and the INGV WebGIS (http://ipf.ov.ingv.it/cf_gis.html) and we have removed benchmarks whose uplift time histories include evident anomalous values and steps (e. g. because of benchmark damage and reconstruction) from the dataset. The final set consists of 53 adjusted benchmark uplifts (as shown in figure 1.4 in chapter 1). The uplift covariance matrix is not diagonal and cannot be computed exactly because of lack of information on original measurements and the adjustment procedure.
We use a non-diagonal covariance matrix obtained by combining the non-diagonal covariance matrix due to leveling measurement errors (0.0024 $m/\sqrt{\text{km}}$, proportional to $\sqrt{L}$, $L$ being section length in km) and the diagonal covariance matrix due to non-measurement errors, under the simple hypothesis of uncorrelated non-measurement errors on benchmark uplifts (0.01 m, estimated as in *Amoruso and Crescentini, 2007*).

### 4.3.2 Tested sources and inversions

As seen in chapter 3, in this thesis, misfit function optimization is obtained, firstly, using Adaptive Simulating Annealing *(Ingber, 1993)*. ASA aims to find the best global fit of a non-linear misfit function over a multidimensional parameters space; it ensures an ample global searching in the first phase of search and ample quick convergence in the

final phase, self-optimizing its program options recursively. We minimize the absolute deviation of residuals (L1-norm misfit function), appropriate for two-sided-exponentially distributed residuals and commonly used for robust fitting

$$\mathscr{L}^1 = \sum_{j=1}^{2} w_j \sum_{i=1}^{N_j} \left| \frac{x_i - f_i(a)}{\sigma_i} \right| \tag{4.3.1}$$

where $x_i (i = 1,...,N_j)$ indicates independent data, $f_i(a)$ is model prediction of $x_i$ given model parameters $\mathbf{a}$, and $\sigma_i$ is uncertainty of $x_i$. From the maximum likelihood point of view, all the weights $w_j$ should be 1 independently of how many data are in each data set, provided that uncertainties have been estimated correctly. Subsequently we used the neighbourhood algorithm (NA), as introduced in chapter 2.

While ASA is better than NA to provide a global minimum, the NA instead is able to generate ensembles of model parameters which preferentially sample the good data fitting regions of the parameter space, and than is also used for global optimization.

Like for any other Monte Carlo method, success in finding the optimal model parameters is never guaranteed by ASA or NA. We cross-check ASA and NA inversions to increase confidence in the results.

Firstly, single-source models are tested, for the CF large-scale deformation and all tested sources are considered embedded both in an elastic homogeneous half-space and in a layered one (Table 2.1). In chapter 2, the importance of stratification in the inversion procedure is introduced, the elastic parameters used in this thesis and the six tested sources, that are

1. one pressurized point spheroidal cavity having a vertical axis of symmetry *(*5 free parameters*, Amoruso et al., 2008),*

2. one pressurized finite horizontal circular crack (5 free parameters*, Crescentini and Amoruso, 2007),*

3. one pressurized finite spheroidal cavity having a vertical axis of symmetry, mathematically modeled under the quadrupole approximation (6 free parameters*, Amoruso and Crescentini, 2011),*

4. one pressurized finite triaxial ellipsoidal cavity, mathematically modeled under the

quadrupole approximation (10 free parameters*, Amoruso and Crescentini, 2011),*

5. one rectangular uniform-opening tensile fault (8 free parameters*, Okada, 1985; Wang et al., 2006),*

6. one moment tensor (9 free parameters*, Aki and Richards,1984)*.

Recent studies proposed multiple sources with different features acting in different periods *(Gottsmann et al., 2006b)*, fluid injections implying large changes of the large-scale deformation pattern over time *(Troiano et al., 2011)*, complex spatial and temporal patterns of distributions of volumetric sources *(D'Auria et al., 2012)*.
The sources, tested in this thesis, cover and extend the whole ensemble of sources used in previous works for the inversion of ground deformation data related to the major 1982-1984 uplift.

### 4.3.3 Inversion results

As already obtained in *Amoruso et al. ( 2008)* and *Amoruso et al. (2007a)* for axisymmetric sources, here again we find that sources embedded in a homogeneous medium cannot give a good simultaneous fit to vertical and horizontal ground displacements, whereas incorporating the layered structure detailed in Table 2.1 allows a significantly lower (up to 50\%) misfit for any tested source.
Moreover, source parameters and model ranking obtained using BDC and ABD are quite similar, (ii) as already mentioned, to our best knowledge BDC (as well as distance changes in other papers on 1980-83 CF deformation) were actually obtained from adjusted benchmark coordinates, (iii) trade-off plots indicate that the "knee" region is around $w_2 = 1$ for both BDC and ABD. Thus we only show results related to the layered half-space, using uplifts and ABD, with $w_2 = 1$.
As introduced in chapter 3 we can choose the "best model", among a set of different types of models, using the Akaike's Information Criterion. Perhaps none of the models in the set are good, but AIC attempts to select the best approximating model of those in the candidate set. The competing model with the smallest *AICc* is most likely to be correct. As seen in chapter 3, only the *AICc* difference ($\Delta AICc$) is significant when comparing two competing models.

| | Source | Misfit | AICc |
|---|---|---|---|
| 1 | Point vertical spheroid | 82.6 | 89.9 |
| 2 | Finite circular crack | 62.6 | 41.1 |
| 3 | Finite vertical spheroid | 60.0 | 36 |
| 4 | Finite triaxial ellipsoid | 52.5 | 22.6 |
| 5 | Finite tensile fault | 54.8 | 24.9 |
| 6 | Moment tensor | 60.0 | 43.5 |

Table 4.1: Misfits and AICcs of Best-fit Sources, 1980-83 data

A simple rule of thumb states that if $\Delta AICc < 2$ the two models have similar support from data, if $4 < \Delta AICc < 7$ the two models have considerably different support, while if $\Delta AICc > 10$ the larger-*AICc* model has essentially no support. Misfits and *AICcs* (Table 4.1) indicate that the non-axisymmetric point source (#6) is strongly favored with respect to the axisymmetric one (#1) ($\Delta AICc = 46.4$), and the non-axisymmetric finite sources (#4 and #5) are strongly favored with respect to the axisymmetric ones (#2 and #3; retrieved polar axis of source 3 is much shorter than the equatorial one) ($\Delta AICc = 11.1$ and $\Delta AICc = 18.5$ respectively).

The pressurized triaxial ellipsoid (source 4, hereinafter referred to as PTE) and the tensile fault (source 5, hereinafter referred to as TF) are strongly favored with respect to all the other sources, ( $\Delta AICc = 2.3$ ), so the two models have a similar support from data.

"Optimal" PTE and TF parameters returned by ASA and NA are always very close to those listed in Table 4.2, hereinafter chosen as reference PTE and TF.

Often, find the range of parameters values is more important than discover their "optimal" values; in this sense becomes really important to have MPDFs of PTE and TF parameters. The MPDFs are shown in figure 4.6; from this figure we gather that source centers are almost co-located, volume changes are quite similar, and both sources suggest opening of a quasi-horizontal elongated crack oriented NW to SE.

| Parameters | PTE | TF |
|---|---|---|
| Est (m) | 426167 | 426156 |
| North (m) | 4518919 | 4518940 |
| Depth (m) | 3603 | 3553 |
| Volume change ($10^7\,m^3$ ) | 1.65 | 1.61 |
| Longest semi-axis (m) | 2256 | n. a. |
| Intermediate semi-axis (m) | 1979 | n. a. |
| Shortest semi-axis (m) | 99 | n. a. |
| Overpressurea (MPa) | 18.5 | n. a. |
| $\alpha$(deg) | 34.6 | n. a. |
| $\beta$(deg) | 90.2 | n. a. |
| $\gamma$(deg) | 94.7 | n. a. |
| Length (m) | n. a. | 3884 |
| Width (m) | n. a. | 2466 |
| Azimuth (deg) | n. a. | 113.0 |
| Dip (deg) | n. a. | -6.6 |

Table 4.2: TF and PTE source parameters

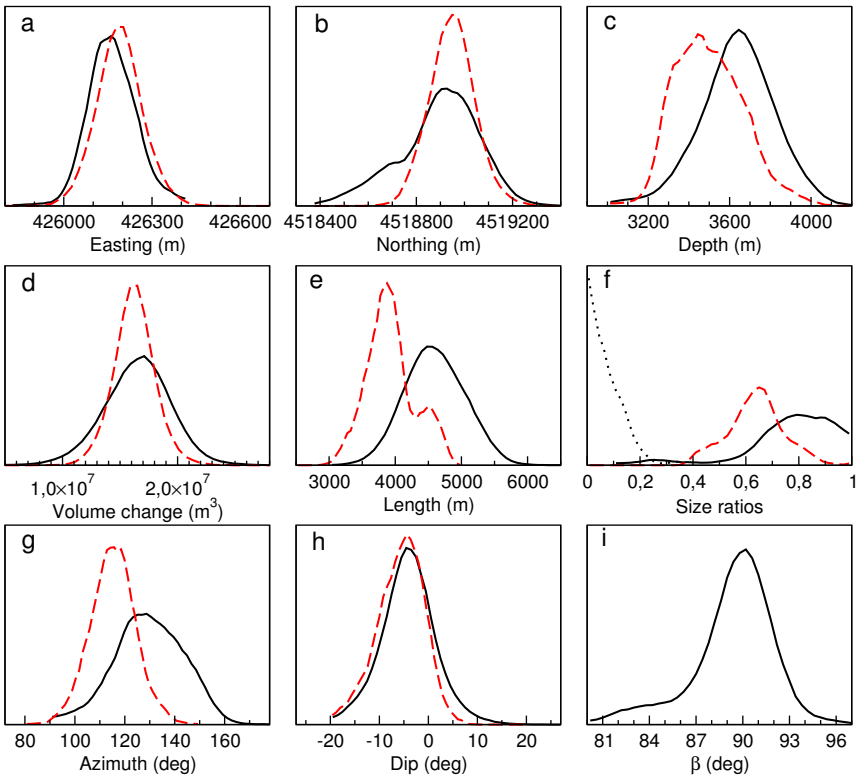


Figure 4.6: Marginal PDFs of 1980-83 PTE (black solid lines) and TF (red dashed lines) parameters. The label "Size ratios" (plot f) refers to intermediate-to-longest axis for PTE and width- to-length for TF; the dotted line gives shortest-to-intermediate axis for PTE. We use $90° + \alpha$ for estimating PTE azimuth and $90° - \gamma$ for estimating PTE dip because $\beta \approx 90°$

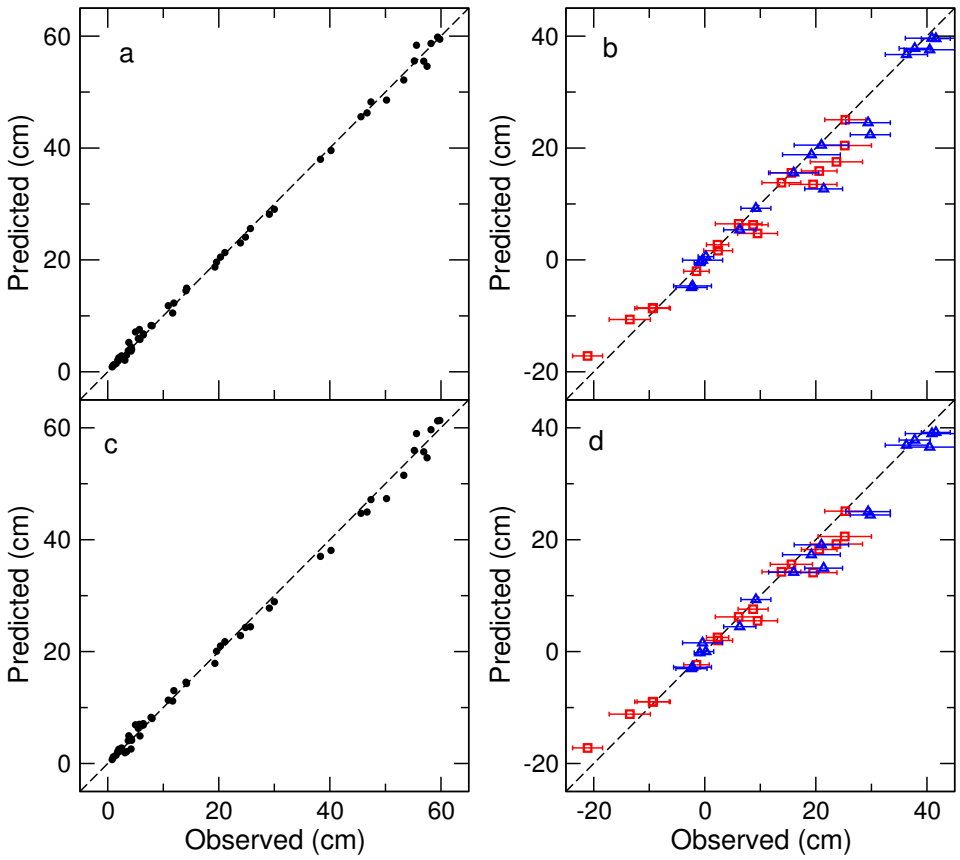


Figure 4.7: 1980-83 PTE (a and b) and TF (c and d) model predictions compared with observations. (a) and (c), vertical displacements; no error bar is shown because vertical displacements are not independent data. (b) and (d), horizontal displacements in Barbarella's local reference system (inset in Figure 1.5); red squares, x-displacement; blue triangles, y-displacement.

Figure 4.7 compares model predictions and observations for reference TF and PTE. Deviations with respect to the perfect correlation line are, for the most part, within data uncertainties (1 standard deviation), the most noticeable exception being y-displacement of EDM benchmark C (see Figure 1.5), and no systematic misestimate is visible.

The lack of systematic misestimates still holds for the best-fit moment tensor. In *Trasatti et al., (2011),* best fitting moment tensors are incompatible with any pressurized ellipsoid or crack, infact there is a systematic underestimate of horizontal displacement data in their single-source moment-tensor models.

They interpret their best fit moment tensor in terms of a mixed mode (shear and tensile) dislocation at 5.5 km depth, striking EW and dipping by ~ 25°–30° to the North, but also

in this model, the underestimation of horizontal displacement data, although to a minor extent, is persisted.

Figure 4.7 also shows that TF gives a slightly better fit to y-displacements with respect to PTE, while PTE gives a slightly better fit to uplifts with respect to TF. As a consequence, small changes in $w_2$ favor TF or PTE. To discover how much is different, in results, using TF or PTE, in figure 4.8 there are the difference between TF and PTE northward, eastward and vertical displacement. Remarkable differences are present in the sea area, particularly for the north component, on dry land the only differences are present in areas that are not covered (or little covered) by SAR or leveling. In practice, using TF or PTE for computations, does not affect results because predicted ground displacements by reference PTE and TF are almost indistinguishable, at least in dry land (see Figure 4.8). Hereinafter we use reference PTE (see Figure 4.9 c for its center location) and its theoretical displacements are shown in figure 4.8 (a, c and f).

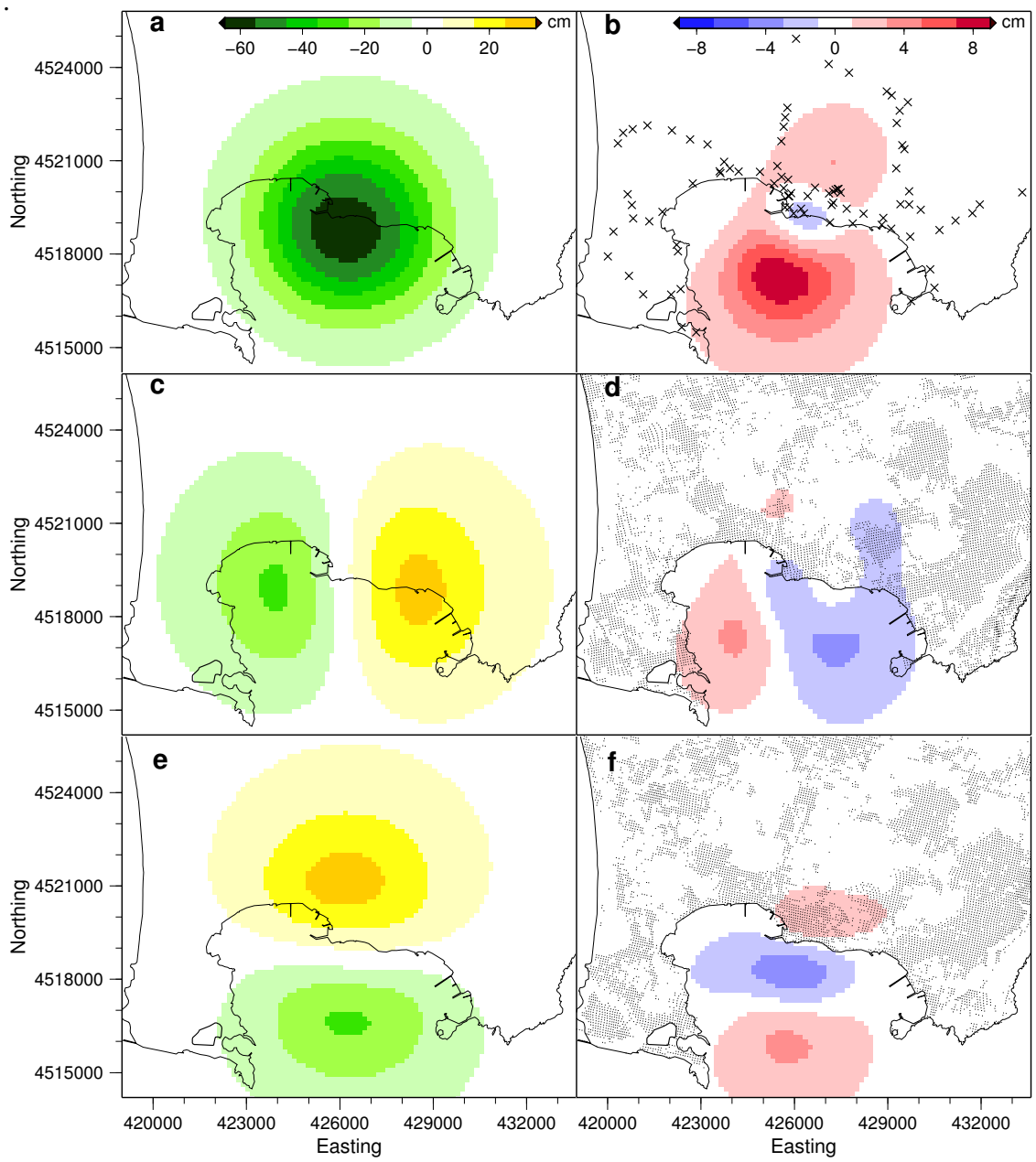


Figure 4.8: Ground displacement maps for reference PTE and TF. (a) PTE vertical displacement; (b) difference between TF and PTE vertical displacement; (c) PTE eastward displacement; (d) difference between TF and PTE eastward displacement; (e) PTE northward displacement; (f) difference between TF and PTE northward displacement. Crosses in (b), leveling benchmarks; dots in (d), ascending orbit pixels; dots in (f), descending orbit pixels.

## 4.4 1995-2000 deflation

As seen in chapter 1, InSAR data give superficial displacement maps of almost entire CF and this good spatial coverage is useful to investigate the Solfatara area. We compute ascending and descending LOS displacements from reference PTE, using $\Delta V_{\mathrm{PTE}} = -5.2 \times 10^6$ m$^3$, that is the $\Delta V$ of PTE, founded from 1980-83 data inversion, rescaling using the same factor of Figure 4.4, and subtract them from 1995-2000 pixel-wise LOS displacements (Figure 4.9 a and b), thus obtaining residual LOS displacements. Figure 4.9 (c and d) shows ascending and descending residuals with respect to PTE. For the sake of visual inspection easiness, figure 4.10 (a and b) shows the vertical and eastward displacements on the above-described regular (150 m$\times$ 150 m) incomplete grid and vertical and eastwards residuals with respect to PTE. Residuals are generally consistent with SAR uncertainties ($\pm$0.5 cm for vertical displacements and $\pm$1.4 cm for eastward ones) apart from the Solfatara area, where a noticeable anomaly is evident.

The anomaly is much more localized than large-scale deformation and suggests the presence of a local quasi-axi-symmetric shallower source.The presence of two sources, is suggested from the comparison of vertical displacements, related to the above-listed six periods, (figure 4.4) and from previously SAR residuals. To find this other possible source, we invert 1995-2000 LOS displacements of pixels located inside a circle, 5000 m in radius, centered on the maximum uplift area (see Figure 4.9, a and b) using a two-source model embedded in the layered medium of Table 2.1. The first source is reference PTE, whose volume change is left free in the inversion. As second source, we use a small (point) pressurized spheroid (PS) having vertical symmetry axis; location, aspect ratio, and volume change are left free in the inversion. The inversion is performed as already described for 1980-83.

Obviously the most correct procedure should be to leave free all the parameters of PTE and not only the volume change, but in this case there would be too many parameters (15) in the inversion and the results would be too unstable; in addition, the machine time would be very long. From the previous comparison, we have seen that vertical and eastward displacements for 1980-83 and 1995-00 are the same (properly scaled), so the large scale source is the same and fix the PTE source with only volume change left free, is correct. We have also executed some tests using a finite spheroid, but it always degenerated into a point one.

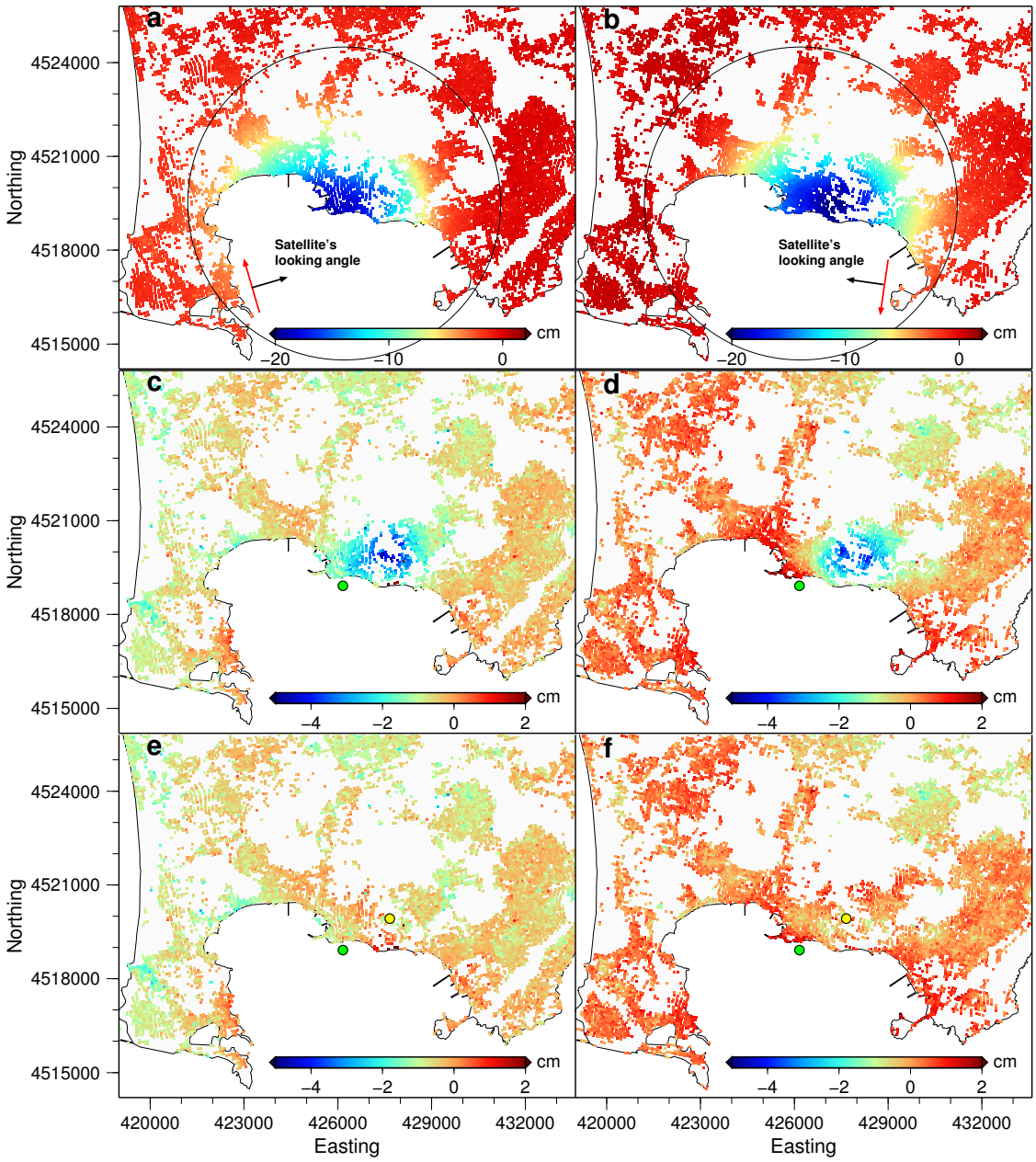


Figure 4.9: 1995-00 SAR ascending (a) and descending (b) displacements. Inverted data in the black circles, 5000 m in radius, centered on the maximum uplift area. Maps (c) and (d): ascending and descending residuals after subtracting predictions for the 1980-83 reference PTE divided by -3.2 (i. e. $\Delta V_{PTE} = -5.2 \times 10^6 m^3$ ) from SAR displacements; filled green circle, PTE center; Maps (e) and (f): residuals after subtracting predictions for reference PS and PTE (with $\Delta V_{PTE} = -5.2 \times 10^6 m^3$ ) from SAR displacements; filled yellow circle, spheroid center; crosses, main fumaroles.

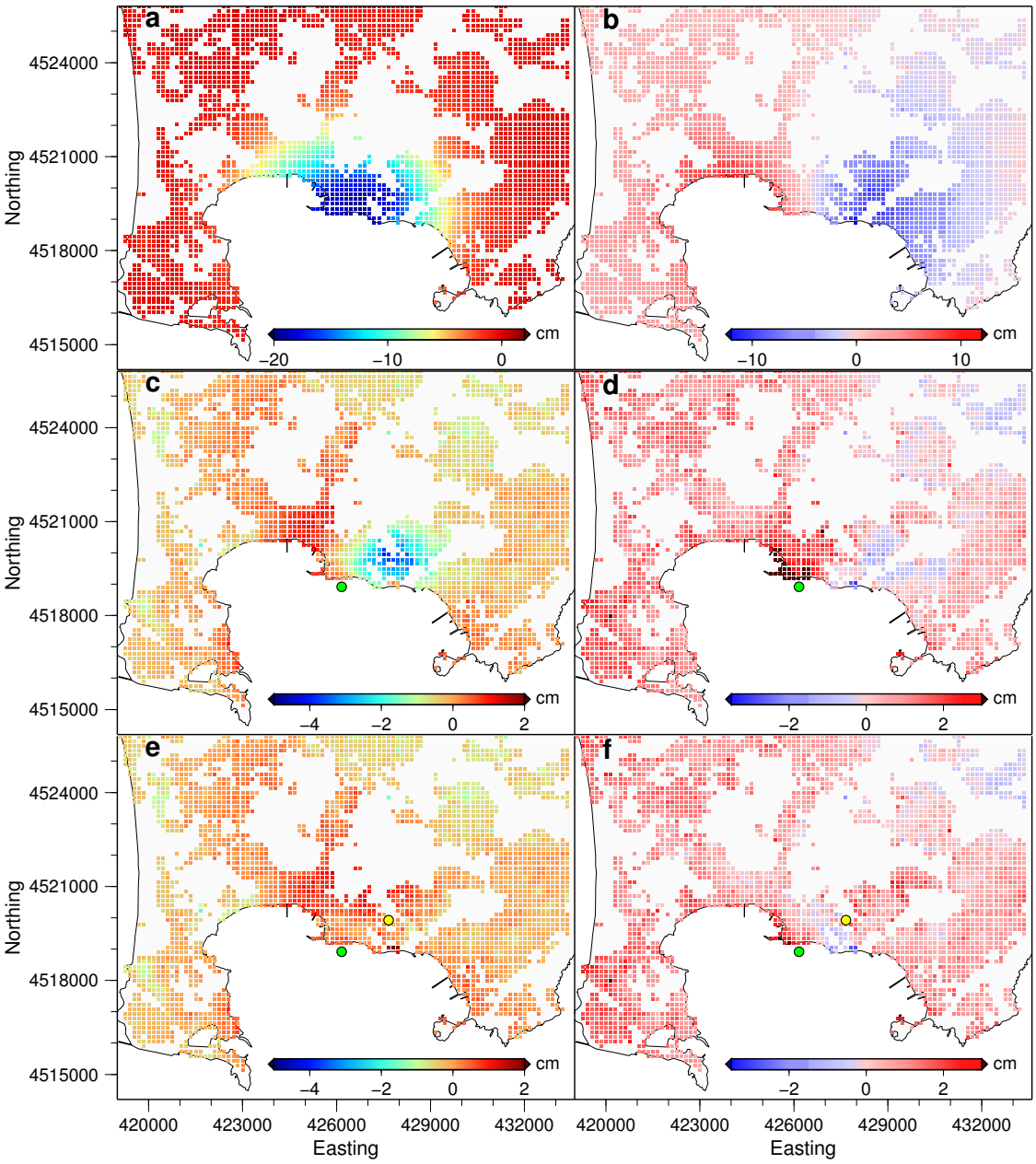


Figure 4.10: 1995-00 vertical (a) and eastward (b) displacements on an incomplete regular grid (150 m × 150 m). Maps (c) and (d): residuals after subtracting predictions for the 1980-83 reference PTE divided by -3.2 (i. e. $\Delta V_{PTE} = -5.2 \times 10^6 m^3$ ) from vertical and eastward displacements; filled green circle, PTE center. Maps (e) and (f): residuals after subtracting predictions for reference PS and PTE ( with $\Delta V_{PTE} = -5.2 \times 10^6 m^3$ ) vertical and eastward displacements; filled yellow circle, spheroid center; crosses, main fumaroles.

"Optimal" parameters returned by ASA and NA are always very close to those listed in Table 4.3, hereinafter chosen as reference PS, and to $\Delta V_{\mathrm{PTE}}$ given in its footnote. MPDFs of PS parameters and PTE volume change are shown in Figure 4.11. Evident trade-offs

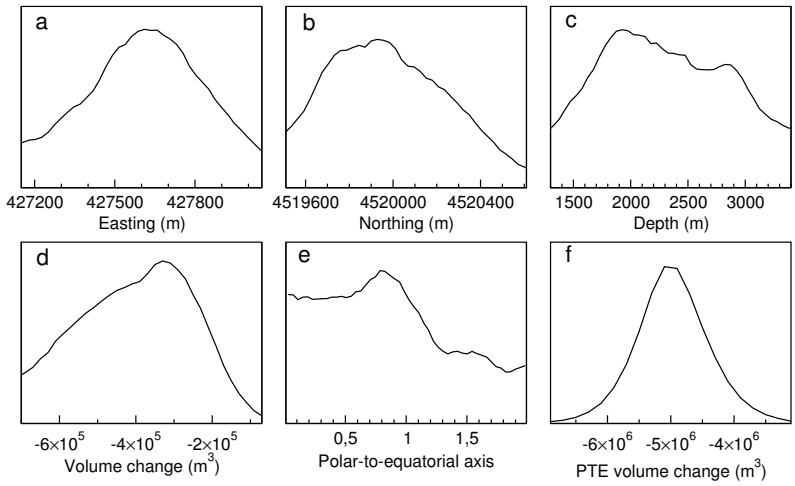


Figure 4.11: Marginal PDFs of 1995-00 PS parameters (a to e) and PTE volume change (f).

link volume change and aspect ratio of the PS to its depth (Figure 4.12). This finding is not surprising. A reliable estimate of the source depth is obtainable only if vertical and horizontal ground displacements are considered *(Dieterich and Decker, 1975)*, while SAR LOS displacements are mainly sensitive to vertical ones. We have conducted a simple numerical experiment of using point spheroids to match synthetic vertical displacements generated by an isotropic point (Mogi) source embedded in a homogeneous elastic half-space. Results show clear trade-offs (similar to those in Figure 4.12) between estimated aspect ratio (and volume change) and depth of the point spheroids, while synthetic data are always fitted very well. Figure 4.10, c and d, shows 1995-2000 vertical and eastward residuals after subtracting predictions from reference PTE (using its "optimal" volume change $\Delta V_{\mathrm{PTE}} = -5.02 \times 10^6$ m$^3$) and PS. No additional source seems to be required by SAR data, since LOS mean absolute deviation (0.35 cm for the pixels used in the inversion) is within data uncertainties and no localized anomaly is evident. In conclusion, the two-source model satisfies overall CF deformation during 1980-83 and 1995-2000. The first source is reference PTE (parameters in Table 4.2) with different volume changes ($1.65 \times 10^7$ m$^3$ and$-5.02 \times 10^6$ m$^3$ respectively). The second source is reference PS (parameters in Table 4.3, note that 1980-83 data do not include measurements affected by

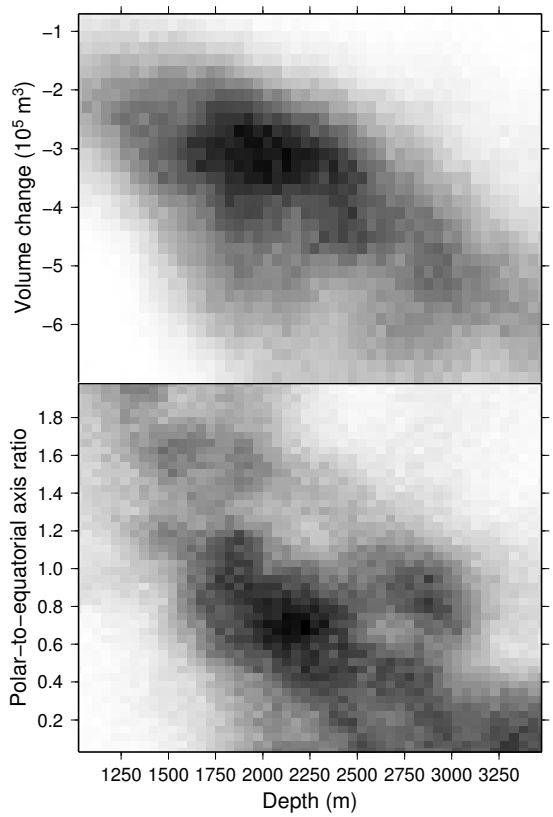


Figure 4.12: 2D marginal PDFs of 1995-00 PS polar-to-equatorial axis ratio and volume change versus depth.

PS appreciably).

## 4.5 Large-signal pre-2000 periods

The crucial aspect is if this simple model can explain the CF deformation during the last forty years (1970-2013). To verify this, firstly we test the two-source model on vertical displacement data related to the other large-signal pre-2000 periods (1983-84, 1985-88, and 1989-92; see Figure 4.1 ) and then check if the deformation pattern is stationary during the period of availability of SAR data. For the sake of comparison, we also consider 1995-2000 vertical displacements estimated from SAR data as close as possible to leveling benchmarks. If all source parameters but volume changes are kept constant (at values listed in Tables 4.2 and 4.3), predicted displacements from each source are proportional to

its volume change. Thus least squares fit has some advantages with respect to the minimization of the absolute deviation of residuals because it is mathematically much simpler and the misfit function has one global minimum. We estimate the volume change of both sources ($\Delta V_{\mathrm{PTE}}$ and $\Delta V_{\mathrm{PS}}$) for each period by means of multiple linear regressions using the data covariance matrix. Figure 4.13 shows comparisons between model predictions and observations and confirms the appropriateness of the two-source model for all the large-signal pre-2000 periods. $\Delta V_{\mathrm{PS}}$-to-$\Delta V_{\mathrm{PTE}}$ ratio is different from period to period (see caption of Figure 4.13), suggesting different time histories for the two source potencies. 1995-2000 volume changes obtained from vertical displacements at leveling benchmarks are very close to those obtained from the inversion of LOS displacements, confirming the capability of the benchmark net to resolve the local source at Solfatara.

| | |
|---|---|
| East (m) | 427659 |
| North (m) | 4519923 |
| Depth (m) | 1934 |
| $\triangle V\,(10^5 m^3)$ | -3.1 |
| Polar-to-equatorial axes ratio | 0.66 |

Table 4.3: Parameters of the reference Solfatara Point Spherical Source (PS), 1995-00 data. $\triangle V_{PTE} = -5.02 \times 10^6$

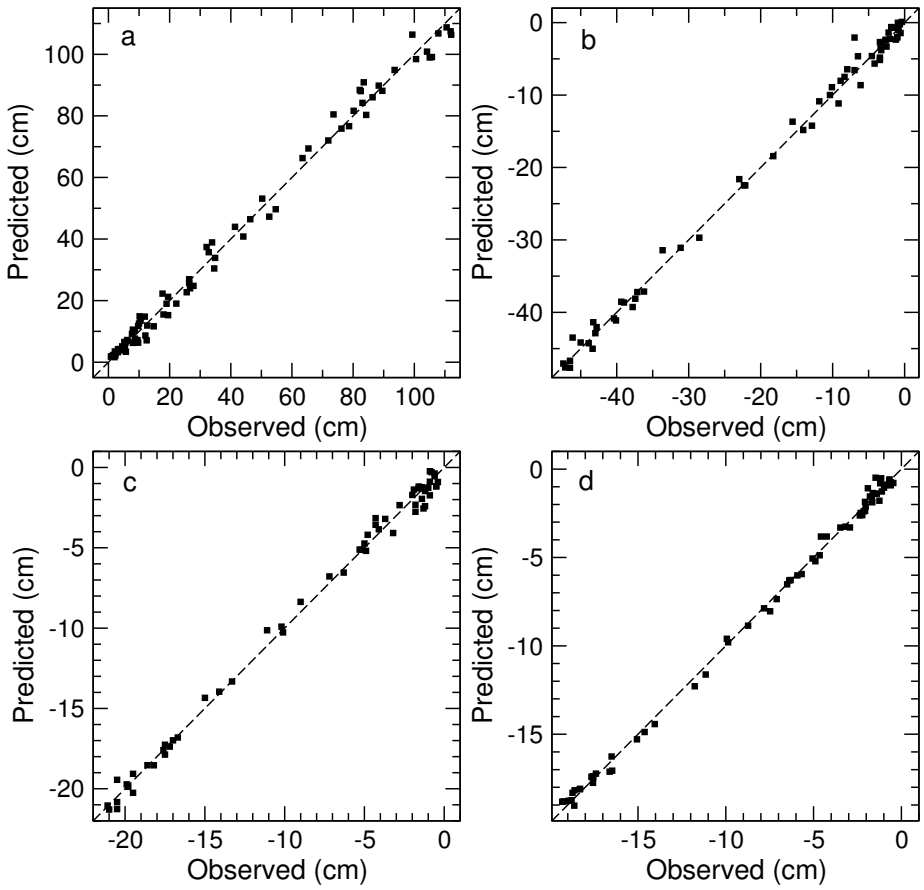


Figure 4.13: Comparisons between uplift model predictions and observations for tested large-signal pre-2000 periods. No error bar is shown because vertical displacements are not independent data. Here we give the root-mean-square deviation of residuals (RMSD) as intuitive goodness-of-fit indication. (a) 1983-84 ($\Delta$VPTE = 3.06 × 107 m3 , $\Delta$VPS = −4.5 × 105 m3 , RMSD = 3.2 cm); (b) 1985-88 ($\Delta$VPTE = −1.33 × 107 m3 , $\Delta$VPS = −1.87 × 105 m3 , RMSD = 1.2 cm); (c) 1989-92 ($\Delta$VPTE = −0.58 × 107 m3 , $\Delta$VPS = −1.14 × 105 m3 , RMSD = 0.5 cm); (d) 1995-00 ($\Delta$VPTE = −0.49 × 107 m3 , $\Delta$VPS = −3.05 × 105 m3 ), RMSD = 0.3 cm).

## 4.6 Appropriateness and potency time histories of the two-source model, 1970 to 2010

The second step is to check if the deformation pattern is stationary during the period of availability of SAR data. To prove this, we produce a correlation plot, left panel of figure 4.14, between the vertical displacement at different nodes of the grid of CF, which are representative of the behavior of the region, and the actual vertical displacement in the reference area. The time histories of vertical displacements are obtained from the spatial average of the pixels in a circular area in different regions of CF (black symbols in the inset maps). Points related to the nodes out of Solfatara are always very close to the best-fit 1993-1997 regression lines (indicating linear time-invariant correlation), while points related to Solfatara depart largely and non-randomly from the best-fit 1993-1997 regression line. Further support, to the anomalous behavior of Solfatara (with respect to CF as a whole), comes from the right panel of figure 4.14; it shows vertical displacements at the reference area and at the same nodes as in the left plane versus vertical displacement at Solfatara. Best-fit 1993-1997 regression lines prove the lack of linear time-invariant correlation between nodes out of and inside Solfatara. Correlation plots suggest the stationarity of the deformation pattern, except for the Solfatara area, during the availability period of SAR data. This confirms the thesis of two-source model during the whole investigated period (1970 to 2010).

It is important to exclude that the local deformation at Solfatara is only a mere distortion of large-scale deformation, e. g. because of local rheology or check if the two sources are connected to each other, so we estimate the time histories of the two volume changes ($\Delta V_{\mathrm{PTE}}$ and $\Delta V_{\mathrm{PS}}$) by means of multiple linear regressions, using the time histories of leveling benchmark uplifts (January 1980 to January 1994) and SAR vertical and eastward displacements data. SAR data are calculated from February 1993 to September 2010, inside a circle, 5000 m in radius, centered on the maximum uplift area, as shown in figure 4.9, a and b, and evaluated on a regular $150\times150m^2$ incomplete grid as previously described. Each date of the time histories is analyzed independently; we use (somewhat arbitrarily) the leveling survey of March 1984 as reference for computing benchmark height changes and February 1993 for SAR data. Since leveling benchmark heights are given with respect to a reference benchmark and SAR displacements are given with respect to a reference area, we leave uplift of the reference benchmark and vertical and eastward displacements

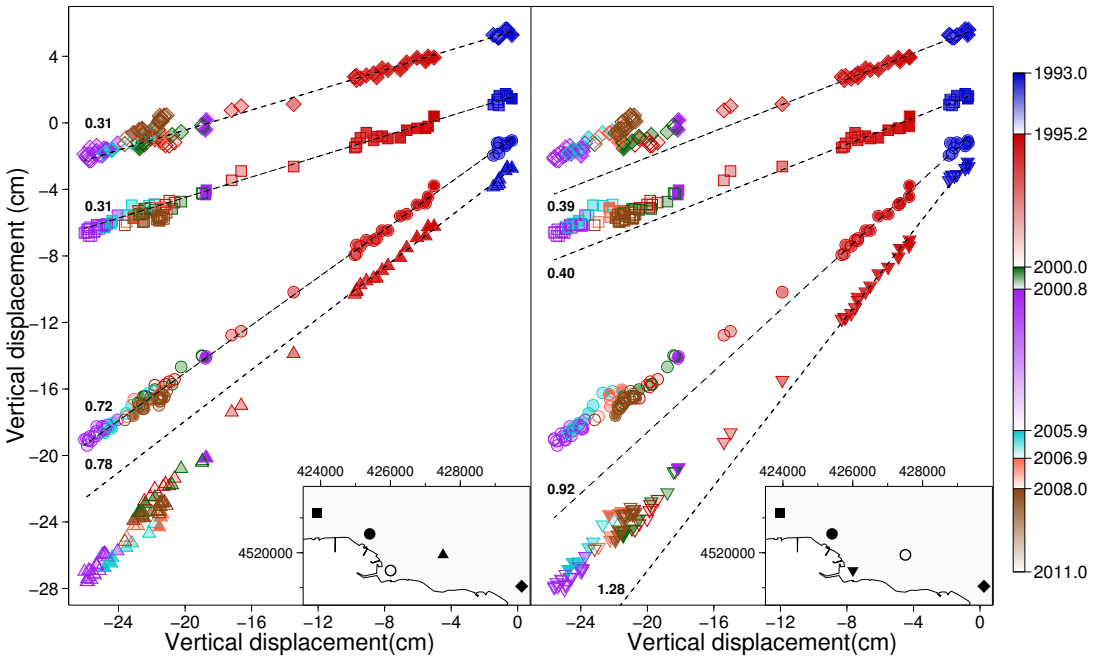


Figure 4.14: Correlation plots between vertical displacements. Left: local (filled symbols in the inset) vertical displacements vs reference area (empty circle in the inset) vertical displacements ; numbers indicate slopes of the dashed 1993-1997 regression lines. Right: local (filled symbols in the inset) vertical displacements vs solfatara (empty circle in the inset) vertical displacements; numbers indicate slopes of the dashed 1993-1997 regression lines. Colors give time (see scale on the right).

of the SAR reference area free in the regressions. Horizontal displacements from geodetic precise traversing are not used because of the lack of spatial and temporal continuity of the measurements. We use the data covariance matrix previously introduced for leveling benchmark uplifts and assign a constant uncertainty to SAR vertical and eastward displacements ( 0.5 cm and 1.4 cm respectively). Parameter uncertainties are estimated as usual in linear regressions *(Gubbins, 2004)*. Figure 4.15 shows the estimated time histories of $\Delta V_{\mathrm{PTE}}$, $\Delta V_{\mathrm{PS}}$ and the root-mean-square deviation of residuals (RMSD). RMSD is shown also for uplifts from leveling data, even if they are not independent, as intuitive goodness-of-fit indication. RMSD is fully consistent with data uncertainties for both leveling and SAR data. RMSD of SAR vertical and eastward displacements increases over time by about 0.5 mm/yr, in agreement with the non-measurement noise level in *(Pollitz et al., 1998)* and long-period noise levels in vertical motion obtained by *Wyatt, (1989)*.

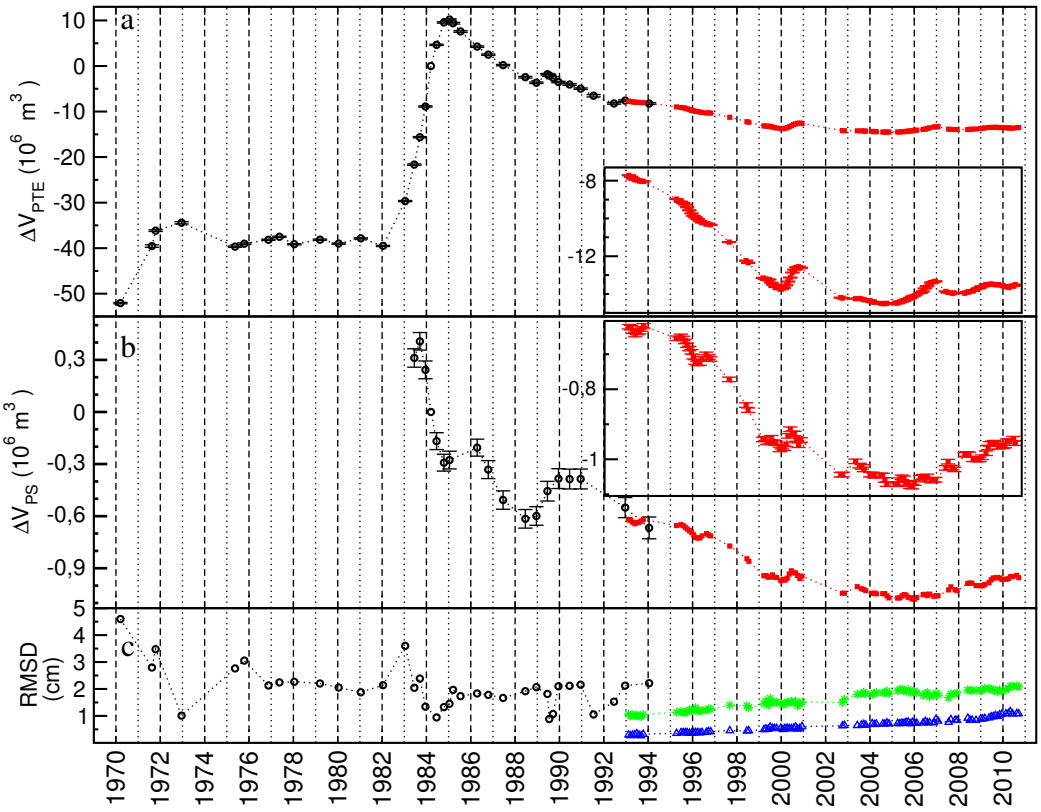


Figure 4.15: Time histories of (a) $\Delta V_{PTE}$ , (b) $\Delta V_{PS}$ , and (c) root-mean-square deviation of residuals (RMSD). Enlarged y-scales are used in the insets of panels (a) and (b). Volume changes of both sources are given with respect to March 1984. $\Delta V_{PS}$ is not given before June 1983 and for some other dates (e. g. July 1991 and June 1992) because of lack of leveling data in the Solfatara area. We show also RMSD of uplifts from leveling data, even if they are not independent, as intuitive goodness-of-fit indication. Open circles, results obtained from the inversion of leveling data; solid squares, results obtained from the inversion of SAR data (vertical and eastward displacements). Open triangles and stars (panels c) refer to SAR vertical and eastward displacements respectively.

These results refer to completely different settings, but long-period deformation noise seems almost site-independent *(Crescentini et al., 1997)*. Time histories of $\Delta V_{\mathrm{PTE}}$ and $\Delta V_{\mathrm{PS}}$ are similar, but some noticeable differences are visible, e. g. before January 1985 and after 2006. The 2006 mini-uplift, which is evident in $\Delta V_{\mathrm{PTE}}$ and in Figure 4.1, is absent in $\Delta V_{\mathrm{PS}}$. These differences support the existence of a genuine local deformation source at Solfatara against the emergence of a mere distortion of large-scale deformation, e. g. because of local rheology. The steep negative 1995-2006 trend of $\Delta V_{\mathrm{PS}}$ history in-

dicates relatively large deflation, superimposed by a small uplift (inflation) during 2000; slope seems slightly steeper before 2000 than after 2001. After 2006 slope is positive and almost constant. Annual oscillations are clearly visible.

To confirm the validity of this two-source model we choose seven representative grid nodes of CF and calculate the residuals, before subtracting, from the actual SAR vertical displacement, only the PTE effect and then the effect of the both sources (PTE and PS). Figure 4.16 shows vertical displacements, residuals with respect to PTE, and residuals with respect to the two-source model. Residuals with respect to PTE for grid nodes A,B,C and G are always almost null, but not residuals of grid nodes of Solfatara area D, E and F; in this case residuals with respect to PTE model present a further displacement, but are always almost null using the two-source model. This is true for the entire period of availability of SAR data.

To highlight any changes in the residuals, we have the residuals of vertical displacements computed with respect to February 1993 for the two-source model (PTE and PS) at four different dates (see figure 4.17). Snapshot (a) refers to the end of a major CF deflation phase (about 23 cm from February 1993); no particular feature is recognizable. After more than five years (snapshot b) the map is similar, but some positive and negative tilt-like vertical displacement is visible few kms SE and NW of the maximum uplift area. These features become more and more evident over time (snapshots c and d). However, displacement velocity is small (around 3 mm/yr) and further deeper investigation is needed to exclude SBAS-DInSAR processing artifacts and/or possible environmental causes. This particular feature is confirmed from figure 4.18. We have chosen two strips in the CF area (see figure 4.18) from west to east and have extracted the vertical and eastward displacements of the nodes of the grid contained in these strips, for four different periods rescaled to match the 1995-00 maximum uplift. The chosen periods (1995-00, 2000-01, 2005-07 and 2008-10) are all mini-uplift with constant ratio. We can note that the displacement in the period 2008-10 has a different pattern compared to those of other periods, with an uplift in the east part of the caldera, in the same zone where the positive tilt-like vertical displacement is visible in figure 4.17. So after 2008 the deformation pattern seems to be given by the combination of the "usual" pattern and an "anomalous" side uplift, whose origin is not clear.

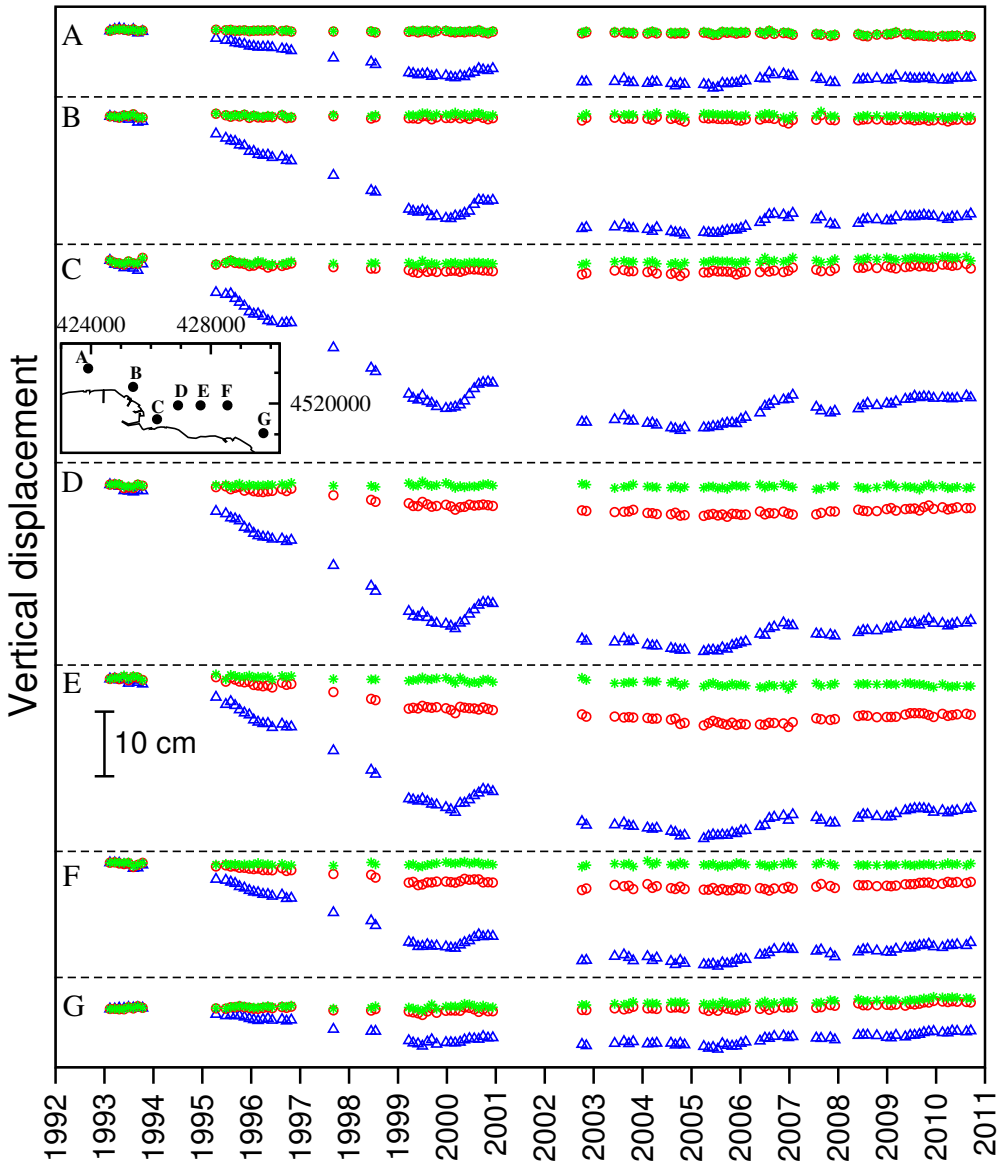


Figure 4.16: Vertical displacements (open blue triangles), residuals with respect to PTE (open red circles), and residuals with respect to the two-source model (PTE and PS, light green stars) from SAR data at seven grid nodes (see inset and Figure 4.3). Nodes D, E, and F are in the Solfatara area.

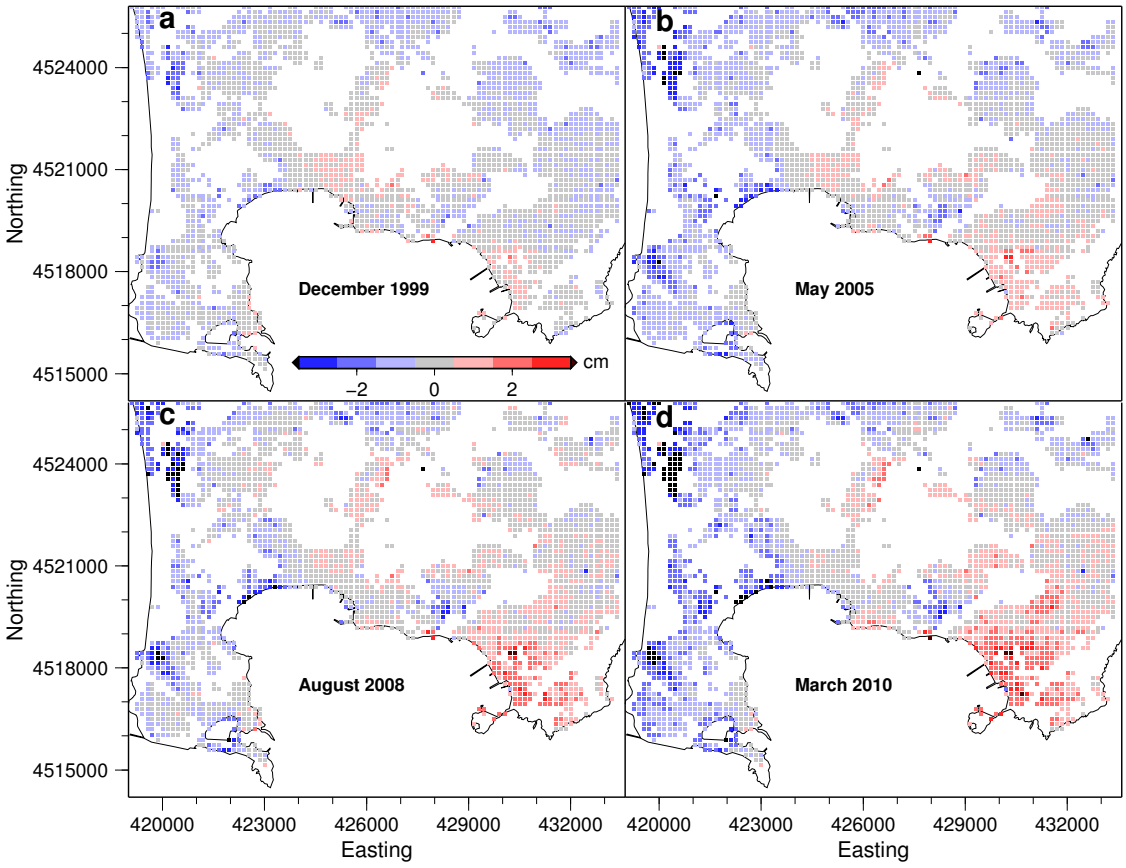


Figure 4.17: Snapshots of residuals of vertical displacements, computed with respect to February 1993, for the two-source model (PTE and PS) at four different dates.

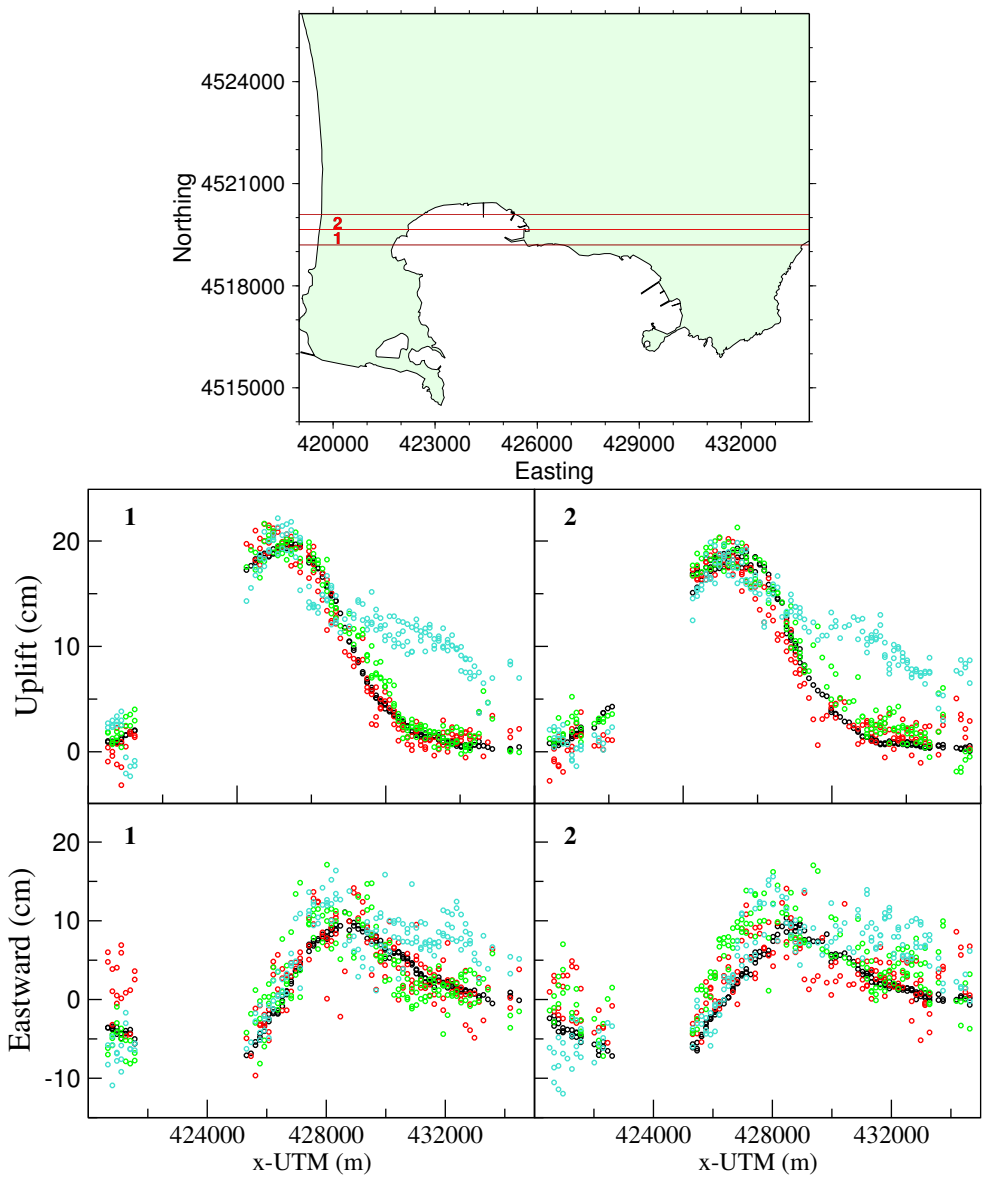


Figure 4.18: Selected strips in the CF caldera, from west to east (top). Vertical and eastward displacements in the two selected strips (Left: strip 1; right: strip 2). Black circles, 1995-00 (reversed in sign); red, 2000-01 (multiplied by 5.6); green, 2005-07 (multiplied by 5.9); turquoise, 2008-10 (multiplied by 7.2) (bottom).

# Chapter 5

# Recent bradyseisms: analysis of cGPS data

In the previous chapter, the period from 1980 to 2010 is analyzed using leveling, geodetic precising traversing and SAR data. In this chapter, the analyzed period is extended, until October 2013, using continuous Global Positioning System (cGPS) data. Our aim is confirmed, by cGPS data (that covered the period 2000-2013), the previous results.

## 5.1 Campi Flegrei stationary deformation pattern confirmed by GPS data

Different types of data have different peculiarities, for example, InSAR series give superficial displacement maps, but northward displacement is not resolved, accuracy is $\sim 1$ cm and lag between consecutive data is $\sim 1$ month. Leveling data provide only the vertical displacements and need to be coupled with horizontal displacements too. Continuous GPS stations, instead, have a worse spatial coverage than SAR or leveling, but the full displacement vector is resolved with an accuracy of weekly solutions of $\sim 1$ mm.
From 2008 to present a general uplift $\sim 16\,cm$ occurred and the displacement from 2008 to 2011 has a lower amplitude and average rate of uplift than the period from 2011 to present. The RITE GPS station is used as reference station because it is located in the area of maximum uplift, its acquisition started in 2000 and its vertical displacement is shown

in figure 5.1.

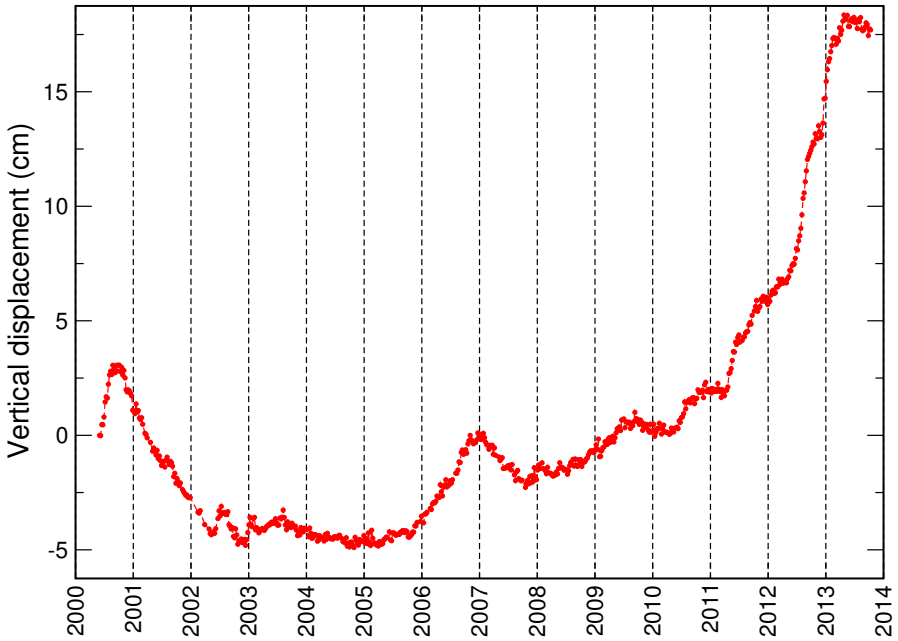


Figure 5.1: RITE station vertical displacement

The deformation field stationarity is evident in figure 5.2 by the comparison between the 1980-83 displacements of EDM benchmarks, with cGPS displacements of periods 2005.8-2007 and 2011.2-2013.3 (appropriately scaled). Although different EDM and cGPS benchmarks positions, the field seems to be the same. The anomalous trend of geodetic precise traversing benchmarks C (located at Nisida), already highlighted in the previous chapter by the comparison with SAR eastward displacement data, is also confirmed by the comparison with cGPS data.

## 5.2 New inversion for large scale deformation source with cGPS data

To confirm the proposed two-source model, we tried to find a source that gives a good simultaneous fit for all available data (leveling, geodetic precising traversing and cGPS). By ASA we invert leveling and precising traversing data as previously described, but joining

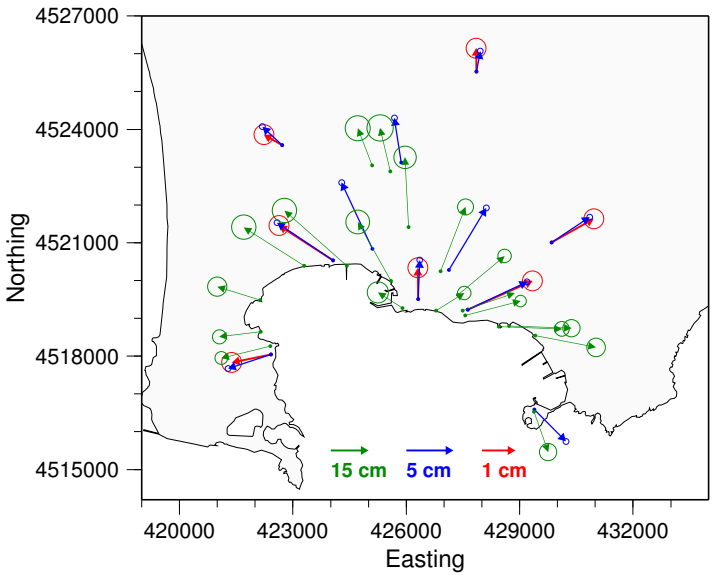


Figure 5.2: Positions and 1980-83 displacements of EDM benchmarks (green) compared with 2005.8-2007 GPS (red) and 2011-2013.3 GPS displacements (blue)

displacements cGPS data, for the period 2011-2013 (uplift period), scaled on 1980-83 displacement. To reduce noise, we estimate 2011 to 2013 cGPS displacements after smoothing displacement time series. The inverted data are shown in figure 5.3. The results confirm that the most likely single stationary source that satisfy large-scale CF deformation is an elongated quasi-horizontal crack at 3600m in depth, and oriented NW to SE. Fixing this source, whose volume change is left free in the inversion, we invert the data using a two-source model. The inversion results confirm, as second source, a small pressurized spheroid having vertical simmetry axis at 2000m depth;

As previously done we estimate the time histories of the two volume change, using the cGPS data to cover the period from 2000 to October 2013 (till cGPS data are available). From 2000 to 2010 there is an overlap period of SAR and cGPS data. RMSD of cGPS vertical, eastward and northward decreases over time until 2009 where an increases is present until the end. It is worth highlighting two important features, firstly the good agreement between SAR and cGPS time histories during overlap periods, secondly the noticeable differences between $\triangle V_{PTE}$ and $\triangle V_{PS}$ which are still visible and as a further support of the existence, of a real deformation source and not of a distortion of large-scale deformation . The most evidence discrepancy is after 2011, as it has been argued in the previously chapter, where $\triangle V_{PTE}$ has an evident uplift while $\triangle V_{PS}$ is almost constant from 2008. $\triangle V_{PS}$ is

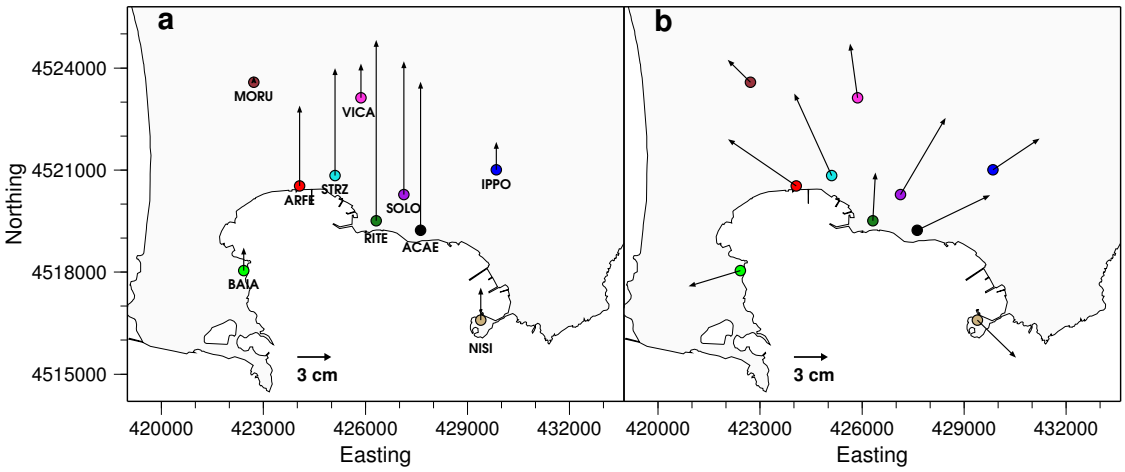


Figure 5.3: Maps of the Campi Flegrei caldera, cGPS stations (colored filled circles), and (a) vertical and (b) horizontal displacements of 2011.24–2013.27.

almost constant from in the period 2011-2013, or in other word, PS did not contribute to 2011-2013 deformation; on the contrary , PTE exhibits a noteworthy increase of activity.

## 5.3 cGPS residuals time series

This two-source model is used to calculate vertical, eastward and northward residuals of each station, when the effects of large-scale and local (Solfatara) deformation sources are removed. Figures 5.5, 5.6 and 5.7 show that residuals, with respect to the two-source model, are always almost null. For same stations a constant trend is evident, probably due to a local moving. So the introduction of cGPS data seems to confirm the two-source model. The most relevant station to highlight the necessity of a two-source model is the ACAE station, located in the south part of Solfatara. Because of its position, at this station, should be very evident the effect of both the sources, PTE and PS. Particularly the local deformation due to the Solfatara source should be evident in the station's northward displacement. In figure 5.8 the black line is the actual northward displacement at ACAE station and the red line represents residuals respect to PTE. The effects of another local source is clearly visible because an evident signal is still present, particularly from 2000 to 2008. This is in agreement with the time histories of PS volume change, indeed, a northward residual is present until 2006 (positive $\triangle V_{PS}$ ) and an opposite residual is present after 2006 (negative $\triangle V_{PS}$ ). The residuals with respect to the two-source model,

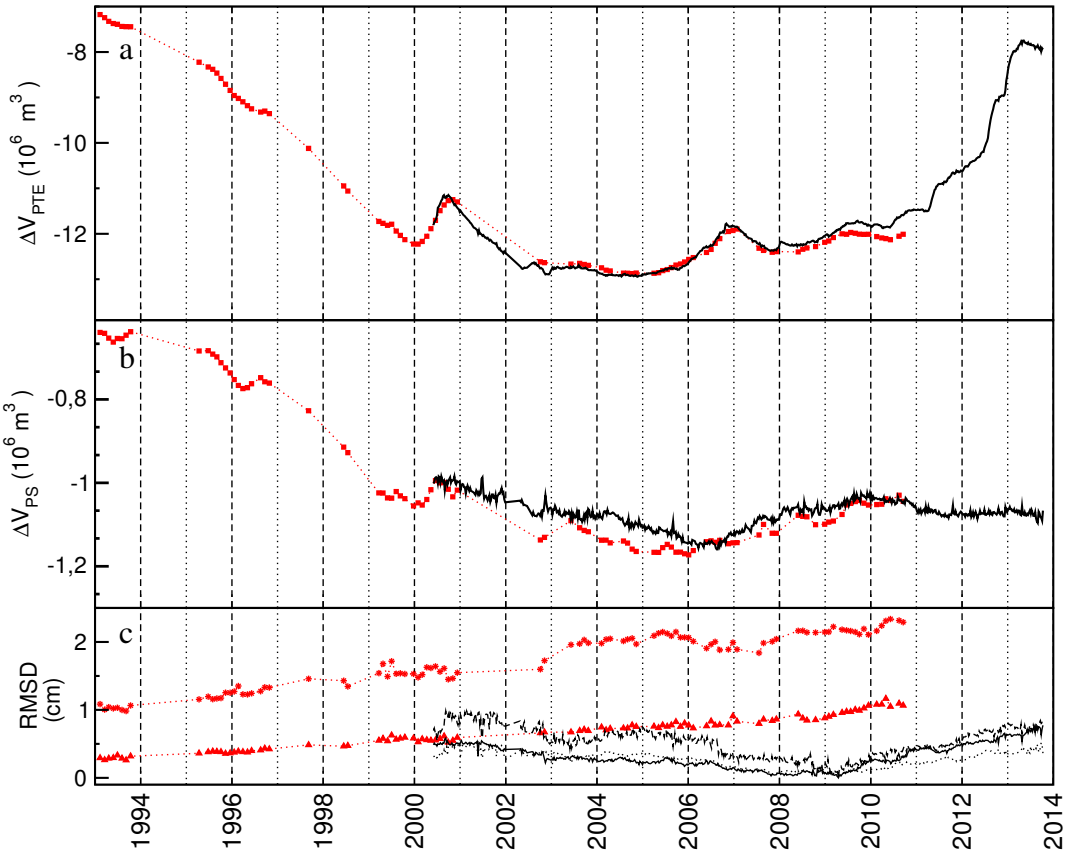


Figure 5.4: Time histories of (a) $\triangle V_{PTE}$ and (b) $\triangle V_{PS}$ and (c) root-mean-square deviation of residuals (as just seen in fig4.15). Red solid squares results obtaines from the inversion of SAR data. Black lines are from the inversion of GPS data. Red stars and triangle refer to SAR eastward andvertical while dashed, pointed, and solid lines refer to SAR vertical, eastward and northward respectively.

the green line, are almost null. To highlight any strange behaviors of the area, by best fit lines on the residuals time histories shown in figures 5.5, 5.6 and 5.7, residual vertical and horizontal velocities are calculated as shown in figure 5.9 .

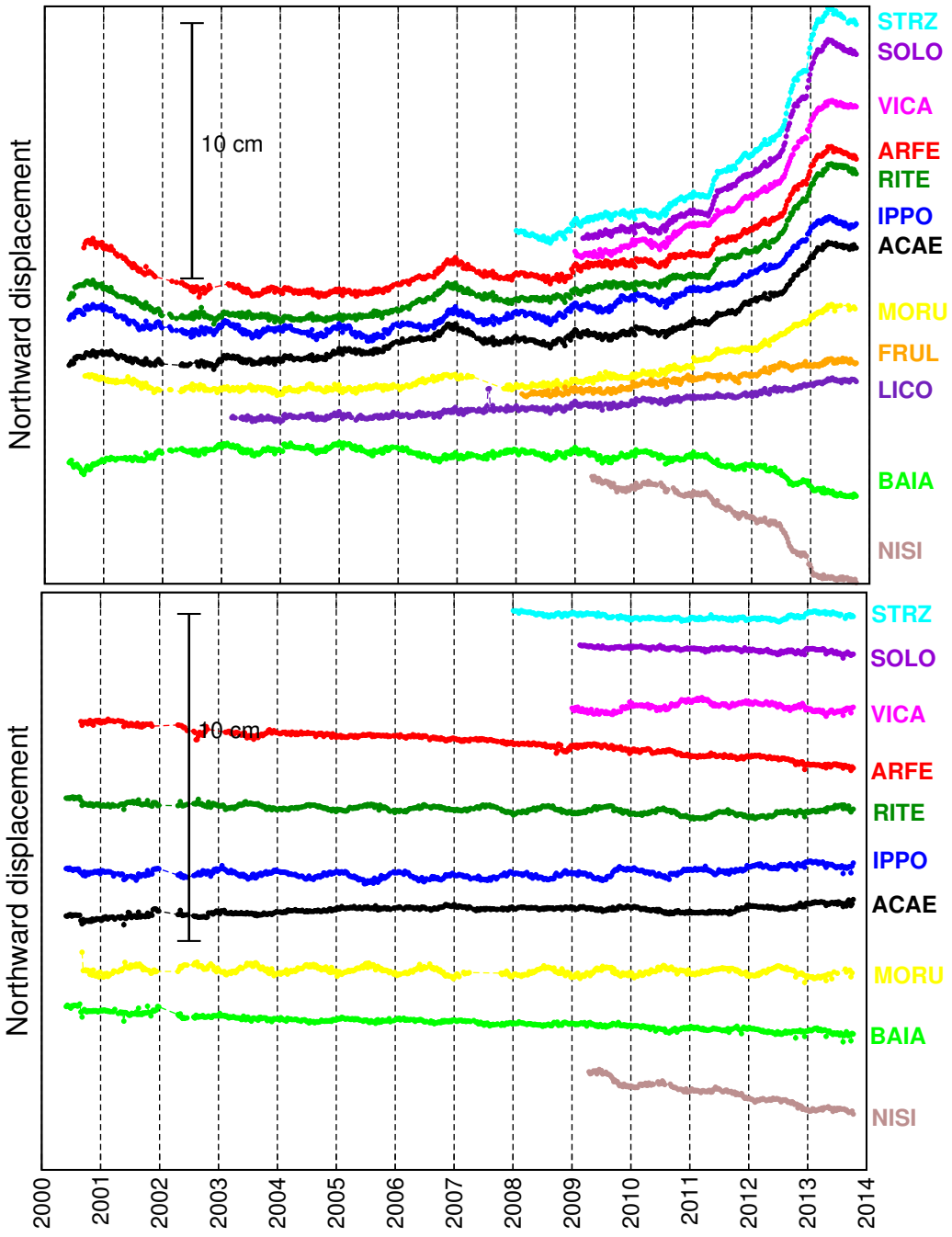


Figure 5.5: Top: Time northward displacement. Bottom: Residuals displacements, effects of large-scale and local (Solfatara) deformation sources is removed. Residuals of FRUL and LICO stations are not shown because they are not affected by the PTE or PS.

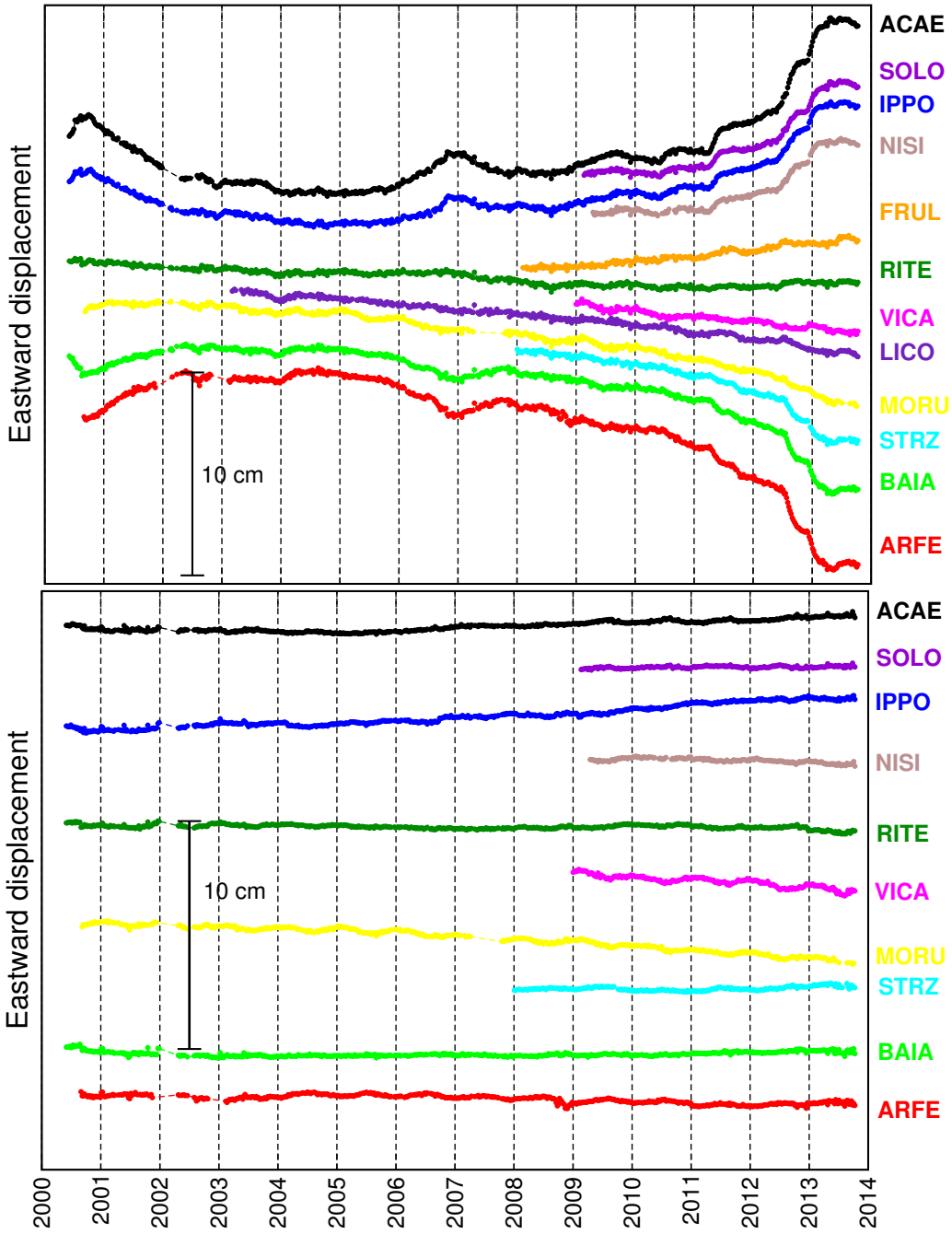


Figure 5.6: Top: Time eastward displacement. Bottom: Eastward residuals displacements, effects of large-scale and local (Solfatara) deformation sources is removed. Residuals of FRUL and LICO stations are not shown because they are not affected by the PTE or PS

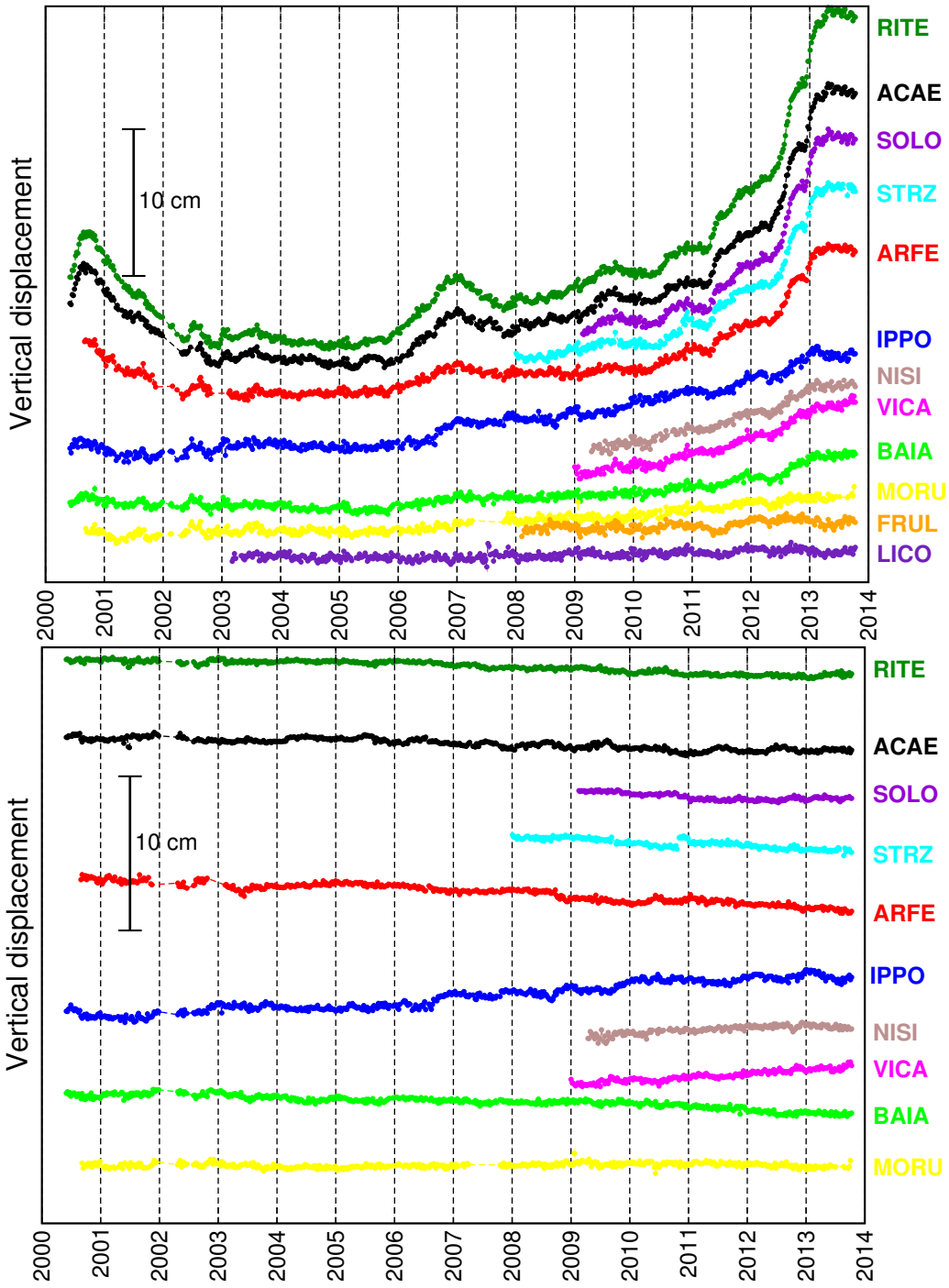


Figure 5.7: Top: Time vertical displacement. Bottom: Vertical residuals displacements, effects of large-scale and local (Solfatara) deformation sources is removed. Residuals of FRUL and LICO stations are not shown because they are not affected by the PTE or PS

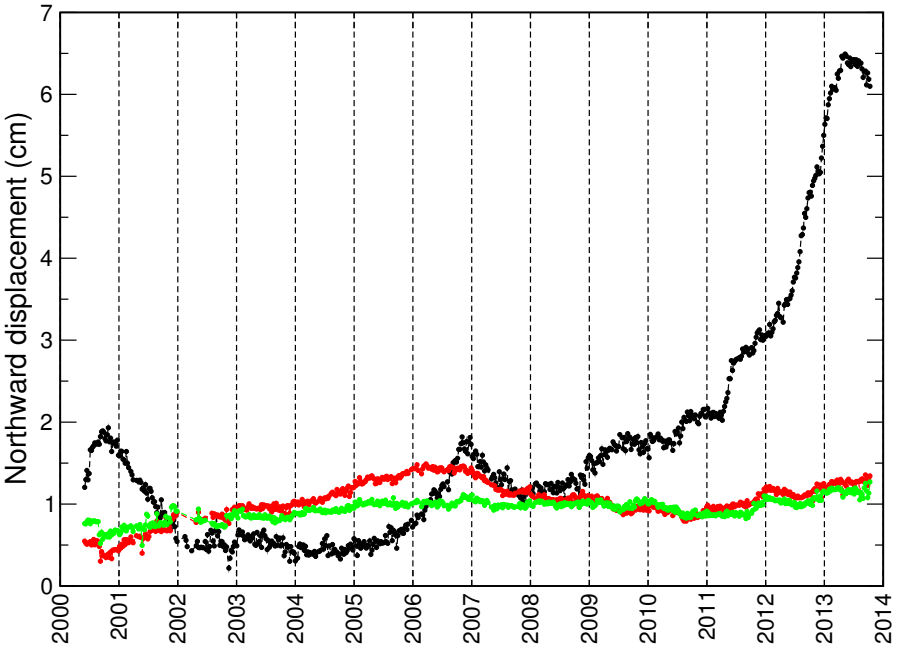


Figure 5.8: Actual northward displacement at ACAE station (black line), residuals respect to PTE (red line) and residuals with respect to the two-source model (green line).

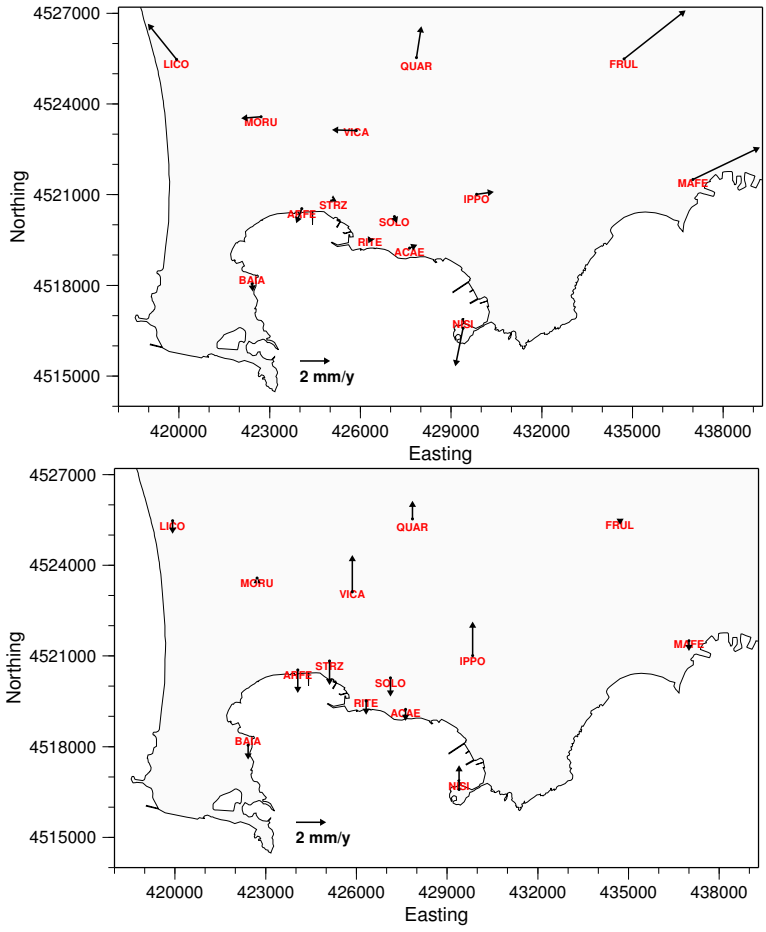


Figure 5.9: Horizontal (top) and vertical (bottom) residuals velocities

# Chapter 6

# Conclusions

The aim of this thesis is not to investigate the real causes of the Campi Flegrei deformation pattern (magma or fluid injections) but to provide a model that is compatible with the data and allows to exclude some scenarios that are not compatible with a deformation pattern that is constant during both inflation and deflation phases. In chapter 4 it has been shown that CF deformation pattern is stationary for all analyzed periods with large-signal and constant ratio (March 1970 - May 1975; June 1980 - June 1983; June 1983 - October 1984; January 1985 - December 1988; June 1989 - December 1992; March 1995 - end 1999), with the exception of the Solfatara area, so we inverted 1980-83 ground deformation data (because of the large signal $\sim 60\,cm$) for a single source, testing the whole ensemble of sources used in the literature and two additional ones (finite spheroid and finite triaxial ellipsoid).

This 1980-83 source, with time-dependent potency, satisfies large-scale CF deformation from 1980 to 2010 and residual deformation is confined to the Solfatara fumarolic field and can be described by a shallow small source, whose potency changes over time. These simple stationary sources are enough to solve the whole CF deformation pattern. The term "stationary" means that each of the two parts evolves over time through a mere scaling factor, given by the potency (strength) of the related source.

Firstly we inverted, in a layered media, leveling, geodetic precise traversing and SAR (appropriately scaled) data to investigate the period 1980-2010. The most likely single stationary source that satisfies large-scale deformation during the whole investigated period is an elongated quasi-horizontal crack embedded in an elastic layered medium at $\approx 3600$

m in depth, and oriented NW to SE. The source is schematized as a pressurized triaxial ellipsoid (PTE) or, equivalently, as a stationary tensile fault (TF), infact only source potency changes over time.
The other tested models (point spheroidal cavity, horizontal circular crack, finite spheroidal cavity, moment tensor) are unfavored. Subtracting this source contribution to the 1995-2000 sperimental SAR data, the residual deformation is confined to the area of the Solfatara fumarolic field. Fixing the first PTE source, whose volume change has been left free in the inversion, we inverted the data using a two-source model.
The second source of this model is a small spheroid (PS) located beneath Solfatara, at about 1900 m in depth. Again, all source parameters but potency has been considered constant over time. An important aspect of this thesis is that the two-source model is obtained by inversion in a layered media.
The importance of taking into account the stratification is evidenced by different authors (*Amoruso, Crescentini and Fidani, 2004; Amoruso and Crescentini, 2007; etc)*. In this thesis, the layered model is based on seismically derived estimates of the P wave speed for the crust in the CF area. It is a first-order approximation of the real CF heterogeneities and permits to invert displacement data for finite sources, which are much favored with respect to point sources.
We tested other elastic layered media and found that source depth depends on layering details and can change up to about 200 m.
Volume change is more robust, in agreement with as been found by *Amoruso et al. (2004)* for fault depth and seismic potency. Subsequently, using cGPS data, the analyzed period was extended until October 2013. The cGPS stations, used in this thesis, are only twelve but they are well distributed over all the CF area. cGPS data confirm that the CF deformation field is still constant and a new inversion has been done using 1980-1983 leveling data and geodetic precising traversing data joined to displacements cGPS data, for the period 2011-2013 (uplift period $\sim$ 16 cm), scaled on 1980-83 displacement. The inversion results confirm that the most likely single stationary source, that satisfy large-scale CF deformation, is an elongated quasi-horizontal crack at 3600 m in depth, and oriented NW to SE.
Fixing this source, whose volume change is left free in the inversion, we inverted the data using the previous two-source model. The inversion results confirm, as second source, a small pressurized spheroid having vertical symmetric axis at 2000m depth. The residual displacements, for each stations, with respect to the two-source model are almost null.

The necessity of a two-source model is highlighted by ACAE station, indeed, because of its position at the South of Solfatara, this station is well affected by the presence of both sources. The local deformation due to Solfatara source is evident in the station northward displacement, after removing the effects of the PTE source.
Residual deformation (without PTE), on the ACAE station, is also well compatible with the history of the Solfatara source potency.
Recent studies proposed multiple sources with different features acting in different periods *(Gottsmann et al., 2006b)*, fluid injections implying large changes of the large-scale deformation pattern over time *(Troiano et al., 2011)*, complex spatial and temporal patterns of distributions of volumetric sources *(D'Auria et al., 2012)* but those scenarios are not compatible with the result of this thesis of a CF deformation pattern that can be decomposed into two stationary parts.
The Solfatara source potency history is somewhat similar to the one of the source of large-scale CF deformation, but the two sources are not synchronous (Figure 4.15).
These differences support the existence of a genuine local deformation source at Solfatara against the emergence of a mere distortion of large-scale deformation, e. g. because of local rheology. Moreover, inverting CF superficial displacements related to different periods for single sources may lead to different models. Even if leveling data from January 1994 to March 1995 ($\approx$ 4 cm mini-uplift and subsequent recovery) and from January 2001 to October 2002 ($\approx$ 5 cm deflation following the 2000 mini-uplift) are not accessible to us, our findings may be reasonably extended to these missing periods.
A similar source azimuth was found by *Dvorak and Berrino (1991)* for 1980-83 and *Lundgren et al. (2001)* for 1993-98. The best-fit 1980-83 source in *Dvorak and Berrino (1991)* is a tensile fault which is similar to TF here, apart from depth. The depth difference is not surprising, because of the so-called "focussing effect" which arises when a homogeneous half space is used *(Amoruso et al., 2004)*.
Our large-scale deformation source is in agreement with the possible presence of a small melt volume – located below the maximum uplift area of the major 1982-1984 unrest between 3000 m and 4000 m in depth – recently evidenced by seismic attenuation imaging (*DeSiena et al., 2010)* as shown in figure 6.1.

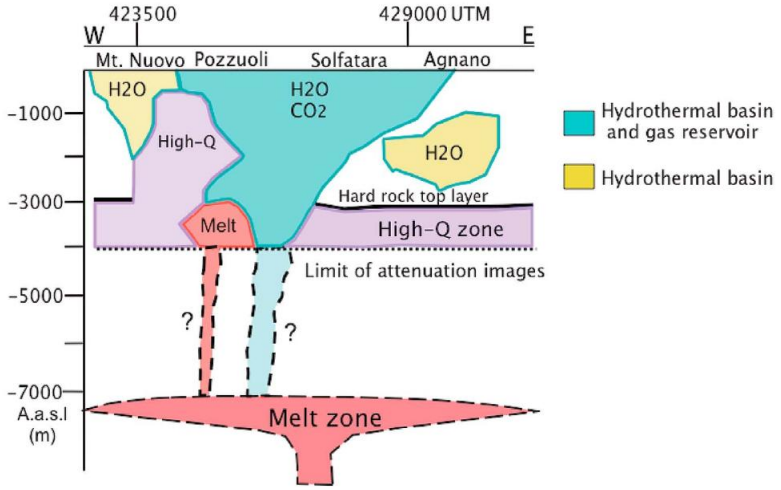


Figure 6.1: Schematic illustration of the uppermost crust crossing Campi Flegrei from West to East. From *DeSiena et al., 2010.*

The Solfatara deformation source is consistent with the Solfatara geochemical conceptual model *(Chiodini et al. [2010, 2013*]) and related vertical displacements *(Rinaldi et al., 2010)*. According to *Chiodini et al., [2010, 2013*], a plume of vapor-liquid biphase zones and single vapor zones is fed by a mixture of magmatic and meteoric fluids. The magmatic component enters the base of the system at about 2000 m in depth, where it mixes with and vaporizes the liquid of meteoric origin. Hydrothermal fluids play a role, in the ground deformation, due to thermal expansion and pore pressure acting on rocks. *Rinaldi et al. (2010)* simulated the heat and fluid flow driven by the arrival of magmatic fluids from greater depth and calculate the rock deformation arising from simulated pressure and temperature changes within a shallow hydrothermal system. We employ a mathematical model, based on the linear theory of thermo-poro-elasticity and on a system of distributed equivalent forces. Results show that stronger degassing of a magmatic source may cause several centimeters of uplift *(Rinaldi et al., 2010*). *Fournier and chardot (2012)* have recently shown that, when ground deformation is related to hydrothermal processes and satisfied by simple point or finite sources, ground deformation is likely to be controlled by the poroelastic response of the substratum to pore-pressure increase near the injection point of hot magmatic fluids into the hydrothermal system.

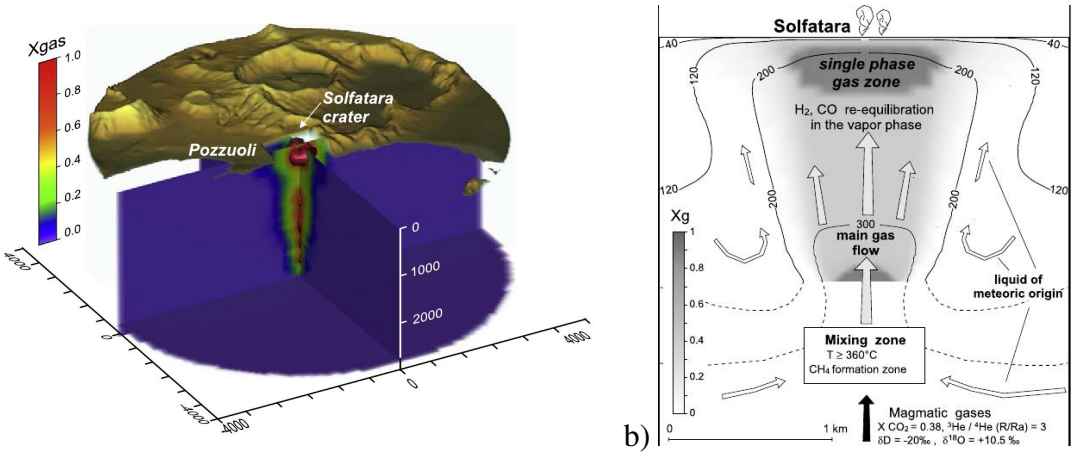


Figure 6.2: a) This figure shows the gas saturated area (red color) between 100 and 250 m of depth underneath the Solfatara crater. A deeper spindle shaped saturated area appears, between 2600 and 1000 m of depth. From *Chiodini et al., 2013* b) Geochemical conceptual model of Solfatara from *Chiodini et al., 2010*

The retrieved source depth points to that of the injection area. As regards geochemical data at Solfatara, the fumarolic $CO_2/H_2O$ ratio shows a mild increasing trend after 2000; this change has been interpreted as the effect of an increased contribution of the magmatic component in the fumarolic fluids *(Chiodini et al., 2012)*. A sharp increase of the $CO_2/H_2O$ ratio overlaps the trend during 2007. Also the partial pressure of $CO_2$ (estimated on the basis of fumarolic compositions and on the assumption of thermodynamic equilibrium within the $H_2O - H_2 - CO_2 - CO$ gas system) starts to increase after 2000 with an evident jump in 2006. The same distinct periods (before 2000, 2000 to 2006, after 2006-2007) are evident in the time history of $\Delta V_{PS}$ (Figure 6.3). Obviously, potency changes of the large-scale deformation source and/or the Solfatara one could be driven by magma and/or magmatic fluids fed by a deeper ($\approx$ 7500 m) magma chamber *(Zollo et al., 2008)*. In principle, migration of magma and/or magmatic fluids from the deeper magma chamber should give its own deformation signal.

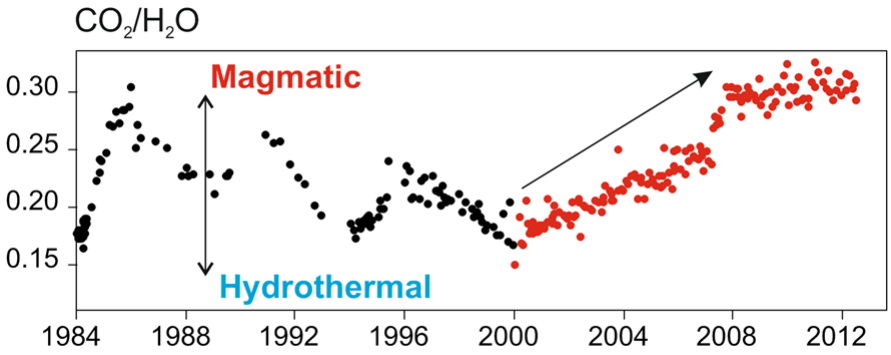


Figure 6.3: Time histories changes in the chemical composition of the fumaroles of Solfatara $CO_2/H_2O$. Since 2000, the fumaroles of Solfatara were progressively enriched in the magmatic contribution. (Figure from http://www.ov.ingv.it/ov/it/campi-flegrei.html)

# Bibliography


[1] AGIP, *Modello geotermico del sistema flegreo (Sintesi)*. Technical Report, SERGMESG, San Donato, Italy, 1987.

[2] AKAIKE H., *Information theory and an extension of the maximum likelihood principle*. Second international symposium on information theory (pp. 267281). Budapest: Academiai Kiado, 1973.

[3] AKI K. and RICHARDS P. G., *Quantitative seismology*. Second edition, University Science Books, Mill Valley, 2009.

[4] AKIMA H., *On estimating partial derivatives for bivariate interpolation of scattered data*. Rocky Mountain J. Math., 14, 41–52, 1984.

[5] AMORUSO A. CRESCENTINI L., and FIDANI C., *Effects of crustal layering on source parameter inversion from coseismic geodetic data*. Geophys. J. Int., 159, 353–364, doi: 10.1111/j.1365-246X.2004.02389.x, 2004.

[6] AMORUSO A., CRESCENTINI L., LINDE A. T. , SACKS I.S., SCARPA R. and ROMANO P., *A horizontal crack in layered structure satisfies deformation for the 2004-2006 uplift of Campi Flegrei*. Geophysical Research Letters, Vol. 34, L22313, 2007.

[7] AMORUSO A. CRESCENTINI L., *Inversion of leveling data: how important is error treatment?*. Geophys. J. Int., 171, 1352–1362. doi: 10.1111/j.1365-246X.2007.03585.x, 2007.

[8] AMORUSO A. , CRESCENTINI L. and BERRINO G., *Simultaneous inversion of deformation and gravity changes in a horizontally layered half-space: evidences for magma intrusion during the 1982-1984 unrest at Campi Flegrei Caldera (Italy).* Earth and Planetary Science Letters, 2008.

[9] AMORUSO A. , CRESCENTINI L., *Shape and volume change of pressurized ellipsoidal cavities from deformation and seismic data.* Journal of geophysical research,Vol.114, 2009.

[10] AMORUSO A., and CRESCENTINI L., *Modelling deformation due to a pressurized ellipsoidal cavity, with reference to the Campi Flegrei caldera, Italy* . Geophys. Res. Lett., 38, L01303, doi:10.1029/2010GL046030, 2011.

[11] AMORUSO A. and CRESCENTINI L., *Analytical models of volcanic ellipsoidal expansion sources*. Annals of Geophysics, 56, S0435, doi:10.4401/ag-6441L01303, 2013.

[12] AMORUSO A., CRESCENTINI L., SABBETTA I., *Paired deformation sources of the Campi Flegrei caldera (Italy) required by recent (1980–2010) deformation history.* Journal of Geophysical Research: Solid Earth , DOI: 10.1002/2013JB010392, 2014.

[13] ARIENZO A., MORETTI R., CIVETTA L., ORSI G., PAPALE P., *The feeding system of Agnano–Monte Spina eruption (Campi Flegrei, Italy): Dragging the past into present activity and future scenarios*. Chemical Geology 270, 135–147, 2010.

[14] BARBARELLA M., GUBELLINI A., and RUSSO P., *Rilievo ed analisi dei recenti movimenti orizzontali del suolo nell'area flegrea*. Atti 2° Convegno GNGTS, Rome, Italy, 12–14 December, 1983.

[15] BATTAGLIA M., TROISE C., OBRIZZO F., PINGUE F., and DE NATALE G., *Evidence for fluid migration as the source of deformation at Campi Flegrei caldera (Italy).* Geophysical Research Letters, vol. 33, L01307, doi:10.1029/2005GL024904, 2006.

[16] BEAUDUCEL F., DE NATALE G., OBRIZZO F. PINGUE F., *3-D Modelling of Campi Flegrei Ground Deformations: Role of Caldera Boundary Discontinuities.* Pure Appl. Geo- 683 phys., 161, 1329–1344, 2004.

[17] BERRINO G., CORRADO G., LUONGO G., TORO B. *Ground deformation and gravity changes accompanying the Pozzuoli uplift* . Bulletin Volcanologique 47, 187–200, 1984.

[18] BOTTIGLIERI M., FALANGA M., TAMMARO U., DE MARTINO P., OBRIZZO F., GODANO C. and PINGUE F., *Characterization of GPS time series at the Neapolitan volcanic area by statistical analysis.* Journal of Geophysical Research, VOL. 115, B10416, doi:10.1029/2009JB006594, 2010.

[19] BURNHAM K. P. and ANDERSON D. R., *Multimodel Inference: Understanding AIC and BIC in Model Selection*. Sociological Methods Research, 33, 261–304, 2004.

[20] CASU, F., MANZO M., and LANARI R., *A quantitative assessment of the SBAS algorithm performance for surface deformation retrieval from DInSAR data*. Remote Sens. Environ., 102, 195 – 210, doi:10.1016/ j.rse.2006.01.023, 2006.

[21] CATALLI F., *Sorgenti sismiche: Rappresentazione matematica ed applicazione al calcolo degli spostamenti.* Quaderni di Geofisica (INGV), 2007.

[22] CHIODINI G., CALIRO S., CARDELLINI C., GRANIERI D., AVINO R., BALDINI A., DONNINI M., AND MINOPOLI C., *Longterm variations of the Campi Flegrei, Italy, volcanic system as revealed by the monitoring of hydrothermal activity*. J. Geophys. Res., 115, B03205, doi: 10.1029/2008JB006258., 2010.

[23] CHIODINI G., CALIRO S., DE MARTINO P., AVINO R., GHERARDI F., *Early signals of new volcanic unrest at Campi Flegrei caldera? Insights from geochemical data and physical simulations*. Geology, 40, 943–946, doi:10.1130/G33251.1., 2012.

[24] CRESCENTINI L., AMORUSO A., FIOCCO G. and VISCONTI G., *Installation of a high-sensitivity laser strainmeter in a tunnel in central Italy*, Rev. Sci. Instrum., 68, 3206– 3210, 1997.

[25] CRESCENTINI L. AMORUSO A., CARPENTIERI M., *ANGELA: a new package for the near-real-time inversion of geodetic data in layered media*, in Marzocchi W., Zollo A.(Eds.) "Conception, verification, and application of innovative techniques to study active volcanoes". ISBN: 978-88-89972-09-0, 2007.

[26] CRESCENTINI L., AMORUSO A., *Effects of crustal layering on the inversion of deformation and gravity data in volcanic areas: An application to the Campi Flegrei caldera, Italy.* Geophysical Research Letters , Vol. 34, L09303, 2007.

[27] D'AURIA L. GIUDICEPIETRO F., AQUINO I., BORRIELLO, G., DEL GAUDIO C., LO BASCIO D., MARTINI M., RICCIARDI P., RICCIOLINO P., and RICCO C. *Repeated fluid-transfer episodes as a mechanism for the recent dynamics of Campi Flegrei caldera (1989–2010)*. J. Geophys. Res., 116, B04313, doi:10.1029/2010JB007837, 2011

[28] D'AURIA L. GIUDICEPIETRO F., MARTINI M. , AND LANARI R., *The 4D imaging of the source of ground deformation at Campi Flegrei caldera (southern Italy)*. J. Geophys. Res., 117, B08209, doi:10.1029/2012JB009181, 2012.

[29] DAVIS P.M. *Surface deformation due to inflation of an arbitrarily oriented triaxial ellipsoidal cavity in an elastic half-space, with reference to Kilauea Volcano, Hawaii,* Journal of Geophysical Research, Vol.91, No.B7, 1986.

[30] DEL GAUDIO C., AQUINO I., RICCO C., SERIO, C., *Monitoraggio Geodetico dell'Area Vulcanica Napoletana: Risultati della Livellazione Geometrica di Precisione Eseguita ai Campi Flegrei a Settembre 2008*. Quaderni di Geofisica, 2009.

[31] DEMARTINO P., TAMMARO U. and OBRIZZO F., *GPS Time Series at Campi Flegrei Caldera (2000-2013)*. Annals of Geophys, (in press).

[32] DE NATALE G. , MASTROLORENZO G., PINGUE F., SCARPA R., *I Campi Flegrei e i fenomeni bradisismici*. Le Scienze n° 306, febbraio 1994.

[33] DE NATALE G. MASTROLORENZO G., PINGUE F., TROISE C.,PAPPALARDO L., BATTAGLIA M. BOSCHI E., *The Campi Flegrei Caldera: unrest mechanism and hazards*, Geological Society of London, Special Publications, 269, 25-45, 2006.

[34] DE SIENA L., DEL PEZZO E., and BIANCO F., *Seismic attenuation imaging of Campi Flegrei: Evidence of gas reservoirs, hydrothermal basins, and feeding systems*. J. Geophys. Res., 115, B09312, doi:10.1029/2009JB006938, 2010.

[35] DIETERICH J. H., and DECKER R. W., *Finite element modeling of surface deformation associated with volcanism*. J. Geophys. Res., 80, 4094–4102, 1975.

[36] D'ORIANO, C., POGGIANTI, E.,BERTAGNINI, A., CIONI, R., LANDI, P., POLACCI, M., ROSI, M.*, Changes in eruptive style during the A.D. 1538 Monte Nuovo eruption (Phlegrean Fields, Italy): the role of syneruptive crystallization*. Bull Volcanol 67, 7: 601-621, 2005.

[37] DVORAK J. J. and BERRINO G., *Recent ground movement and seismic activity in Campi Flegrei, southern Italy, epi- sodic growth of a resurgent dome*. J. Geophys. Res., 96, 2309-2323, 1991.

[38] ESHELBY J. D., *The determination of the elastic field of an ellipsoidal inclusion, and related problems.* Proc.R.Soc.London,Ser.A,241,376-396, 1957.

[39] FIALKO Y., KHAZAN Y. and SIMONS M., *Deformation due to a pressurized horizontal circular crack in an elastic half-space, with applications to volcano geodesy*. Geophys. J. Int. 146, 181–190, 2001.

[40] FOURNIER N., and CHARDOT L., *Understanding volcano hydrothermal unrest from geodetic observations: Insights from numerical modeling and application to White Island volcano, New Zealand*. J. Geophys. Res., 117, B11208, doi:10.1029/2012JB009469, 2012.

[41] GHILANI C. D., and WOLF P. R., *Elementary surveying – An introduction to geomatics*. 13th ed., Prentice Hall, Boston, 2012.

[42] GOLDSTEIN H.,POOLE C. P. and SAFKO J. L., *Classical Mechanics*. 3rd ed., Addison- Wesley, San Francisco, 2001.

[43] GOTTSMANN J., RYMER H. and BERRINO G., *Caldera unrest at the Campi Flegrei: A critical evaluation of source parameters from geodetic data inversion*. J. Volcanol. Geotherm. Res., 150, 132–145, doi:10.1016/j.jvolgeores.2005.07.002, 2006.

[44] GOTTSMANN J., CAMACHO A. G. , TIAMPO K. F. and FERNÀNDEZ J. *Spatiotemporal variations in vertical gravity gradients at the Campi Flegrei caldera (Italy): a case for source multiplicity during unrest?*. Geophys. J. Int. 167, 1089–1096, 2006.

[45] GUBBINS D. *Time series analysis and inverse theory for geophysicists*. Cambridge University Press, Cambridge, 2004.

[46] INGBER, L. *Adaptive Simulated Annealing (ASA).* Lester Ingber Research, 1993.

[47] JUDENHERC S., and ZOLLO A., *The Bay of naples (southern Italy): Constraints on the volcanic structures inferred from a dense seismic survey.* J. Geophys. Res. , 109 , B10312, doi:10.1029/2003JB002876, 2004.

[48] LUDWIG W. J., NAFE J. E., and DRAKE C. L., *Seismic refraction*, in The Sea, vol. 4, edited by A. E. Maxwell, pp. 53–84, Wiley-Interscience, New York, 1970.

[49] LUGLI A., *Interferometria SAR per lo studio di movimenti e generazione di modelli digitali del terreno in Antartide*. Tesi di dottorato, Università di Bologna, Italia, 2010

[50] LUNDGREEN P., USAI S., SANSOSTI E., LANARI R., TESAURO M., FORNARO G., BERARDINO P., *Modeling surface deformation observedwith syntheticaperture radar interferometry at Campi Flegrei caldera.* Journal of gheophysical research, VOL. 106, NO. B9, PAGES 19,355-19,366, 2001.

[51] MANCONI A,WALTER T.,MANZO M,ZENI G.,TIZZANI P.,SANSOSTI E., LANARI R., *On the effects of 3-D mechanical heterogeneities at Campi Flegrei caldera*. *Southern Italy* ,Journal of Geophysical Research., 115, B08405, doi:10.1029/2009JB007099, 2010

[52] MASSIRONI M*., Il Telerilevamento Satellitare.* Appunti per lezioni, Università di Padova, 2004

[53] MCQUARRIE D. R., TSAI C., *Regression and time series model selection*. World Scientific Publishing Co.Pte.Ltd., 1998

[54] MINDLIN, R.D., *Force at a point in the interior of a semi-infinite solid*. Physics,7,195-202,1936.

[55] MOGI K., *Relations between the eruptions of various volcanoes and the deformations of the ground surfaces around them*. Bull. Earthquake. Res. Inst. , 36 , 99-134, 1958.

[56] ORSI, G., PIOCHI, M., CAMPAJOLA, L., D'ONOFRIO, A., GIALANELLA, L., TERRASI, F., *Geochronological constraints for the volcanic history of the island of Ischia (Italy) over the last 5,000 years*. J. Volcanol. Geotherm. Res., 71, 249-257, 1996.

[57] Okada Y., *Surface deformation due to shear and tensile faults in a half-space*. Bull. Seismol. Soc. Am., 75, 1135–1154, 1985.

[58] OKADA Y., *Internal deformation due to a shear and tensile faults in a half space.* Bullettin of Seismology of America*,* Vol.82, No.2, 1992.

[59] PARASCANDOLA A., *I fenomeni bradisismici del Serapeo di Pozzuoli*. Guida, 1947.

[60] POLLITZ F. F.,URGMANN R. B. and SEGALL P., *Joint estimation of afterslip rate and postseismic relaxation following the 1989 Loma Prieta earthquake*. J. Geophys. Res., 103, 26975–26992, 1998.

[61] RENKA R., *Algorithm 660, QSHEP2D, Quadratic Shepard method for bivariate interpolation of scattered data*. ACM Trans. Math. Softw., 14, 149–150, doi: 10.1145/45054.356231, 1988.

[62] RINALDI A. P., TODESCO M. and BONAFEDE M., *Hydrothermal instability and ground displacement at the Campi Flegrei caldera*. Phys. Earth Planet. Inter., 178, 155–161, doi:10.1016/j.pepi.2009.09.005, 2010.

[63] ROTHMAN D. H., *Nonlinear inversion, statistical mechanics, and residual statics estimation*. Geophysics, 50, 2784-2796, 1985.

[64] ROTHMAN, D. H., *Automatic estimation of large residual statics corrections*. Geophysics, 51. 332-346, 1986.

[65] SAMBRIDGE M., *Geophysical Inversion with a Neighbourhood Algorithm -I. Searching a parameter space*. Geophys. J. Int., 138, 479–494, 1999.

[66] SAMBRIDGE M., *Geophysical Inversion with a Neighbourhood Algorithm -II. Appraising the ensemble*. Geophys. J. Int., 138, 727–746, 1999.

[67] SAMBRIGDGE M., MOSEGAARD K., *Monte Carlo methods in geophysical inverse*. Reviews of Geophysics, 2002.

[68] SEGALL P., *Earthquake and Volcano Deformation*. Princeton University Press, 2010.

[69] STACEY F. D. and DAVIS P. M., *Physics of the Earth*. Cambridge University Press, 2008.

[70] TRASATTI E., BONAFEDE M., FERRARI C., GIUNCHI C., BERRINO G., *On deformation sources in volcanic areas: Modeling the Campi Flegrei (Italy) 1982–84 unrest.* Earth and Planetary Science Letters, 2011.

[71] TROIANO A., DI GIUSEPPE M.G., PETRILLO Z. , TROISE C. and DE NATALE G., *Ground deformation at calderas driven by fluid injection: modelling unrest episodes at Campi Flegrei (Italy)*. Geophys. J. Int., 187, 833–847, doi: 10.1111/j.1365-246X.2011.05149.x, 2011.

[72] TROISE C., DE NATALE G., PINGUE F., TAMMARO U., DE MARTINO P., OBRIZZO F., and BOSCHI E., *A new uplift episode at Campi Flegrei caldera (southern Italy): Implications for unrest interpretation and eruption hazard evaluation*, Dev. Volcanol., 10, 375–392, doi:10.1016/S1871-644X(07) 00010-1, 2008.

[73] WANG, R., LORENZO MARTIN F. and ROTH F., *PSGRN/PSCMP – a new code for calculating co- and post-seismic deformation, geoid and gravity changes based on the viscoelastic-gravitational dislocation theory*. Computers & Geosciences, 32, 527–541, 2006.

[74] WOO J. Y. L. and KILBOURN C. R. J., *Intrusion and deformation at Campi Flegrei, southern Italy: Sills, dikes and regional extension.* Journal of Geophysical Research: Solid Earth, 2010.

[75] YANG X., DAVIS P., *Deformation from inflation of a dipping finite prolate spheroid in an elastic half-space as a model for volcanic stressing.* Journal of Geophysical Research., Vol.93, No.B5, 1988.

[76] Zollo A., MAERCKLIN N., VASSALLO M., DELLO IACONO D.,VIRIEUX J. and GASPARINI P., *Seismic reflections reveal a massive melt layer feeding Campi Flegrei caldera*. Geophys.Res. Lett., 35, doi:10.1029/2008GL034242, 2008.